The Dissertation Committee for Miguel Cisneros Certifies that this is the approved version of the following Dissertation:

Constraining the exhumation history of high-pressure subduction zone rocks: insights from the Cycladic islands, Greece and the application of novel thermobarometry techniques

Committee:

Jaime, Barnes, Supervisor

Whitney Behr

Daniel Stockli

Richard Ketcham

Kyle Ashley

Kenneth Befus

Constraining the exhumation history of high-pressure subduction zone rocks: insights from the Cycladic islands, Greece and the application of novel thermobarometry techniques

by

Miguel Cisneros

Dissertation

Presented to the Faculty of the Graduate School of

The University of Texas at Austin

in Partial Fulfillment

of the Requirements

for the Degree of

Doctor of Philosophy

The University of Texas at Austin

December 2018

Dedication

This dissertation is dedicated to my parents Elidia and Heriberto Cisneros, for their continued support throughout the many years I spent far away from California.

Acknowledgements

I would like to thank my advisor, Jaime Barnes, for her continued support and encouragement throughout my PhD. I owe much gratitude to my committee as well. Danny Stockli, for initially introducing me to the Cycladic islands. Whitney Behr for endless fruitful discussions about the Cyclades, and the evolution of rocks throughout exhumation and core-complex detachment. This work would not have been possible without the insight gained from her microstructures course that drove a lot of the direction of my research. Rich Ketcham, for initially introducing me to isotopes, age-dating techniques, and their applications. And of course, my external members Kyle Ashley and Kenny Befus, whom have both been a continued stream of support during the advancement of elastic thermobarometry that shaped much of my research. This PhD would have been impossible without their encouragement and guidance. The undergraduates whom I was fortunate to work with during graduate school, Tim Prather, Rania Eldam, and Natalie Raia. My research was also greatly shaped by discussions and field work help from the Greece and Barnes research groups, including Kostis Soukis, Spencer Seman, Natalie Raia, Emily Cooperdock, Eirini Poulaki, Megan Flansburg, Jeff Cullen, Evan Ramos, Grace Beaudoin, Michelle Gevedon, Ed Marshall and Alexandra Holmes. A special thanks to Alissa Kotowski, whom readily helped me with research and gave me beautiful thin sections. And lastly to some of the biggest support in my life, my family and friends: Elidia and Heriberto Cisneros, the entire Cisneros and Benavides families, Kris Darnell, Colin McNeece, Stephen Ferencz, Jasmine Mason, Kristina Walowski, Michael Huh, Robin Zuza, Elliot and Florence Dahl, Jeff Cullen, Scott Eckley, Kelly Olsen, Heather Christensen, Jacob Jordan, Brendan Murphy, Rosemary and Kevin Befus, Jeff and Veronica Senison, and so

many more. This process would have been impossible without all of your individual contributions to my life.

Abstract

Constraining the exhumation history of high-pressure subduction zone rocks: insights from the Cycladic islands, Greece and the application of novel thermobarometry techniques

Miguel Cisneros, PhD

The University of Texas at Austin, 2018

Supervisor: Jaime Barnes

The mechanisms that lead to exhumation of high-pressure low-temperature (HP-LT) metamorphic rocks have remained enigmatic since the recognition of the petrologic significance of blueschist facies mineral assemblages. Much of our understanding about these mechanisms stems from constraints of the pressure-temperature history of exhumed metamorphic rocks. In this work I describe the results of four projects that focus on testing new thermobarometers that can be applied to metamorphic rocks, among other rock types, and then apply multiple integrative techniques to constrain the pressure-temperature-fluid histories of rocks from Syros and Tinos, Greece. Elastic thermobarometry is a rapidly expanding technique that can be used to constrain pressures and temperatures from inclusion-host mineral pairs. I present a compilation of new inclusion-host mineral pairs that can be used to constrain PT conditions, and an adaptive script that can be used for calculating entrapment pressure or temperature conditions from residual inclusion pressures. I further complete a case-study of the quartz-in-epidote barometer, because of

its great abundance in metamorphic rock types and its potential utility for understanding geologic systems that currently lack barometers. Results from heating measurements of quartz inclusions in epidote from Alpine metamorphic rocks indicate two promising conclusions: 1) calculated entrapment pressures show good agreement with previously constrained pressure conditions, indicating that further investigation of the barometer is warranted, and 2) the quartz-in-epidote barometer may not require temperature-dependent entrapment pressure corrections.

The Cycladic Blueschist Unit on both Syros and Tinos, Greece, preserves exhumed, HP subduction zone rocks that have an enigmatic history after having reached peak metamorphic conditions. I present a combination of thermobarometry and mineral chemistry techniques that include further application of the quartz-in-epidote barometer, oxygen isotope thermometry, and fluid chemistry as deduced from oxygen, hydrogen, and carbon isotopes, to better understand the protracted exhumation history of metamorphic belts. Results from PT-fluid data from select outcrops that record changing kinematics, indicate that retrograde metamorphic rocks from Syros Greece underwent cooling during decompression, and interaction with slab derived fluids during exhumation. Lower pressure samples from Tinos Greece and hydrogen isotopes possibly show evidence of interaction with meteoric derived fluids during later stages of exhumation along a low-angle detachment.

Table of Contents

List of Tables

List of Figures

Chapter 1: Introduction

Metamorphic rocks provide an indirect window into processes that occur in continental and oceanic crust, wherein many of these processes are important in shaping the evolution of continents. The presence of high-pressure low-temperature (HP-LT) rocks that formed under depressed geothermal gradients in subduction zones, provide a key observation that indicates important dynamic processes occur in the crust to bring these rocks back up to the surface. This dissertation ties together new thermobarometry techniques and applies them to metamorphic rocks from Syros and Tinos, Greece, in combination with kinematic constraints, PT conditions, and fluid chemistry, to constrain how high-pressure metamorphic rocks from subduction zones are exhumed back to the surface.

Chapter 2 presents an array of thermobarometers that have great theoretical potential to be utilized in the future. This chapter uses elastic thermobarometry and an extensive thermodynamic database to test potential thermobarometers and presents a script that users can use to quickly calculate pressure and temperature conditions from residual mineral inclusion pressures. Three case studies are also carried out, and they show that the apatite-in-olivine barometer has great potential for igneous rocks, the albite-in-epidote barometer has great potential for metamorphic rocks but exhibits a complex array of residual inclusion pressures, and the last case study on rutile inclusion in garnet fails. The combination of all three cases highlights some of the potential pitfalls and advantages of the technique.

Chapter 3 tests the quartz-in-epidote elastic barometer by examining if the applied equations of state and isotropic elastic model are suitable when simulating the elastic

evolution of two anisotropic minerals, and by comparing calculated entrapment pressures from Alpine samples with reference pressure-temperature constraints. Two of our quartz-in-epidote entrapment pressure calculations show good agreement with reference pressure-temperature conditions of samples from the Alps. Epidotes from one sample show different petrographic context than the remaining assemblage and exhibits a low entrapment pressure relative to reference constraints.

Chapter 4 applies kinematic constraints, the quartz-in-epidote barometer, and stable isotope thermometry, to provide constraints on the exhumation history of high-pressure rocks from Syros, Greece. The results reveal high-pressure garnet-growth at ~ 1.4 - 1.5 GPa and 500 °C, retrograde epidote growth at ~1.3 – 1.4 GPa between 500 - 400 °C, and a second stage of retrograde low-pressure epidote growth at ~1.0 GPa and 400 °C. These results are consistent with stages of deformation that record a change of kinematics from subduction through exhumation and suggests that Syros underwent incipient cooling during decompression after reaching maximum high-pressure/low-temperature conditions, consistent with a cold PT evolution that is indicative of exhumation adjacent to a subduction zone boundary within a subduction channel prior to core-complex capture.

Chapter 5 uses the chemistry of fluids preserved during stages of exhumation on Syros and Tinos, Greece, to understand the tectonic setting of these rocks during exhumation. The fluid history as deduced from $\delta^{18}O$, δD, and $\delta^{13}C$ values of epidote boudin neck quartz-calcite pairs and mineral separates that record greenschist facies metamorphic conditions, indicate possible interaction with slab-derived fluids derived from dehydration of altered oceanic crust (basalts) or sediments, and a low $\delta^{13}C$ carbon source. Quartz-calcite pairs from epidote boudin necks that record higher temperatures indicate similar $\delta^{18}O$ values of fluids as those present during greenschist facies metamorphism, implying similar

fluid sources. Carbon isotope values of these higher temperature boudins; however, may indicate carbon sourced from a reservoir with higher $\delta^{13}C$ values. The fluid history of samples from below the Tinos detachment indicate possible late-stage interaction with meteoric water. The contrasting fluid histories present differences in the tectonic position of rocks preserved on both islands during exhumation.

Chapter 2: Applying solid mineral inclusion thermobarometry: the good, the bad, and the beautiful

ABSTRACT

Solid mineral inclusion thermobarometry can be used to extract the pressure and temperature conditions of mineral crystallization by exploiting the relative differences between the elastic properties of a crystalline inclusion and its host during ascent, exhumation, and cooling. To date, the application of solid inclusion thermobarometry has been limited by analytical difficulties, uncertainty in thermodynamic properties, and a lack of quantitative calibrations. We test the pressure-temperature sensitivity of 5142 different inclusion-host pairs. Rigid hosts, such as diamond and zircon, make outstanding containment vessels. Highly compressible mineral inclusions, such as albite, graphite, and quartz serve as the most reliable barometers. We provide three case studies in diverse geologic settings to demonstrate the benefits and shortcomings of solid inclusion thermobarometry. Apatite-in-fayalite measurements from Yellowstone caldera indicate shallow magmatic crystallization at ~100 MPa, in remarkable agreement with independent constraints. Rutile-in-garnet from the Verpeneset eclogite fails to recover reasonable metamorphic conditions. Albite-in-epidote measurements from a blueschist from Syros, Greece possibly indicate two stages of epidote growth. The population with high-pressure entrapment pressures indicates epidote crystallization at ~1200 MPa, in agreement with previous estimates. To make solid inclusion thermobarometry accessible to the greater community, we share an adaptable script that is built upon an extensive thermodynamic database and performs elastic modeling for a large suite of inclusion-host mineral pairs. Solid inclusion thermobarometry can be used to understand petrologic processes in diverse

geologic environments, including mantle, metamorphic, magmatic, and even extraterrestrial settings.

2.1 INTRODUCTION

No methods exist to directly monitor magmatic, metamorphic, and mantle processes that occur in the deep subsurface. Dynamic processes in these subsurface environments remain at the forefront of geoscience research because they control tectonism and crustal deformation, seismic and volcanic hazards, the geomorphic evolution of landscapes, and the generation of economic mineral resources. To learn about what we cannot see, we are forced to rely on indirect methods that include careful fieldwork and outcrop observations, petrography, geophysical methods, high pressure and temperature (PT) experiments, and theoretical calculations. The PT conditions of mineral and rock crystallization are variables central for understanding petrology because they influence processes such as crustal and mantle deformation, crystallization kinetics, molecular diffusion, and melt rheology. Accordingly, many techniques have been developed to constrain PT conditions (e.g., mineral-mineral equilibria, cation-exchange thermobarometry, order-disorder of crystals, and stable isotope thermometry)(e.g., Javoy 1977; Ferry and Spear 1978; Beyssac et al. 2002; Gualda et al. 2012). Unfortunately, several of these methods have practical limitations imposed by the requisite mineralogy or require assumptions of chemical or isotopic equilibrium. The petrology community is thus continuously exploring innovative techniques to constrain the PT conditions of mineral crystallization.

The application of solid mineral inclusion thermobarometry represents one increasingly important method to determine the PT conditions of mineral crystallization

(Ashley et al., 2017, 2016, 2014; Barkoff et al., 2017; Izraeli et al., 1999; Parkinson and Katayama, 1999; Sobolev et al., 2000). The technique has recently generated significant interest because it can be used for thermobarometry on micron-scale specimens in diverse geologic environments that previously did not have suitable thermobarometers. A plethora of recent work has aimed at better understanding the methodology, leading to important advancements (Parkinson and Katayama 1999; Angel et al. 2014b; Ashley et al. 2014a; Barkoff et al. 2017; Mazzucchelli et al. 2018; Thomas and Spear 2018). Solid mineral inclusion thermobarometry was first developed in the 1960s by J.L. Rosenfeld and colleagues (Rosenfeld and Chase 1961; Rosenfeld 1969; Adams et al. 1975b, 1975a; Cohen and Rosenfeld 1979). They recognized that elastic differences between the crystalline inclusion and host would generate quantifiable lattice strain during eruption or exhumation. Those strains are preserved by the host crystal and are related to entrapment (e.g., Guiraud and Powell, 2006; Kohn, 2014). Despite the promise of this method, it failed to find wide use because quantifying the preserved, residual strain was problematic. Fortunately, updated thermodynamic databases, improved mineral elasticity models, and advancements in analytical instrumentation, now allow for the application and further advancement of quantitative solid mineral inclusion thermobarometry (Kohn 2014; Angel et al. 2017b, 2017a).

Solid mineral inclusion thermobarometry calculations are solely dependent upon the thermodynamic and elastic properties of inclusion-host pairs. Thus, the technique has several key advantages in comparison to conventional thermobarometry. For example, neither chemical nor isotopic equilibrium amongst phases is required, and no bulk-rock composition constraints exist, allowing the technique to be widely applicable to all rock compositions. Furthermore, the technique offers a high spatial resolution, often at the

micron-scale. The high spatial resolution allows investigators to constrain PT conditions from inclusions within discrete sub-domains of a single crystal. Surprisingly, solid inclusion thermobarometry has primarily been applied to diamond- and garnet-hosted inclusions (Cohen and Rosenfeld 1979; Izraeli et al. 1999; Howell et al. 2010; Ashley et al. 2014b; Thomas and Spear 2018). Many inclusion-host pairs that could be used to extract petrologically valuable PT information have yet to be explored.

In this study, we test the suitability of different inclusion-host pairs for their potential as barometers or thermometers. From that set of pairs, we identify many potential thermometers and barometers. Most of these inclusion-host pairs have never previously been tested. We targeted three new pairs for introductory studies. We demonstrate that apatite-in-fayalite from Yellowstone caldera and albite-in-epidote from Syros, Greece recover crystallization conditions that agree with published results. Not all inclusion-host pairs work, either due to difficulties with analytical measurements, inaccurate mineral pair thermodynamic properties, inadequacies associated with isotropic elastic modeling, or other reasons we discuss below. To demonstrate failure, we show how residual pressures in rutile-in-garnet from a Norwegian eclogite indicate garnet crystallization far from established prograde metamorphic conditions.

We also provide a new program that allows simple, rapid implementation of solid inclusion thermobarometry for a large collection of inclusion-host pairs, to make the technique more accessible to the greater geoscience community. The computer program is user-friendly and is provided as a script and graphical user interface (GUI) in both MATLAB and Python. This work independently builds upon that spurred by Kohn (2014) and Angel et al. (2017b), by expanding the mineral thermodynamic database and constraining the utility of inclusion-host pairs as thermobarometers. Our work continues to

introduce the theory and application of solid mineral inclusion thermobarometry to the community of earth and planetary petrologists. Our script then enables the community to rapidly apply the technique to better understand fundamental geologic processes.

2.2 METHODS

2.2.1 Entrapment pressure-temperature calculations: an overview

The difference in compressibility and thermal expansivity between the crystalline inclusion and host generates compression or expansion of the inclusion as PT conditions change. Strained, encapsulated inclusions at ambient temperature preserve a residual stress that can be measured by multiple techniques, including measurement of birefringent halos surrounding inclusions (Rosenfeld and Chase 1961; Howell et al. 2010), X-ray Diffraction (Harris and Munn 1970; Nestola et al. 2011), and by the approach we implement in this study, Raman spectroscopy (Ashley et al. 2014a, 2016, 2017). We can use residual stress measurements combined with elastic modeling to calculate either the entrapment pressure (P_{ent}) or temperature (T_{ent}) following depressurization and cooling during exhumation and ascent to the Earth's surface.

To calculate entrapment pressures or temperatures, we perform 1-dimensional elastic modeling to determine the elastic response of inclusion-host pairs upon return to ambient conditions. We implement the Guiraud and Powell (2006) elastic model with a correction applied by Angel et al. (2017), following the equation:

$$\left[\left(\frac{V}{V_0}\right)_{incl} - \left(\frac{V}{V_0}\right)_{host}\right]\left(\frac{V_0}{V_{foot}}\right)_{incl} = \frac{3}{4G_{host}}(P_{incl} - P_{ext})$$

where $(V/V_0)_{incl}$ and $(V/V_0)_{host}$ are the molar volume ratios of the entrapped inclusion and the host at ambient temperature and pressure (V) and at entrapment conditions (V_0). The molar volume of the inclusion at ambient conditions incorporates ambient temperature and the analytically measured residual pressure retained by the inclusion. $(V_0/V_{foot})_{incl}$ is the ratio of the inclusion molar volume at entrapment conditions (V_0) and at ambient temperature along the inclusion-host pair isomeke (briefly discussed below) defined by the entrapment conditions (V_{foot})(see Angel et al. 2017b). G_{host}, P_{incl}, and P_{ext} are the shear modulus of the host, the inclusion pressure at ambient conditions, and ambient pressure, respectively. For minerals that have experimentally determined shear moduli, we use their calculated shear moduli in the elastic model calculations. Otherwise, the shear modulus of the host is calculated from mineral Poisson ratios and bulk moduli, following the equation:

$$G = \frac{3K(1 - 2\nu)}{2(1 + \nu)}$$

where G is the shear modulus, K is the bulk modulus, and ν is the Poisson ratio. Mineral shear moduli and poisson ratios were compiled from various literature sources that are provided in the supplementary material to Chapter 2. We limited our application to 72 mineral phases with reported shear moduli or Poisson ratios, but many of these minerals require further refinement of elastic properties before accurate, reliable PT calculations can be carried-out. Our inclusion-host dataset will grow as future studies constrain shear moduli or Poisson ratios of additional minerals.

In Equation 1, all variables other than the molar volume of the inclusion and host (V_0), are held constant. The entrapment conditions are solved for by assuming a temperature or pressure of entrapment (T_{ent} and P_{ent}), and then iteratively calculating V_0 in the elastic model equation until both sides of the equation are equal (Guiraud and Powell

2006; Kohn 2014; Ashley et al. 2016). Conversely, if entrapment conditions can be assumed then we can solve for a theoretical inclusion pressure (P_{incl}). Incorporation of the Angel et al. (2017) correction also requires iterative calculation of P_{foot}, i.e., the pressure along the entrapment isomeke at ambient temperature, prior to calculation of entrapment conditions or P_{incl}.

To test the potential of inclusion-host pairs to serve as barometers, we calculate the change of P_{ent} and T_{ent} at constant P_{incl}. These isobaric inclusion pressures show the position of a constant P_{incl} in PT space, and are referred to as isomekes ("iso" =equal, meke = "length") in previous studies (Adams et al. 1975b, 1975a; Angel et al. 2014b). Isomeke lines represent points in PT space along which fractional volume changes between the inclusion and host are equal. Therefore, the isomeke contours are the P_{ent} or T_{ent} solution to a measured P_{incl}. For clarification, we present P_{ent} and T_{ent} calculations at a constant P_{incl} as isomeke contours. Isomeke slope and spacing are important criteria for thermobarometry. Inclusion-host pairs with steep isomeke slopes make the best thermometers whereas those with shallow slopes are the best barometers. Intermediate isomeke slopes allow either P_{ent} or T_{ent} to be determined but require an independent constraint of one of the variables.

2.2.2 Thermodynamic properties of end-members and molar volume calculations

To perform molar volume calculations, we used thermodynamic properties from various sources. Most of the thermodynamic properties implemented for molar volume calculations were derived from the Holland & Powell (2011) thermodynamic database (see the Supplementary Information for Chapter 2 and the MATLAB and Python thermodynamic properties Excel spreadsheet for sources). We use the isothermal Tait Equation of State (EOS) with a thermal pressure correction to solve for molar volumes at

given PT conditions (Holland and Powell 2011). The script implements Landau and Braggs-William theory to calculate excess molar volumes caused by spontaneous strain development of phases that undergo phase transitions (see Holland and Powell, 1996a, 1996b, 1998, 2011).

For a few mineral end-members, we have used thermodynamic properties that we have calculated from experimental data or implement literature data. The properties of epidote and clinozoisite were taken from the experimental molar volume data of Gatta et al. (2011), and Holland et al. (1996), Pawley et al. (1996), respectively. P-V-T experimental data was refit with the modified Tait EOS with a thermal pressure correction in EOSFit7c (Angel et al. 2014b). To best model quartz volumes, we rely upon the thermodynamic properties of quartz from Angel et al. (2017a). To replicate their modeling approach for quartz molar volumes, we follow an approach consistent with their best-fit "curved-boundary model."

Our script can easily be modified by users wishing to manually input thermodynamic properties of their preference, preferred EOS', and bulk modulus temperature corrections. Additionally, users can manually input new mineral phases to be modelled. The script incorporates linear mixing, and the GUI allows for the manual input of up to 5 end-members to best represent the solid-solution phase of interest. Following previous studies, we note that linear mixing of compositional end-members may result in differences in entrapment pressures up to 100's of MPa (e.g., Ashley et al., 2014c). Hence, solid-solutions must be considered when compositional data of the inclusion or host phases is available.

2.2.3 Analytical techniques

We present introductory case studies that utilize previously untested inclusion-host pairs to demonstrate the practicality of solid mineral thermobarometry (P_{incl} determined by Raman spectroscopy). For each study, we petrographically identified hosts containing mineral inclusions. We identified apatite-in-fayalite and rutile-in-garnet in grain mounts of handpicked crystals. Albite inclusions in epidote were identified in 80-μm thick petrographic sections. Thick sections or thick grain mounts are preferable because their thickness preserves a larger host volume, which better ensures complete entrapment and reduces the possibility of stress reduction of the inclusion relative to its ideal stress state (Mazzucchelli et al. 2018). Whether in thin or thick sections, inclusions should ideally be isolated, and ~ three-to-four times the inclusion radial distance from the host exterior, fractures, cleavage, or other inclusions (Mazzucchelli et al. 2018). Proximity to the host exterior, fractures, or cleavage could release stresses, and proximity to other inclusions may produce over-pressures that exceed ideal pressures from pure elastic relaxation. Inclusions should be >1 μm in diameter, as previous work has shown that small inclusions preserve a stress field that reflects over-pressurization relative to true elastic relaxation (Kyle Ashley, personal communication).

We performed Raman analyses by using spectrometers housed separately at Baylor University and Virginia Tech. At Baylor University we used a confocal Thermoscientific DXR Raman microscope equipped with a green 532 nm laser. Measurements were performed at 10 mW with a 100x objective, which allowed us to focus the beam on the target inclusion with a spatial resolution of 1 μm. We collected data using a high-resolution grating and fit the resulting data with a least-squares smoothing interpolant. Together, this approach allowed us to measure peak position with a spectral resolution of ~1 cm^{-1}.

Measurements at Virginia Tech were carried out on a JY Horiba LabRam HR800 Raman Spectrometer with a high resolution 1800 lines mm^{-1} grating. We used a 100x objective with a confocal aperture of 400 µm and 150 µm slit width. An Ar laser interference filter was removed for all analyses to allow us to simultaneously correct feldspar measurements for drift by applying a linear drift correction dependent on the position of the 520.30 cm^{-1} Ar plasmaline. Instrument standardization was carried out by repeatedly measuring the 497 cm^{-1} and 508 cm^{-1} peak positions of an Amelia Albite standard. Based on the long-term instrument stability as deduced from standard measurements, analytical uncertainty at Virginia Tech is ± 0.1 cm^{-1}. For measurements made at Virginia Tech, we used the program PeakFit v4.12 for fitting all the measured spectra.

The crystal lattices of fully encapsulated inclusions are pressurized whereas matrix phases and exposed inclusions are relaxed to, or near, ambient PT conditions. The amount of residual stress in the entrapped inclusions is primarily controlled by the host shear modulus, and the evolution of thermal expansivity and compressibility of an inclusion-host pair since the time of entrapment. The difference in wavenumber between the enclosed inclusions and relaxed matrix or exposed inclusions is coined the "Raman shift(s)." We use Raman shift to calculate residual inclusion pressures (P_{incl}) for minerals whose pressure-dependent Raman shift(s) have been empirically calibrated (Comodi et al. 2001; Schouwink et al. 2010); *feldspar:* (Aliatis et al. 2017; Befus et al. 2018); *anatase/rutile:* (Samara and Peercy 1973; Liu and Mernagh 1992; Swamy et al. 2005); *and quartz/coesite:* (Asell and Nicol 1968; Schmidt and Ziemann 2000; Hemley R. J. 2013). Many minerals have pressure-dependent Raman shifts whose sensitivity ranges from ~1 to 4 cm^{-1} GPa^{-1} (Mernagh and Liu 1991; Yang et al. 1997); *brucite:* (Duffy et al. 2015); *diamond:* (Boppart et al. 1985; Hanfland et al. 1985; Tardieu et al. 1990; Occelli et al. 2003); *garnet:* (Mernagh

and Liu 1990; Gillet et al. 1992); *graphite:* (Hanfland et al. 1989; Sandler et al. 2003); *gypsum:* (Knittle et al. 2001); *olivine:* (Gillet et al. 1989; Wang et al. 1993); *perovskite:* (Williams et al. 1987; Hemley et al. 1989); *pyroxene:* (Lin 2003); *serpentine:* (Auzende et al. 2004; Reynard and Wunder 2006); *spinel:* Wang et al., 2003b, 2003a, 2002c, 2002b, 2002a, 2002; *wurtzite:* (Decremps et al. 2002); *and zircon:* (Schmidt et al. 2013); however, many other important mineral's Raman shifts remain unconstrained. When it is not possible to measure Raman shifts relative to minerals in the matrix, we suggest measuring Raman shifts relative to exposed inclusions. If neither are possible, then we suggest measuring Raman shifts relative to compositionally identical standards.

2.3 RESULTS

2.3.1 Suitable inclusion-host pairs

We test the thermobarometric potential of 5142 inclusion-host pairs by carrying out entrapment pressure and temperature calculations to produce isomeke contour positions in PT space (Fig. 2.1). For each pair, we calculated P_{ent} for an isobaric inclusion pressure (P_{incl}, contours herein referred to as isomekes) and by changing temperature (T_{ent}), from -200 to 800 MPa and 300 to 1000 ºC, using 100 MPa and 100 ºC intervals, respectively. Isomeke slopes vary from 0.4 to $10^{5.1}$ MPa ºC^{-1}, with a median value of 1.9 MPa ºC^{-1} (Fig. 2.1C, E; Supplemental Table 1 for Chapter 2). We measure isomeke spacing perpendicular to isomeke slopes, hence the units may be considered MPa (near horizontal slope), ºC (near vertical slope), or a combination of MPa ºC^{-1}. Isomeke spacing ranges from ~0 up to $10^{4.3}$ about a median of 189 MPa, ºC, or MPa ºC^{-1}. Isomeke spacings are more tightly distributed about the mean than isomeke slope (Fig. 2.1D, F). We find that inclusions with high compressibilities (e.g., low bulk modulus phases such as quartz and feldspars) serve as the

better barometers, whereas phases that have a significant difference in thermal expansivity, serve as the best thermometers.

2.3.2 Case Studies

We herein present case studies for 3 inclusion host-pairs from different geologic environments (Fig. 2.2). Our first case study highlights the potential of using apatite inclusions hosted by olivine. We measured the 964 cm^{-1} peak of apatite inclusions within fayalite phenocrysts from the rhyolitic obsidian Solfatara Plateau Lava flow in Yellowstone caldera (Fig. 2.2A, 2.3A). Microphenocrysts of apatite in the glassy matrix have peak positions at 962.4 ± 0.2 cm^{-1}, whereas 9 apatite-in-fayalite display peaks at 961.5 ± 0.3 cm^{-1}. The enclosed apatite inclusions exist under tension, as demonstrated by the negative peak shift of -0.9 ± 0.3 cm^{-1}. The apatite 964 cm^{-1} peak exhibits a pressure-dependent shift that has been experimentally calibrated (Comodi et al. 2001; Schouwink et al. 2010). To calculate P_{incl} from apatite Raman shifts, we implement the regression to the preceding experimental data calculated by Ashley et al. (2017). Calculated residual pressures recorded by apatite suggest that the inclusions preserve an average tensional pressure of -201 ± 78 MPa (s.d. of calculated inclusion pressures, Table 2.1).

For our second case study, we measured the ~444 and ~609 cm^{-1} Raman peaks in garnet hosted rutile inclusions from the Verpeneset eclogite in western Norway (Fig. 2.2B, 2.3B). Liu and Mernagh (1992) demonstrate that both rutile peaks experience pressure-dependent shifts to higher wavenumber with slopes of 3.9 and 4.1 cm GPa^{-1}, respectively. Exposed rutile inclusions from the eclogite have peak positions at 443.9 ± 0.5 and 609.0 ± 0.2 cm^{-1}. Fully encased rutile inclusions have peak positions at 444.1 ± 0.4 and 609.4 ± 0.5 cm^{-1}. If we simply use the average of 10 measurements at each of the ~444 and ~609 cm^{-1}

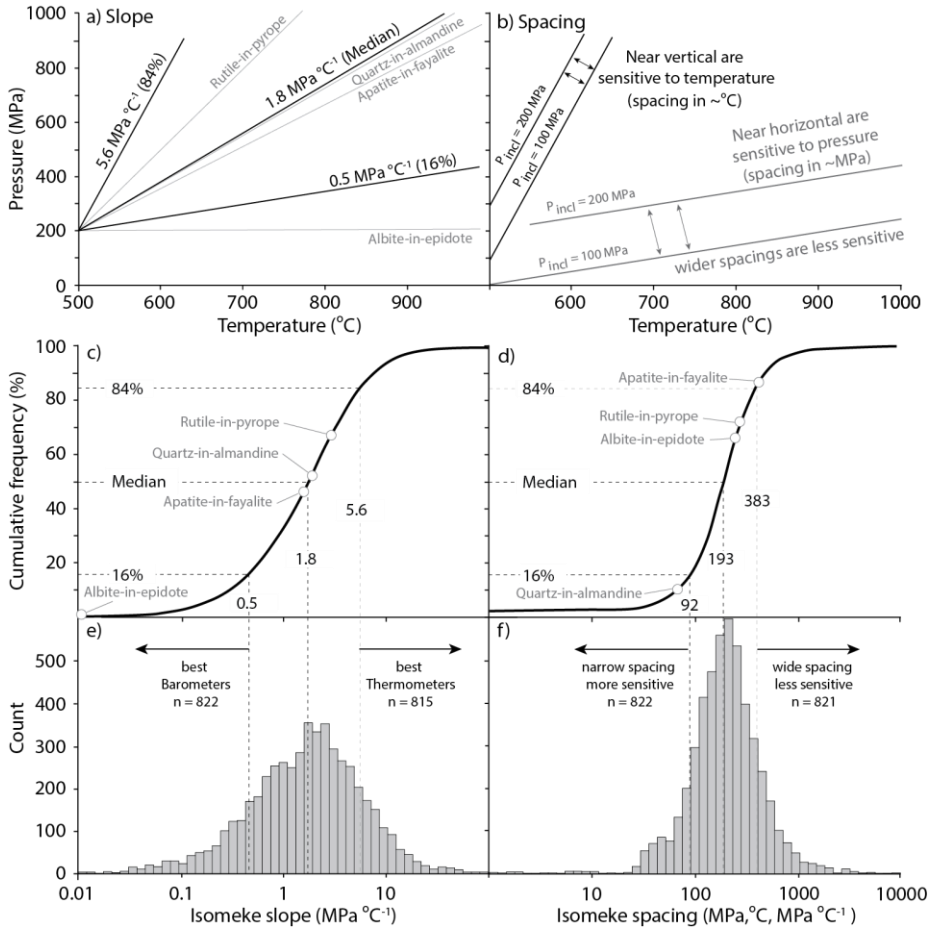

Figure 2.1: **a**) Isomeke slopes for inclusion-host pairs. Representative inclusion-host pairs are chosen to illustrate excellent barometers (slope ≤ 0.5 MPa $°C^{-1}$) and thermometers (slope ≥ 5.6 MPa $°C^{-1}$). Pairs that fall in between these end-members require independent constraints to calculate the unknown variable of interest. **b**) Spacing between isomekes is a metric of sensitivity. Small spacing between isomeke contours indicates that a change in entrapment pressure or temperature, will produce large changes in measured residual inclusion pressures, ("high sensitivity"), whereas larger spacing will produce minimal change in measured residual inclusion pressures ("low sensitivity"). High sensitivity inclusion-host pairs are the easiest to implement because large changes in measured inclusion pressures will produce minimal changes in calculated entrapment pressures or temperatures. **c-f**) Cumulative frequency and histogram plots indicating the proportion of inclusion-host pairs that serve as barometers or thermometers and their sensitivities. Most inclusion-host pairs serve as thermobarometers that require independent entrapment pressure or temperature estimates to derive the unknown variable (entrapment P or T). A wide-range of inclusion-host pairs have tightly spaced isomekes, making these inclusion-host pairs most easily applicable in solid mineral inclusion thermobarometry.

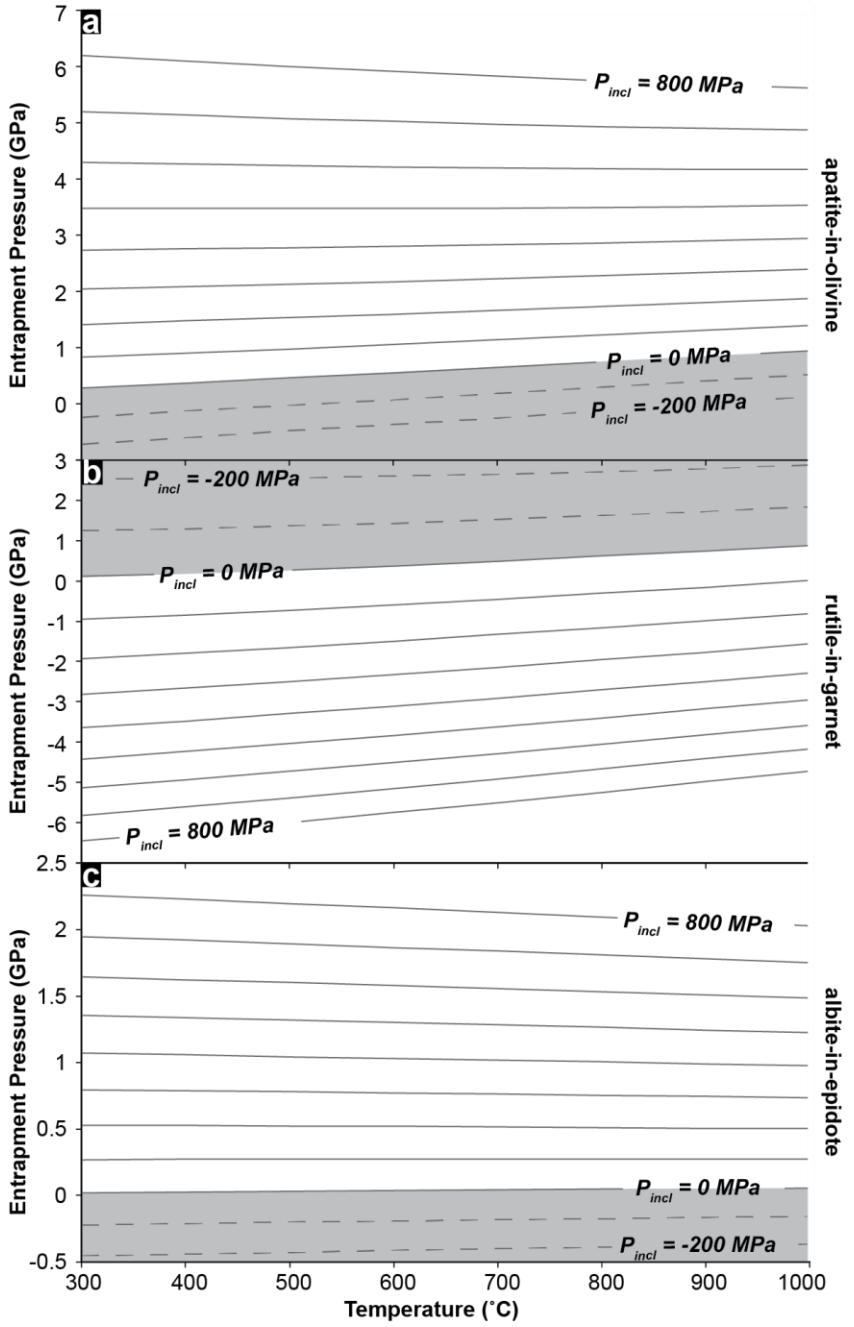

Figure 2.2: Isomekes graphs for **a**) apatite-in-fayalite, **b**) rutile-in-garnet, and **c**) albite-in-epidote inclusion-host pairs. Isomekes are contoured in 100 MPa P_{incl} intervals. Mineral compositions are provided in the text. Dashed lines indicate negative isomekes. Gray areas highlight areas where measured inclusion pressures would theoretically retain negative values.

peak positions, then we calculate that the inclusions retain residual pressures of 51 and 54 MPa, respectively (Table 2.1). However, if we include the 1σ deviation, the range of possible residual pressures extends from -167 to 269 MPa. We acknowledge that our uncertainties are significant, and they result from a combination of real variability, the small number of analyses in our case study, and the relatively poor ~1 cm^{-1} spectral resolution of the Raman system. We suggest that future studies produce much larger datasets with the best spectral resolution possible to minimize pressure uncertainties.

Our final case study highlights the potential of using albite inclusions entrapped by epidote as a barometer (Fig. 2.2C, 2.3C). We calculate residual inclusion pressures from the albite 479 cm^{-1} band, and calculate frequency shifts relative to the ambient pressure 479 cm^{-1} peak position of the Amelia Albite standard. Albite inclusions retain pressures that record a compressional stress state as indicated by 479 cm^{-1} band shifts to higher wavenumbers (0.67 – 1.89 cm^{-1}), and we calculate inclusion pressures that range from 192 – 508 MPa (n = 9). Our results cluster into low and high pressures groups, that average 279 ± 103 MPa (range; n = 3) and 439 ± 63 MPa (range; n = 6), respectively (Table 2.1).

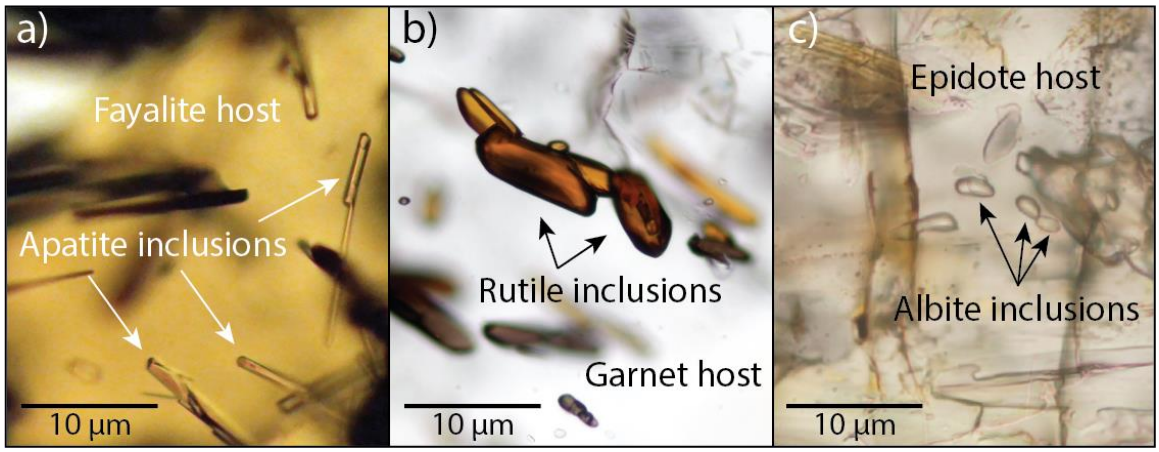

Figure 2.3: **a**) Apatite inclusions within fayalite from Yellowstone caldera. **b**) Rutile inclusions in a garnet from a Verpenset eclogite from western Norway. **c**) Albite inclusions encapsulated within epidote from a blueschist facies rock from Syros, Greece. These inclusions are shown for illustrative purposes and were not necessarily those analyzed here (e.g. too close to fractures, inclusions too close to each other, etc).

2.4 DISCUSSION

We have discovered many new inclusion-host pairs that may be useful for solid mineral inclusion thermobarometry. Our GUI can immediately be used to constrain PT conditions for a wide-range of inclusion-host pairs from diverse geologic environments. After an inclusion-host pair is targeted, we first recommend considering the isomeke slope and spacing. Importantly, we do not specify a range of appropriate slope or spacing. The useful range of each variable will depend on the task at hand. For example, quartz-in-almandine isomekes have a slope of 1.8 MPa $^{o}C^{-1}$, very near the median slope of 1.9 MPa $^{o}C^{-1}$, and certainly far above the arbitrary 16th percentile slope threshold of 0.5 MPa $^{o}C^{-1}$ (Fig. 2.1C). But, quartz-in-almandine is known to be a reliable barometer, used to better understand petrologic and tectonic processes in many metamorphic environments (e.g., Ashley et al. 2014a, 2016). Similarly, isomeke spacing usefulness will depend on the application. To establish a practical foundation for solid inclusion thermobarometry, we

provide three case studies that use previously untested inclusion-host pairs from samples that have well-constrained magmatic and metamorphic PT conditions. These examples provide an introductory check on the reliability of the technique for these inclusion-host pairs. Two examples are successful, but the third fails. We show that analytical limitations and/or thermodynamic properties sometimes restrict the utility of solid mineral inclusion thermobarometry.

Apatite				Rutile				Albite			
		Raman Shift relative				Raman Shift relative				Raman Shift relative	
Analysis	Peak Position (cm^{-1})	to ambient[a] (cm^{-1})	P_{incl} (MPa)	Analysis	Peak Position (cm^{-1})	to ambient[a] (cm^{-1})	P_{incl} (MPa)	Analysis	Peak Position (cm^{-1})	to ambient[a] (cm^{-1})	P_{incl} (MPa)
1	962.2	-0.3	-57	1	444.4	0.5	128	1	609.3	0.25	61	1	481.4	1.73	475
2	961.2	-1.2	-275	2	443.9	0	0	2	609.3	0.25	61	2	481.1	1.43	394
3	961.7	-0.7	-163	3	444.4	0.5	128	3	608.8	-0.25	-61	3	481.6	1.86	508
4	961.2	-1.2	-275	4	443.9	0	0	4	609.3	0.25	61	4	481.3	1.52	417
5	961.7	-0.7	-163	5	443.9	0	0	5	608.8	-0.25	-61	5	480.3	0.67	192
6	961.2	-1.2	-275	6	443.4	-0.5	-128	6	608.3	-0.75	-183	6	480.9	1.18	329
7	961.7	-0.7	-163	7	444.4	0.5	128	7	609.7	0.65	159	7	481.4	1.58	433
8	961.2	-1.2	-275	8	444.4	0.5	128	8	610.2	1.15	280	8	480.0	0.89	250
9	961.7	-0.7	-163	9	443.9	0	0	9	609.7	0.65	159	9	480.8	1.72	473
Average	**961.5 (0.3)**	**-0.9 (0.3)**	**-201 (78)**	10	444.4	0.5	128	10	609.3	0.25	61	**Average**	**481(0.5)**	**1.40 (0.41)**	**386 (108)**
				Average	**444.1 (0.4)**	**0.2 (0.3)**	**51 (90)**	**Average**	**609.4 (0.5)**	**0.2 (0.5)**	**54 (132)**				

[a] Raman Peak positions of ambient minerals are: apatite at 962.4 cm^{-1}, rutile at 443.9 cm^{-1} and 609.1 cm^{-1}, and albite at 479.1cm^{-1}.
[b] Analyses by Raman spectroscopy. Values in parentheses represent the standard deviation of the analyzed measurements

Table 2.1: Raman measurements of peak position shift for each of the 3 case studies.

2.4.1 Applications for magmatic rocks

Volcano scientists and igneous petrologists use the PT conditions of magmatic rocks to better understand many processes, including melt genesis, assimilation and fractional crystallization, eruption triggers, and melt transport. Magmatic crystallization may occur over a range of depths, spanning the upper mantle to subaerial emplacement. Minerals within igneous rocks may also preserve a record of the regional tectonics that led to magma genesis and its subsequent evolution. Magma composition controls the mineral phases that may crystallize, and the diversity of magmatic "flavors" permits hundreds of potential solid mineral inclusion-host pairs to be considered as thermobarometers. Apatite-in-zircon, rutile-in-quartz, and magnetite-in-forsterite immediately draw our attention as untested pairs that may have wide applicability. Excitingly, our results likely represent only a fraction of the many more untried combinations that exist.

Here, we choose apatite-in-fayalite as the introductory magmatic application for Raman thermobarometry. Fully enclosed apatite inclusions from the Solfatara Plateau, Yellowstone caldera, preserve a tensional residual pressure of -201 ± 78 MPa. To calculate a P_{ent} from our measured P_{incl}, we must first constrain T_{ent} and the elastic properties of apatite and fayalite. Elastic properties most commonly vary with mineral composition. The composition of the fayalite in Solfatara Plateau is known to be $Fa_{92\pm1}$ (Befus and Gardner 2016). The composition of the apatite; however, is unknown. Importantly, the volatile (OH, F, Cl) composition of apatite exerts a nontrivial control on the crystal's elastic properties (Holland and Powell 2011; Ashley et al. 2017; Barkoff et al. 2017).

We estimate the composition of our targeted apatite through a combination of empirical volatile relationships and comparisons to apatite from the Mesa Falls Tuff, which represents the only previously published composition of apatite across Yellowstone

caldera. Apatite from the Mesa Falls Tuff contains 0.24 wt.% Cl and 3.27 wt.% F, but there is no direct record of OH content (Peng et al. 1997). In the place of a known measurement, we can calculate the OH component in the unit cell 'by difference' because the molar abundances of F, Cl, and OH should sum to 1. We can additionally constrain the composition of apatite because volatile partitioning into apatite is related to the magmatic volatile content (Webster and Piccoli 2015). Quartz-hosted melt inclusions from Solfatara Plateau contain 2063 ± 200 ppm F, 1080 ± 40 ppm Cl, and 1.6 ± 0.3 wt.% H_2O (Befus and Gardner 2016). H_2O contents differ between eruptive units at Yellowstone, but F and Cl are remarkably similar (Befus and Gardner 2016; Myers et al. 2016). Using the magmatic volatile contents of Solfatara Plateau, we calculate a magmatic X_{H2O} of 0.86 (mol fraction). This X_{H2O} indicates that the X_{H2O} in apatite should be between 1.1 to 2 times greater than X_{Cl}. By combining the 'by difference' approach with an empirical relationship between magmatic and apatite volatiles, we conclude that the mol fraction composition of apatite from Solfatara Plateau is well approximated by $X_{Cl} = 0.04$, $X_F = 0.91$, and $X_{OH} = 0.05$.

We calculate that Solfatara Plateau's apatite inclusions were entrapped at 108 MPa by using the average mineral compositions, average residual P_{incl}, and a pre-eruptive magmatic temperature (T_{ent}) of 800 ºC for Solfatara Plateau (Fig. 2.4A; (Vazquez et al. 2009; Befus and Gardner 2016). Calculated entrapment pressures range from 0 to 230 MPa if we include the 1σ standard deviation ranges for the composition and temperature variables, which is compounded to -281 to 411 MPa when we include the 1σ deviation of residual pressure. Each uncertainty exerts a different amount of variability on P_{ent} calculations. For example, assuming pure endmember fayalite and fluoroapatite increases our entrapment estimate by 30 MPa. Of that, the increased 8 mol.% Fa contributes 12 MPa whereas 9 mol.% X_F in apatite contributes the remaining 18 MPa. Changing entrapment

temperature by 50 ºC changes entrapment pressure by 100 MPa. Clearly reducing uncertainties is a critical aspect to consider for future Raman thermobarometry studies. Despite the substantial uncertainties in this case study, our best P_{ent} estimate of 108 MPa directly aligns with numerous independent estimates for shallow crustal storage at Yellowstone caldera (Befus and Gardner 2016; Myers et al. 2016; Gryger 2017). We find this agreement between Raman thermobarometry and geophysical investigations, experimental petrology, lake seiche seismology, mineral chemistry, and volatile saturation pressures encouraging.

2.4.2 Applications for metamorphic petrology

Metamorphic petrology is fundamental for understanding crustal and mantle dynamics, with processes that include, but are not limited to: continent and oceanic lithosphere subduction, obduction and exhumation, crustal strength, fault mechanics and rheology, and the effects of mantle dynamics on the evolution of the crust. A key focus for understanding these problems is through constraining the PT evolution of metamorphic rocks from these different environments. A large span of metamorphic rocks have suitable thermobarometers; nonetheless, some of the most common rocks types still prove difficult to extract PT conditions from (e.g., retrograde metamorphic rocks, skarn deposits, and spinel-bearing peridotites). We attempt to advance the understanding of the evolution of the crust by providing some key examples of the way Raman thermobarometry can be utilized to better understand the prograde and retrograde evolution of metamorphic rocks, especially for mafic lithologies that exhibit partial-recrystallization. We suggest the solid mineral inclusion thermobarometry offers great promise and can potentially be used to

constrain PT conditions of mineral growth and fabric development, allowing deformation and tectonic processes to be independently constrained.

We first explore a failed example of this technique to help the new user navigate potential pitfalls. The Verpeneset eclogite in western Norway occurs within ~400 Ma gneisses formed during the Caledonian Orogeny (Wain et al. 2000; Carswell et al. 2003; Tsujimori et al. 2006; Kylander-Clark et al. 2008). The eclogite is visually stunning in the field and museum displays. It contains an assemblage of omphacite + garnet + zoisite pseudomorphs after lawsonite + kyanite ± talc ± phengite ± hornblende ± rutile ± quartz (Krogh 1982; Wain et al. 2000). Rutile commonly occurs as acicular to ellipsoidal yellow-brown inclusions hosted by garnet. The garnets are compositionally zoned, thus we restricted analyses of rutile to near the core to limit compositional effects. Garnet core compositions are $Py_{24-35}Alm_{40-43}Grs_{20-25}Sps_{0-10}$ (Krogh 1982).

Our measurements of 2 separate Raman peak shifts indicates that rutile inclusions preserve residual pressures of 51 and 54 MPa. To calculate P_{ent} during garnet growth, we require an independent temperature estimate. Previous studies indicate that the maximum prograde conditions of eclogites vary from high-pressure to ultrahigh-pressure across the province. Eclogites in the southern region near Verpeneset record high pressure conditions that peak at 2.5 ± 0.3 GPa and 676 ± 88 ºC (Wain et al. 2000; Carswell et al. 2003; Hacker et al. 2010). If we assume the averages for temperature and garnet are appropriate (e.g., 676 ºC and $Py_{30}Alm_{42}Grs_{23}Sps_{5}$), then the residual pressures of rutile inclusions indicate entrapment pressures of -45 ± 15 MPa (Fig. 2.4B). If we expand the range of temperature and composition to account for the range across the region, P_{ent} ranges from -220 to 100 MPa. Including analytical uncertainty in $P_{incl,}$ entrapment pressures range from -1800 to 2400 MPa. Clearly, solid inclusion thermobarometry is not reliable for this case study.

We suggest several possible explanations for the failure of the rutile-in-garnet thermobarometer. Rutile inclusions may record prograde, low pressure garnet crystallization. However, the negative entrapment pressures of -45 ± 15 MPa are unrealistic and suggest this is very unlikely. During exhumation, rutile inclusions may have instead inelastically relaxed, thus reducing residual pressures next to fractures in garnet or the host exterior. In accordance with the study from Mazzucchelli et al. (2018), the rutile inclusions were small relative to the garnet host, and should not require a correction based on inclusion position in the host. Third, poorly constrained host and inclusion compositions may lead to large uncertainties in calculated PT conditions because solid-solution end-members may have different elastic properties. This is unlikely for a rock as well-studied as the Verpeneset eclogite. It is also possible that rutile inclusions have abundant U, and may therefore suffer from radiation damage, likely reducing its pressure relative to true elastic relaxation P_{incl}. Last, isomekes for this barometer are inverted, i.e., higher measured residual pressures indicate lower pressures of entrapment (Fig. 2.2B). Rutile inclusions may not be able to retain sufficient adhesion to the surrounding host, may relax by separating from the host, and may therefore not preserve an ideal tensional stress state that reflects elastic relaxation. We believe the limit of the maximum tension that inclusions can preserve may be important and requires further consideration in future solid inclusion thermobarometry studies. In summary, we do not have a definitive answer as to why the rutile-in-garnet pair failed to extract reasonable P_{ent} estimates. We suggest that all scenarios are possibilities that can explain failure and must be considered seriously in future studies.

In comparison to the failed rutile-in-garnet barometer, we now show an example that illustrates the potential of solid inclusion thermobarometry. Recent studies have shown

that feldspars (e.g., albite, andesine, and oligoclase) exhibit prominent, pressure-dependent Raman shifts that can confidently be measured and used to constrain entrapment PT conditions with low uncertainty (Befus et al. 2018). The high compressibility of feldspar, and its wide-spread occurrence in diverse geologic settings makes it an ideal inclusion that is suitable as a barometer in many host phases. We focus on testing the albite-in-epidote barometer because epidote is a rigid host, and it is abundant in most metamorphic rocks. Furthermore, in moderate-to-high pressure metamorphic rocks, feldspars exhibit compositions that are nearly pure albite end-members, making use of the pressure-dependent Raman shifts calibration far easier to use.

We sample blueschist facies rocks from Syros Greece (Kalamisia beach) to test the albite-in-epidote barometer. The metamorphic complex exposed on Syros, Greece reached estimated max PT conditions of ~1.5 – 2.0 GPa and 500 - 550 °C at ~ 50 Ma (Ridley 1984; Trotet et al. 2001a; Schumacher et al. 2008). It was subsequently exhumed to the mid-crust by the Miocene, with distinct episodes of deformation and retrogression occurring during exhumation prior-to and post core-complex capture (Bröcker and Enders 1999; Putlitz et al. 2005; Soukis and Stockli 2013). For our blueschist facies sample, we find epidote grains that contain both albite and quartz inclusions, allowing us to compare calculated pressure estimates relative to the Jadeite + Albite → Quartz reaction line (Holland 1980). The sample is composed of an assemblage of garnet + omphacite + glaucophane + epidote + phengite + albite + quartz + chlorite. Textural evidence suggests that the sample exhibits fluid-catalyzed amphibole (glaucophane) replacement of high-pressure omphacite, indicating that the sample records partial re-equilibration during retrograde blueschist facies metamorphism and possible late-stage fluid infiltration that post-dates blueschist facies metamorphism as suggested by late-stage precipitation of quartz + calcite + albite +

chlorite in garnet pressure shadows and chlorite alteration of garnet porphyroblasts. Therefore, we assume that precipitation of epidote occurs during retrogression and use a conservative T_{ent} estimate of 450 °C. At T_{ent} = 450 °C, P_{ent} for our two albite-in-epidote P_{incl} populations is P_{ent} = 673 ± 179 MPa and 1189 ± 117 MPa (1σ in P_{ent} of inclusion population). The high-pressure albite-in-epidote population are consistent with the reaction of Jadeite + Quartz to Albite at 450 °C (see Fig. 2.4B). Our lower P_{ent} estimates are more enigmatic and may reflect epidote growth during late-stage fluid-infiltration. If so, assuming the same entrapment temperature for both albite populations is incorrect. Previous blueschist facies conditions on Syros have been estimated to range from P ≈ 0.9 – 1.8 GPa and T = 450 – 550 °C (Trotet et al. 2001a). Our results are consistent with previous studies that have indicated blueschist facies conditions on Syros, Greece, but previous work has not indicated if blueschists reflect prograde or retrograde equilibration. Solid mineral inclusion thermobarometry provides the potential to evaluate the differences between estimated PT conditions at a higher, micron-scale resolution.

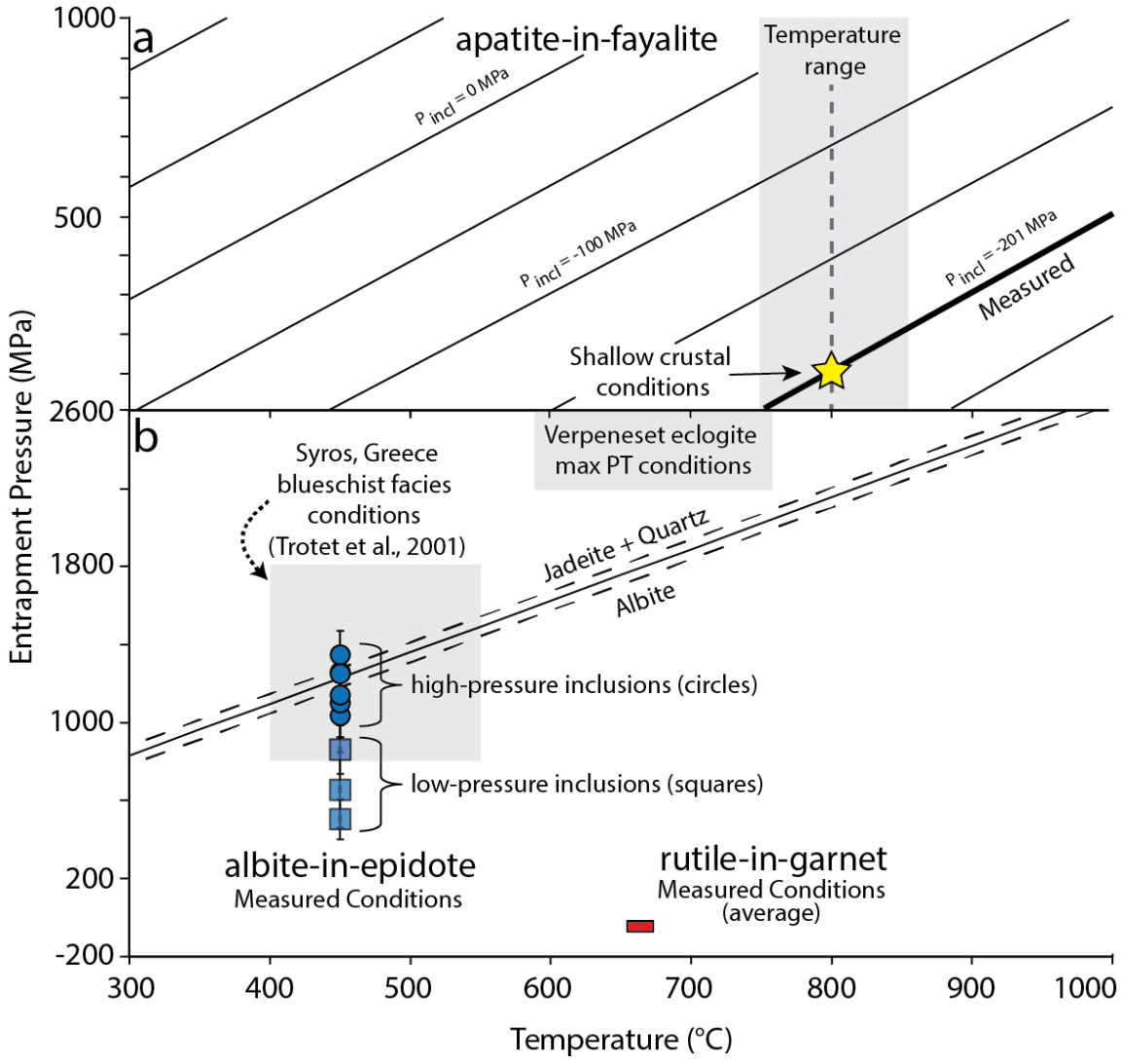

Figure 2.4: Entrapment pressure estimates for the three case studies presented here. **a**) Apatite-in-fayalite results (yellow star) match the previously published reference PT conditions (gray box). **b**) Rutile-in-garnet (red) and albite-in-epidote (blue) pressure estimates from solid inclusion thermobarometry are shown relative to previously determined pressure-temperature constraints (gray boxes). The blue circles and squares indicate the high and low residual inclusion pressure populations, respectively. The yellow star and red square are sized to bracket analytical errors, and errors for albite-in-epidote measurements from Syros, Greece are shown with error bars. The solid black line indicates the position of the Jadeite + Quartz → Albite reaction and adjacent dashed lines bracket the error of the reaction.

2.5 ONGOING DIRECTIONS

The purpose of this work is to make solid mineral inclusion thermobarometry widely available to the community. We believe that this work shows that opportunities with the methodology are plentiful. To demonstrate the vast, untried potential of the technique, we highlight three case studies for magmatic and metamorphic rocks using previously untested minerals. Using those examples, we vulnerably share pitfalls and successes other users will experience. Researchers working on solid mineral inclusion thermobarometry recognize that limitations remain with this technique. Future research is needed to better understand the isotropic and anisotropic effects recorded in residual inclusion pressures, the limitations of 1-dimension elastic modeling, and the effects of non-ideal geometries. Mineral physics experiments are also needed to calibrate the pressure-dependent Raman shifts of additional minerals that may occur as solid inclusions.

Ongoing research is making progress with some of these issues, and many inclusion-host pairs that have not previously been used show promising potential. The best inclusion-host pairs will have dissimilar bulk moduli, thermal expansivities, and compressibilities. Rigid hosts and compressible inclusions make trustworthy barometers, whereas inert hosts and expansive inclusions make the most reliable thermometers. When these elastic differences between host and inclusions minerals are carefully considered then the technique has far-reaching petrologic potential allowing geoscientists to constrain pressure-temperature conditions of processes in diverse mantle, metamorphic, magmatic, and extraterrestrial settings.

Chapter 3: An evaluation of the quartz-in-epidote solid mineral barometer

ABSTRACT

We present the first study to evaluate the suitability of a quartz-in-epidote (qtz-in-ep) solid mineral inclusion barometer. Theoretical calculations applying an isotropic elastic model suggest that the qtz-in-ep barometer exhibits minimal temperature dependence, with the potential to elucidate the growth conditions of epidote in geologic environments with poor pressure-temperature (PT) constraints (e.g., skarn deposits, epidote-bearing granitoids, retrograde metamorphic rocks). To test if the applied equations of state and isotropic elastic model are suitable when simulating the elastic evolution of two anisotropic minerals, we carried out heating measurements and compared Raman spectroscopic shifts of the quartz 464 cm^{-1} band (and therefore inclusion pressure; P_{incl}) with variations of P_{incl} with temperature that are predicted by elastic modeling, for three epidotes derived from samples with well constrained PT histories: 1) sample FT1E from the Frosnitz Tal in Western Tauern (P_{incl} = 6.8 kbar), 2) sample LdC-31C from Lago di Cignana (P_{incl} = 2.6 kbar), and 3) sample HF14C from the Upper Schieferhuelle in Western Tauern (P_{incl} = 0.7 kbar). Entrapment pressures (P_{ent}) calculated from measured P_{incl} at variable T show negligible difference from P_{ent} calculated from modeled P_{incl}, suggesting that for qtz-in-ep pairs, no temperature-dependent correction is required for residual inclusion pressure measurements carried out at ambient temperature. Furthermore, calculated P_{ent} for samples from the Frosnitz Tal and the Upper Schieferhuelle are in excellent agreement with reference PT conditions. Calculated P_{ent} from Lago di Cignana underestimates reference peak pressure conditions by ~20 kbars, and is consistent with early, low P epidote vein precipitation that pre-dates high-P metamorphism or low-P retrogression in the Lago di

Cignana region. This study highlights the potential for future work that can further examine and apply the qtz-in-ep barometer.

3.1 INTRODUCTION

Resolving pressure-temperature (PT) histories of igneous and metamorphic rocks is fundamental for understanding the evolution of the crustal lithosphere. PT conditions are commonly constrained by conventional thermobarometry techniques that include mineral-mineral equilibria, cation exchange, order-disorder of crystals, and stable isotopic compositions, among others. Most of these techniques require chemical equilibrium; however, growing evidence suggests that during metamorphism equilibrium crystallization is unlikely (Carlson 1989, 2015; Rubie 1998; Waters and Lovegrove 2002; Wilbur and Ague 2006; Pattison et al. 2011; Kelly et al. 2013; Spear 2014). Solid (mineral) inclusion thermobarometry constrains the PT conditions at which a host crystal grows and encapsulates an inclusion. Because the elastic properties of the inclusion and host are almost always different, upon exhumation an inclusion can develop residual stress that corresponds to entrapment conditions at higher (or lower) pressures and temperatures. Therefore, the technique requires that changes in inclusion and host volumes from the time of host growth through exhumation to Earth's surface are well constrained. Solid inclusion thermobarometry offers several advantages in comparison to conventional thermobarometric techniques because the method does not rely upon bulk chemical equilibrium or major/trace element cation or isotopic exchange. The method can be used to constrain PT conditions of mineral growth and fabric development, allowing deformation and tectonic processes to be independently constrained. The potential applications of the technique are many, yet it has only been applied to a few inclusion-host

pairs (quartz-in-garnet, Enami et al. 2007; Ashley et al. 2014a; Kouketsu et al. 2014; Spear 2014; Thomas and Spear 2018; apatite-in-garnet, Ashley et al. 2017; olivine-in-diamond, Izraeli et al. 1999; coesite-in-diamond, garnet, and zircon, Parkinson and Katayama 1999; Sobolev et al. 2000; kyanite-in-diamond, Nestola et al. 2018). The quartz-in-garnet (QuiG) inclusion-host pair is the most implemented barometer because of the high compressibility of quartz relative to the rigid host garnet, which allows for retention of significant residual pressures. Additionally, the ubiquity of quartz inclusions in garnet, the stability of garnet across a wide range of conditions in PT space, and the fact that garnet is an isotropic host all make this technique widely applicable. Recent studies have implemented QuiG barometry with much success, and provided novel constraints on formation pressures of garnet from different orogenic belts (Endo et al. 2012; Ashley et al. 2014a; Spear et al. 2014; Wolfe and Spear 2018), however uncertainties still remain in the application of these techniques.

Quartz-in-epidote (qtz-in-ep) is a potentially powerful barometer because: 1) the qtz-in-ep barometer exhibits minimal temperature dependence (Fig. 3.1); 2) epidote is abundant and crystallizes in a broad range of geologic settings (PT conditions); 3) quartz is commonly found as an inclusion within epidote in a wide range of rock types; and 4) the thermodynamic properties of quartz and epidote group minerals are well constrained (Holland et al. 1996; Pawley et al. 1996; Mao et al. 2007; Gatta et al. 2011; Qin et al. 2016). The qtz-in-ep barometer can potentially help elucidate the formation conditions in several environments for which appropriate barometers are not available, including: epidote-bearing skarn deposits, retrograde metamorphic rocks, epidote veins, and hydrothermally altered igneous rocks. A qtz-in-ep barometer represents one of the few barometers that can constrain depths (pressures) of epidote formation in retrograde metamorphic rocks and can

be applied to a wide-range of bulk compositions. Similarly, a qtz-in-ep barometer can supplement existing techniques to determine formation conditions of epidote-bearing skarns.

This study tests the applicability of a qtz-in-ep barometer by comparing entrapment pressure estimates determined by Raman spectroscopy with independent, well-constrained pressure estimates from conventional thermobarometry (Selverstone and Spear 1985; Selverstone et al. 1992; Frezzotti et al. 2011). The methodology used here has the benefit of testing the barometer with natural rocks, but we recognize that our approach is limited by the different processes that barometers record, wherein in solid mineral and conventional thermobarometry records PT conditions of host growth and chemical equilibration, respectively. We follow a similar approach as that implemented in a recent study by Ashley et al. (2016a). Currently, elastic models have been developed for isotropic minerals that assume a spherical inclusion geometry. Furthermore, experiments that determine Raman spectroscopic shifts are carried out under hydrostatic conditions. For the quartz-in-epidote pair, none of these prior assumptions may be correct, therefore necessitating the need for heating measurements of the inclusion-host pair. Heating measurements are carried out to test the ability of the current modeling approach to predict the evolution of inclusion pressure during heating, particularly in systems containing two anisotropic minerals. We compare heating measurements and model results by two methods: 1) the increase in inclusion pressure (P_{incl}) during heating measurements is compared to variations of P_{incl} that are predicted by elastic modeling at elevated temperatures (modeled P_{incl}), and 2) entrapment pressures are calculated from Raman data collected during measurements at elevated temperature and compared to entrapment pressures calculated from modeled P_{incl}.

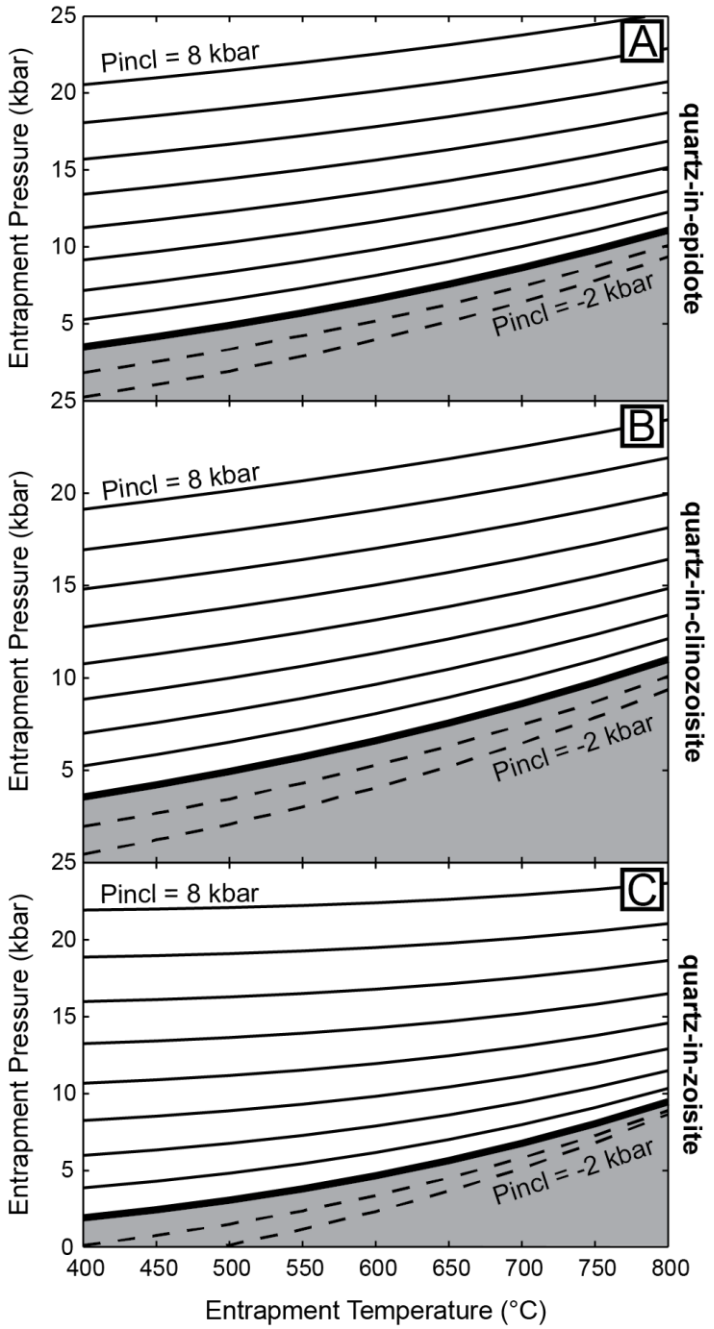

Figure 3.1: Modeled isomekes in P-T space for quartz in (a) epidote, (b) clinozoisite, and (c) zoisite. Modeled isomekes vary over the range of P_{incl} = -2 kbar to 8 kbar (1 kbar intervals) and from 400 ºC – 800 ºC. Regions in grey denote isomekes where assumed P_{incl} is below 0 kbar, wherein quartz preserves a tensile stress.

3.2 SAMPLES

To compare our pressure estimates with those previously determined in other studies, we have selected three samples from various localities that have well constrained PT histories. These samples allow us to test the feasibility of implementing the qtz-in-ep barometer for metamorphic rocks from low-to-high P/T conditions, by comparing if our calculated entrapment pressures are reasonable and consistent with the petrographic context of epidote grains. We note that our samples do not directly allow us to test the potential for the barometer to constrain pressures from high-temperature/low-pressure rocks, such as epidote-bearing skarn deposits and plutonic rocks.

3.2.1 Upper Schierferhuelle – HF14C

Sample HF14C is a metabasalt from the Upper Schieferhuelle in the Western Tauern, Austria, that contains a well-defined foliation defined by amphibole, epidote, quartz, and plagioclase. Reference PT conditions of ~ 500 ºC, and ~7 – 8 kbar have been estimated based on garnet-biotite thermometry (Ferry and Spear 1978; Selverstone and Spear 1985), and garnet-plagioclase-biotite-muscovite barometry (Selverstone and Spear 1985) that uses plagioclase and muscovite inclusions in garnet, garnet core compositions, and matrix biotite.. No biotite inclusions are observed within garnet; therefore, matrix biotite grains are also implemented for temperature constraints, suggesting that these estimates do not reflect the temperature during the onset of garnet growth. Garnet-plagioclase-biotite-muscovite barometry results calculated from garnet rims and matrix grain rims give lower pressure estimates of ~5 – 6 kbars. Epidotes from this sample are oriented parallel to foliation and suggest that precipitation of epidote occurred prior to, or during, foliation-forming deformation (Fig. 3.2A).

3.2.2 Lago di Cignana – LdC-31C

Sample LdC-31C is a psammitic rock from Lago di Cignana, Italy, a region that has experienced ultra-high-pressure metamorphism as evidenced by a diamond-bearing horizon. Estimated PT conditions reach up to 600 ºC and minimum pressure estimates range from 32 - 34 kbar (Frezzotti et al. 2011). The foliation is defined by quartz, epidote and white mica; however, epidote from this sample is derived from a coarse-grained epidote vein that exhibits an irregular, undulating contact with the primary foliation (Fig. 3.2B). The serrated boundary suggests that the epidote derived from the deformed vein may have precipitated prior to the primary foliation-forming event in the region.

3.2.3 Frosnitz Tal – FT1E

Sample FT1E is a psammitic rock from Frosnitz Tal in the Tauern, Austria, eclogite zone that contains a well-defined foliation defined by quartz, epidote, white mica, omphacite, and chlorite (Fig. 3.2C). Reference PT conditions indicate a main phase of equilibration at ~ 625 ºC and ~19 - 24 kbar based on multiple thermobarometric techniques (Spear and Franz 1986; Selverstone et al. 1992). Epidotes from this sample are oriented parallel to the primary foliation, suggesting crystallization of epidote occurred prior to, or during, the primary fabric forming deformation.

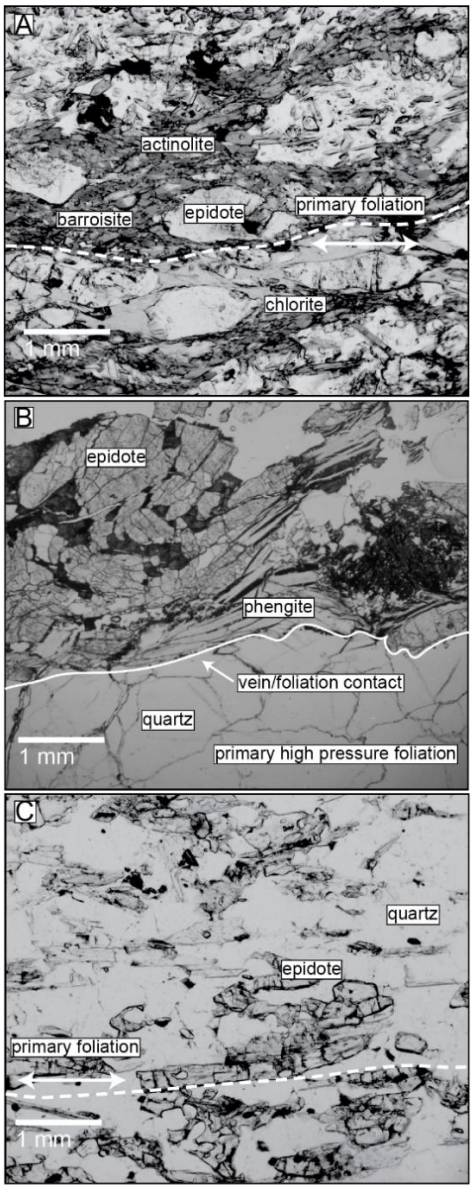

Figure 3.2: Photomicrographs of thin sections showing the petrographic relationships of epidotes analyzed in this study. A) HF14C: foliation parallel epidote grains suggest that epidote likely grew prior to or during deformation associated with formation of the primary foliation. B) LdC-31C: analyzed epidotes are from a vein that has an irregular, undulating contact with the primary foliation. The petrographic relations suggest that epidote crystallized prior to formation of the HP/LT foliation, or during exhumation. This fabric suggests that epidotes should record formation pressures below high-pressure crystallization conditions. C) FT1E: epidote grains aligned parallel to foliation, suggesting that crystallization occurred prior to or during the formation of the primary foliation.

3.3 MEASUREMENT PROCEDURES

To test the suitability of applying an isotropic elastic model when modeling two anisotropic phases, and the ability of the equations of state to model molar volumes, we carried out heating measurements on our three samples. Samples were prepared by doubly-polishing single epidote crystals that were individually loaded onto a heating stage for Raman analyses. The diameter of measured quartz inclusions ranged from 10 – 15 μm, and significant care was taken to select isolated inclusions that were away from fractures, cleavage or other inclusions, and at least 3 times the inclusion radial distance from the host exterior (surface) to avoid relaxation of the stressed inclusion (Mazzucchelli et al. 2018).

Heating measurements were completed at Virginia Tech on a Linkam THMSG600 heating stage mounted onto a JY Horiba LabRam HR800 Raman spectrometer with 1800 lines/mm grating. We used a 40x objective with a confocal aperture of 400 μm and a 150 μm slit width. Raman spectra were centered at 360 cm^{-1} (total spectral range of ~74 – 633 cm^{-1}). A 514.57 nm wavelength Ar laser with the laser interference filter removed was used for all analyses. An unfiltered laser beam allowed us to simultaneously correct measurements for drift by monitoring the position of the Ar plasma lines and applying a linear drift correction dependent on the position of the 520.30 cm^{-1} Ar plasma line. Instrument standardization was carried out by measuring the position of the quartz 464 cm^{-1} peak in a Herkimer quartz standard 5 times prior to analysis. The quartz 464 cm^{-1} peak shift reflects the Si-O-Si stretching mode and this Raman peak was used because it exhibits a prominent frequency shift and has a high intensity (Hemley 1987; Schmidt and Ziemann 2000). For samples LdC-31C and FT1E, the 464 cm^{-1} band was the only band peak-fitted for quartz inclusions because the quartz 128 and 206 cm^{-1} bands exhibited low intensities or had significant overlap with epidote peaks. For sample HF14C, we were able to reliably

measure the quartz 206 cm^{-1} band and calculate an inclusion pressure that we compare with the 464 cm^{-1} band (ν_{464}) in the results section. All the heating measurement data was fit by using PeakFit v4.12 (by Systat Software Inc). A Gaussian amplitude model was used to fit Ar plasma lines, and the Pearson IV model was used to fit the ν_{464} band, following the approach of Schmidt and Ziemann (2000). Due to the overlap of the 464 cm^{-1} quartz peak and lower frequency epidote bands at ~ 422 cm^{-1} and 451 cm^{-1}, we applied multiple peak fitting approaches. The interference is the result of quartz wavenumber shifts with P and T resulting in overlap of the quartz 464 cm^{-1} peak with shouldering epidote bands (particularly at higher T). For all samples, no variation in peak width or shape was allowed because convergence of the quartz and epidote peaks causes unrealistic asymmetry of the fitted quartz 464 cm^{-1} peak at high temperatures (see Schmidt and Ziemann 2000). We used one, two or three peaks to fit the quartz 464 cm^{-1} and shoulder epidote peaks. The number of peaks chosen depended on the quartz 464 cm^{-1} peak intensity and the ease with which it could be resolved from the epidote shoulder peaks. If quartz 464 cm^{-1} intensities were similar to epidote intensities, resolving epidote and quartz Raman bands required two or more peaks due to broadening of the quartz peak if only one peak was used for fitting. For sample FT1E, 2 peaks were required to fit a shoulder epidote peak and the quartz peak. The intensity of the quartz 464 cm^{-1} peak was strong relative to the epidote peak for sample LdC-31C and only required 1 peak to fit the quartz data. The intensity of the 464 cm^{-1} peak in sample HF14C was low and required 3 peaks to fit the two shoulder epidote peaks and the quartz 464 cm^{-1} peak. The propagated errors reported in this study account for errors in peak fit statistics for the Ar plasma line, quartz 464 cm^{-1} peak, and instrument uncertainty (~0.1 cm^{-1}).

Heating measurements on all samples were performed at ambient pressure, from room temperature to 600 ºC. Raman shifts of quartz inclusions were measured at 50 ºC increments, with subsequent cooling measurements to ensure that plastic deformation had not occurred during heating. Shifts of the quartz (inclusions) 464 cm^{-1} position at elevated temperature were calculated relative to frequency shifts of Herkimer quartz at 1 bar and measurement temperature (Ashley et al. 2016). Low-P inclusions used the full polynomial T-$\Delta\nu_{464}$ equation by Ashley et al. (2016a); because of the pressure dependence of the quartz α-β transition; high P_{incl} samples used the linear extrapolation proposed by Ashley et al. (2016). Inclusion pressure was calculated using the polynomial regression by Ashley et al. (2014a), based on the experimental data of Schmidt and Ziemann (2000), assuming pressure dependence does not significantly change at elevated T. Quartz inclusions in epidote record a smaller Raman shift with heating relative to Herkimer quartz at ambient pressure because of increasing inclusion pressure. The increasing Raman frequency shifts (increasing 464 cm^{-1} wavenumber) of inclusions relative to Herkimer quartz reflects the pressure increase of encapsulated quartz during heating due to its higher thermal expansivity relative to epidote

Electron probe microanalysis (EPMA) was carried out at the University of Texas at Austin on a JEOL 8200 instrument equipped with five wavelength-dispersive spectrometers. Epidotes were analyzed for Na, Al, K, Mn, Ti, Mg, Si, Ca, Fe, and Cr using a 10-μm beam size, 10 nA beam current and 15 keV accelerating voltage. All elements were measured for 30 s on peak and a mean atomic number background correction was applied. Primary standards were synthetic anorthite glass, synthetic orthoclase, natural chromite from the Stillwater complex (531M-8), synthetic enstatite, natural Amelia-albite from Amelia, Virginia and ilmenite from the Ilmen Mountains, USSR (USNM96189).

Analyses were monitored by analyzing Kakanui hornblende as a secondary standard, using the same operating conditions as for the unknowns. All iron in epidotes was assumed to be ferric. Chemical compositions of unknown analyses and epidote end-member mole fractions are given in Table 3.1.

Sample	FT-1E	1σ	LdC-31C	1σ	HF-14c	1σ
# n	*17*		*15*		*15*	
Al_2O_3	27.95	1.39	26.80	1.72	25.22	1.79
MnO	0.12	0.09	0.44	0.17	0.12	0.06
TiO_2	0.12	0.06	0.06	0.06	0.06	0.06
SiO_2	38.69	0.38	38.51	0.35	38.16	0.43
CaO	23.63	0.22	23.34	0.46	23.69	0.30
FeO	7.70	1.52	9.05	2.26	10.33	2.28
CrO	0.06	0.04	0.02	0.01	0.04	0.04
Total	98.33	0.35	98.20	0.31	97.70	0.36
Cation sums‡*						
Al	2.54	0.04	2.45	0.04	2.33	0.08
Mn	0.01	0.005	0.03	0.009	0.01	0.004
Ti	0.01	0.003	0.00	0.003	0.00	0.003
Si	2.98	0.07	2.98	0.1	2.99	0.07
Ca	1.95	0.05	1.94	0.04	1.99	0.06
Fe+3	0.50	0.08	0.59	0.11	0.68	0.04
Cations	7.98		7.99		8.00	
Xep	**0.48**	0.02	**0.57**	0.02	**0.67**	0.04
Xcz	**0.52**	0.02	**0.43**	0.02	**0.33**	0.04

***n*** denotes the number of individual of analyses

‡Mineral formula (apfu) is calculated on the basis of 12.5O

*All Fe is assumed to be Fe^{3+}

Table 3.1: Average composition (wt %) of epidote group minerals

Entrapment pressures were calculated by implementing the Guiraud and Powell (2006) 1-D elastic model with a correction addressed by Angel et al. (2017b), following the equation:

$$\left[\left(\frac{V}{V_0}\right)_{incl} - \left(\frac{V}{V_0}\right)_{host}\right]\left(\frac{V_0}{V_{foot}}\right)_{incl} - \frac{3}{4G_{host}}(P_{incl} - P_{ext}) = 0$$

Where $(V/V_0)_{incl}$ and $(V/V_0)_{host}$ are the molar volume ratios of the entrapped inclusion and the host at measurement conditions (V), and at entrapment conditions (V_o), respectively. $(V_0/V_{foot})_{incl}$ is the inclusion molar volume ratio at measurement conditions, and at a measurement temperature and a pressure along an isomeke defined by the entrapment conditions (see Angel et al. 2017b). G_{host}, P_{incl}, and P_{ext} are the shear modulus of the host, the inclusion pressure at ambient T, and the pressure of the host at ambient T (1 bar), respectively. Molar volumes for quartz were calculated by using the Angel et al. (2017a) quartz constants, and by following their curved boundary model approach. The Angel et al. (2017a) thermodynamic properties (Table 3.2) provide a better fit to quartz experimental data and provide a softening of both alpha and beta quartz, reducing entrapment pressure estimates for all samples relative to estimates that use the Holland and Powell (2011) quartz constants. The Tait EOS and thermal pressure correction from (Holland and Powell 2011) were used to calculate epidote group mineral molar volumes. Thermodynamic properties of epidote and clinozoisite were derived from the experimental PT molar volume data of (Gatta et al. 2011), and (Holland et al. 1996; Pawley et al. 1996), respectively. Experimental molar volume P-T-V data were fit with the modified Tait EOS of Holland and Powell (2011) by using EOSFit7c (Angel et al. 2014a) to calculate the elastic moduli of epidote and clinozoisite. For zoisite we use the reference bulk modulus

and thermal expansivity given in Holland and Powell (2011) (all thermodynamic properties are listed in Table 3.2). Shear modulus values for epidote, clinozoisite, and zoisite were calculated by using the aggregate Poisson's ratio of 0.26 suggested by Mao et al. (2007) and the experimentally determined bulk moduli (Table 3.2). The shear modulus equation for an isotropic material is:

$$G = \frac{3K(1-2\nu)}{2(1+\nu)}$$

where G is the shear modulus, K is the bulk modulus, and ν is the poisson ratio. This approach provides a shear modulus value for epidote of 60.9 GPa, calculated from the (Gatta et al. 2011) bulk modulus, that closely approximates experimentally determined values (e.g., 61.2 GPa, (Ryzhova et al. 1966). As a secondary example, we calculate a shear modulus for zoisite of 71.6 GPa based on the experimental bulk modulus value from (Mao et al. 2007). Our calculation closely approximates their experimentally determined shear modulus of 72.9 GPa. The small differences between experimentally-derived and estimated shear moduli have nominal effects on calculated entrapment P (well below the resolution of the barometer). We are not aware of experimental shear modulus data for clinozoisite; therefore, to keep internal consistency, we calculated shear modulus values by using equation 2 and our experimentally refined bulk moduli. Using our thermodynamic properties derived from re-fit experimental data and the approach described above, we calculate and use the following shear moduli values: G_{host} = 72.8 GPa (epidote), G_{host} = 81.5 (clinozoisite), and G_{host} = 59.7 (zoisite). Ideal mixing was assumed between epidote and clinozoisite to calculate the molar volume and shear modulus of solid-solution compositions. The linear scaling approximation between epidote and clinozoisite underestimates non-ideal mixing molar volumes, due to the positive excess volume associated with epidote mixing; however, linear scaling of epidote and clinozoisite molar

volumes and shear moduli was important for providing the best estimates of P_{incl} values predicted by elastic modeling (modeled P_{incl}), and for calculating entrapment pressures. For example, an entrapment pressure calculated for pure end-member epidote (assuming T = 500 °C, P_{incl} = 3 kbar), provides a formation pressure of 10.3 kbar, whereas linear mixing of X_{ep} 0.5 (X_{cz} = 0.5), reduces entrapment pressures to 10.1 kbar. The ~200 kbar higher bulk modulus of clinozoisite can alter entrapment pressure estimates when mixing of end-members is not incorporated. Modeled P_{incl} at elevated T is calculated by determining a residual quartz P_{incl} at ambient T from Raman measurements, calculating P_{ent} from ambient P_{incl} (and an assumed entrapment temperature), and subsequently back-calculating P_{incl} at elevated T from the determined entrapment pressure. The potential of the qtz-in-ep barometer is highlighted by isomekes that show the minimal temperature dependence of entrapment pressures (Fig. 3.1).

Phase	**V_0 (cm^3 mol^{-1})**	**α_0 (10^5 K^{-1})**	**κ_0 (GPa)**	**κ_0'**	**$\kappa_0'' = -\kappa_0'/\kappa_0$**	**$\delta\kappa/\delta T$ GPa K^{-1}**	**ν (poisson ratio)**	**G (GPa)**
Quartz	2.374▪	-0.47▪	64.28▪	5.07▪	-0.0079	0.016		
Clinozoisite	13.649‡	2.16‡	142.6‡	8.44‡	-0.0060	-	0.26•	81.5
Epidote	13.810†	2.30†	127.4†	3.26†	-0.0026	-	0.26•	72.8
Zoisite	13.580*	3.12*	104.4*	4.00*	-0.0038	-	0.26•	59.7

All thermodynamic properties are given at standard state: 0.1 MPa, 298 K

References from which thermodynamic and physical properties are derived or calculated:

▪Angel et al., 2017

*Holland and Powell, 2011

‡Holland et. al, 1996

†Gatta et al., 2011

•Mao et al., 2007

Table 3.2: Thermodynamic and physical properties of quartz, clinozoisite, epidote and zoisite

3.4 RESULTS AND DISCUSSION

3.4.1 Heating measurement results

Here, we present the quartz inclusion frequency shifts and the host compositions determined for our suite of samples. Compositions of epidote from the three samples are listed in Table 3.1. Samples display solid-solution compositions between epidote and clinozoisite end-members that range from X_{ep} = 0.48 - 0.67 (Table 3.1). All quartz inclusions exhibited a shift in the 464 cm^{-1} band position to lower wavenumbers with increasing temperature but show a positive deviation relative to an ambient pressure Herkimer quartz standard (Fig. 3.3). The epidote shoulder wavenumber and the number of shoulder peaks varied depending on the epidote composition, requiring modification in the number of peaks needed to accurately de-convolve the quartz and epidote peaks. At elevated temperatures, we encountered difficulties in separating the quartz 464 cm^{-1} band and shoulder epidote peaks due to the convergence resulting from the T-sensitivity of the quartz band (Table 3.3; Fig. 3.4). Sample HF14C displayed the largest increase in P_{incl} owing to its low inclusion pressure and the proximity of quartz to the α-β transition at higher temperature measurements. As a result, sample HF14C was the most problematic for fitting the quartz 464 cm^{-1} band because of its initial proximity to the lower frequency epidote Raman peaks. For sample HF14C, P_{incl} that was calculated by using measurements at elevated temperatures underestimated modeled P_{incl} (P_{incl} predicted by elastic modeling at elevated T) significantly at low to moderate temperatures; however, the general trend from modeled inclusion pressures is matched by P_{incl} calculated from measurements at high temperatures (Fig. 3.5). In comparison, samples that retain higher quartz inclusion pressures (LdC-31C and FT1E) undergo less increase in P_{incl} during heating measurements. P_{incl} values calculated during heating for samples FT1E and LdC-31C correlate well with

modeled inclusion pressures at low to moderate temperatures (Fig. 3.5). Above these temperatures, it became more difficult to de-convolve the quartz 464 cm^{-1} band from the epidote Raman peaks. For sample HF14C, it is unclear if the lower P_{incl} values of heating measurements reflect an overestimation of P_{incl} by the elastic model and associated EOS's; therefore, we do not use these inclusion pressures to assess the need for a correction of the entrapment pressure. A recent study noted that modeled quartz inclusion pressures exhibit excess pressures relative to inclusion pressures calculated during heating measurements (Ashley et al. 2016). Based on P_{incl} calculated from the lower temperature measurements of samples FT1E and LdC-31C, our results suggest that even for anisotropic minerals, application of the Tait EOS and/or Berman thermal EOS, and an isotropic elastic model, satisfactorily simulate P_{incl} evolution in this study, during exhumation to the Earth's surface of quartz entrapped in epidote.

		$\Delta\nu_{464}$ (cm^{-1})			Inclusion	Entrapment		
Sample	T (°C)	Measured	Corrected	Error (cm^{-1})	Pressure (GPa)	Error (GPa)	Pressure (GPa)	Error (GPa)
Frosnitz Tal: FT1E	23.7	6.04†	6.08	0.20	0.68	0.02	1.95	0.06
	50	5.37†	5.75	0.20	0.64	0.02	1.84	0.05
	50*	6.56†	6.94	0.21	0.78	0.02	2.14	0.06
	100	4.76†	5.85	0.20	0.65	0.02	1.83	0.05
	100*	5.43†	6.52	0.21	0.73	0.02	2.00	0.06
	150	4.01†	5.87	0.21	0.66	0.02	1.80	0.05
	200	3.71†	6.38	0.22	0.71	0.02	1.88	0.06
	250	3.69†	7.17	0.27	0.81	0.03	2.04	0.08
	250*	3.50†	6.98	0.23	0.78	0.03	1.99	0.07
	300	2.58†	6.84	0.24	0.77	0.03	1.91	0.07
Lago di Cignana: LdC-31C	23.7	2.31	2.34	0.20	0.26	0.02	1.00	0.04
	23.8	2.37	2.41	0.20	0.27	0.02	1.02	0.04
	50	2.22	2.60	0.20	0.29	0.02	1.04	0.04
	100	1.43	2.52	0.21	0.28	0.02	0.99	0.04
	100*	1.30	2.39	0.20	0.26	0.02	0.96	0.04
	150	0.88	2.74	0.21	0.30	0.02	1.00	0.04
	200	0.26	2.92	0.25	0.32	0.03	1.00	0.05
	200	-0.05	2.61	0.21	0.29	0.02	0.93	0.04
Upper Schierferhuelle: HF14C	22.5	0.66	0.68	0.20	0.07	0.02	0.61	0.04
	50	0.24	0.62	0.20	0.07	0.02	0.59	0.04
	100	-0.50‡	0.59	0.20	0.06	0.02	0.55	0.04
	100*	-1.18‡	-0.09	0.21	-0.01	0.02	0.43	0.04
	150	-1.29‡	0.57	0.20	0.06	0.02	0.51	0.04
	200	-1.92‡	0.74	0.21	0.08	0.02	0.50	0.04
	200*	-2.19‡	0.47	0.21	0.05	0.02	0.45	0.04
	250	-2.44	1.03	0.22	0.11	0.02	0.51	0.04
	300	-3.05‡	1.22	0.22	0.13	0.02	0.50	0.04
	300*	-3.52‡	0.74	0.25	0.08	0.03	0.41	0.05
	350	-3.27‡	1.74	0.26	0.19	0.03	0.55	0.05
	400	-3.80‡	1.90	0.25	0.21	0.03	0.51	0.05
	400*	-3.91‡	1.79	0.45	0.20	0.05	0.49	0.09
	450	-3.68‡	2.61	0.31	0.29	0.03	0.59	0.07
	500	-2.38‡	4.38	0.53	0.49	0.06	0.90	0.13
	500*	-3.28‡	3.48	0.41	0.39	0.05	0.69	0.09
	550	-3.72‡	3.37	0.47	0.37	0.05	0.56	0.11
	600	-3.28‡	3.98	0.41	0.44	0.05	0.57	0.10

None of the peak fitting implemented variations in peak width or shape

Unless otherwise noted, 1 peak was used to peak fit the Raman spectra

* cooling experiment

† 2 peaks were used to fit the data; ‡ 3 peaks were used to fit the data

Table 3.3: Frequency shifts, experimental inclusion pressures, and calculated entrapment pressures during heating

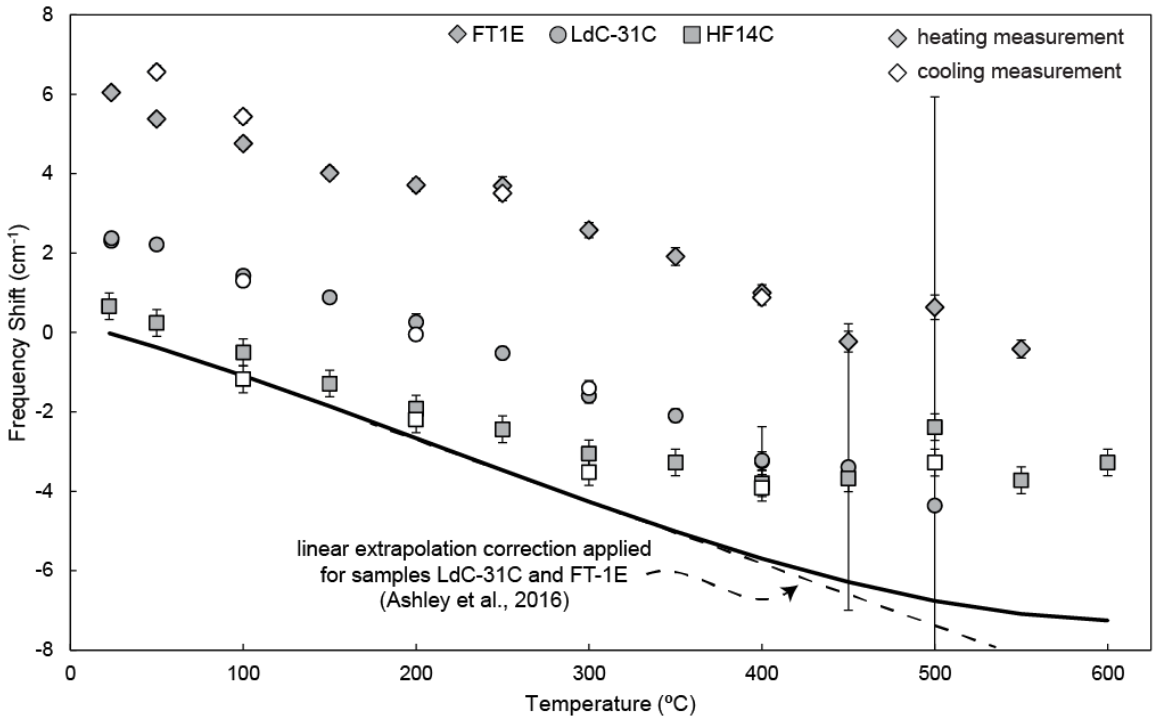

Figure 3.3: Measured frequency shifts for the three samples used during heating. All samples display a decrease in wavenumber with increasing temperature. Relative to ambient Herkimer quartz, all samples exhibit a smaller frequency shift due to an increase in inclusion pressure with increasing temperature. The solid line is derived from the reference polynomial equation for the frequency shift changes of Herkimer quartz at 1 bar and a measurement T (Ashley et al. 2016). The dashed line is the linear extrapolation of the polynomial equation that we used for correcting frequency shifts from samples LdC-31C and FT-1E relative to Herkimer quartz at measurement conditions. Error bars are propagated errors from instrument uncertainty, and errors associated with fitting quartz 464cm^{-1} bands and the Ar plasma line. Symbols represent the following samples: FT1E (triangle), LdC-31C (circle), HF14C (square).

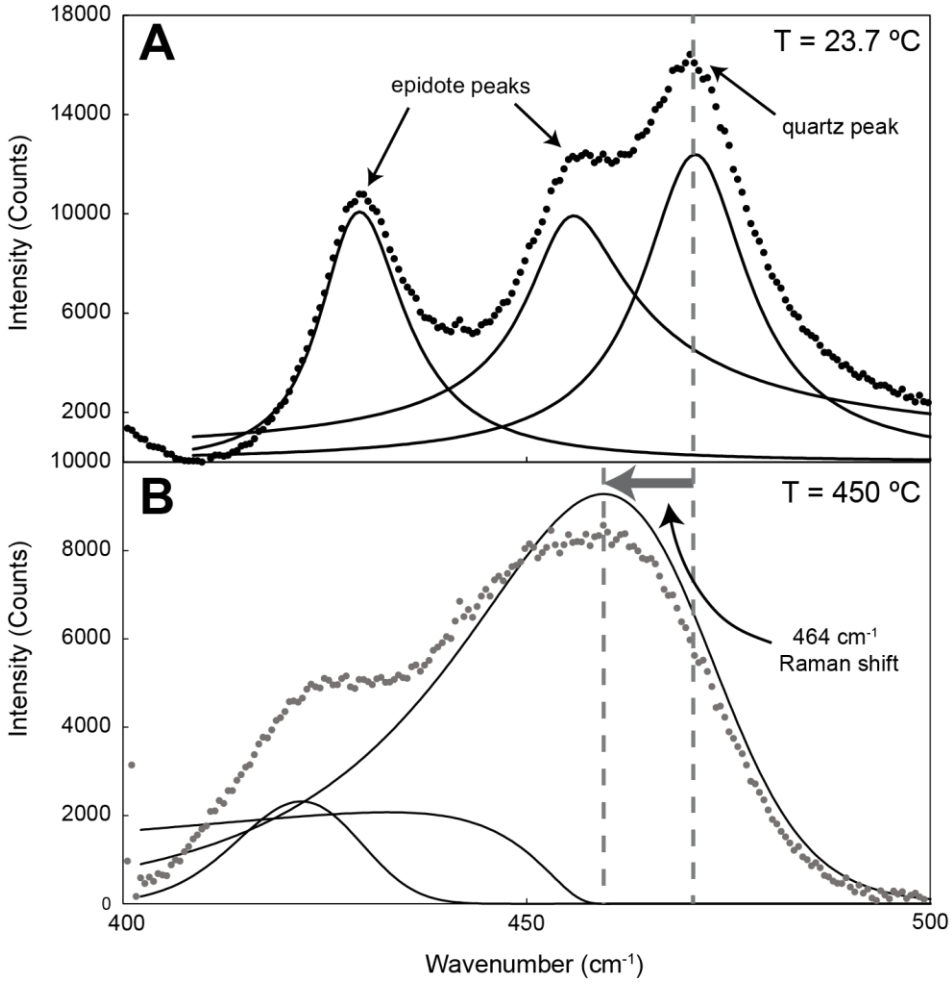

Figure 3.4: Raman spectra of sample FT1E at (a) ambient temperature (23.7°C) and (b) 450 ºC, over the wavenumber range from 400 to 500 cm^{-1}. Shown in circles are the raw data at both temperatures, and solid lines indicate the three peaks used to fit the low and high temperature data. At 450°C, the quartz 464 cm^{-1} Raman band exhibits a shift to lower wavenumbers and overlaps with the epidote shoulder peak. The difficulty in separating the two peaks leads to large uncertainty in the quartz 464 cm^{-1} peak position and associated inclusion pressure. Note, that for measuring 464 cm^{-1} peaks from the quartz inclusion in epidote for this sample, only the 464 cm^{-1} peak and the neighboring epidote peak were fit.

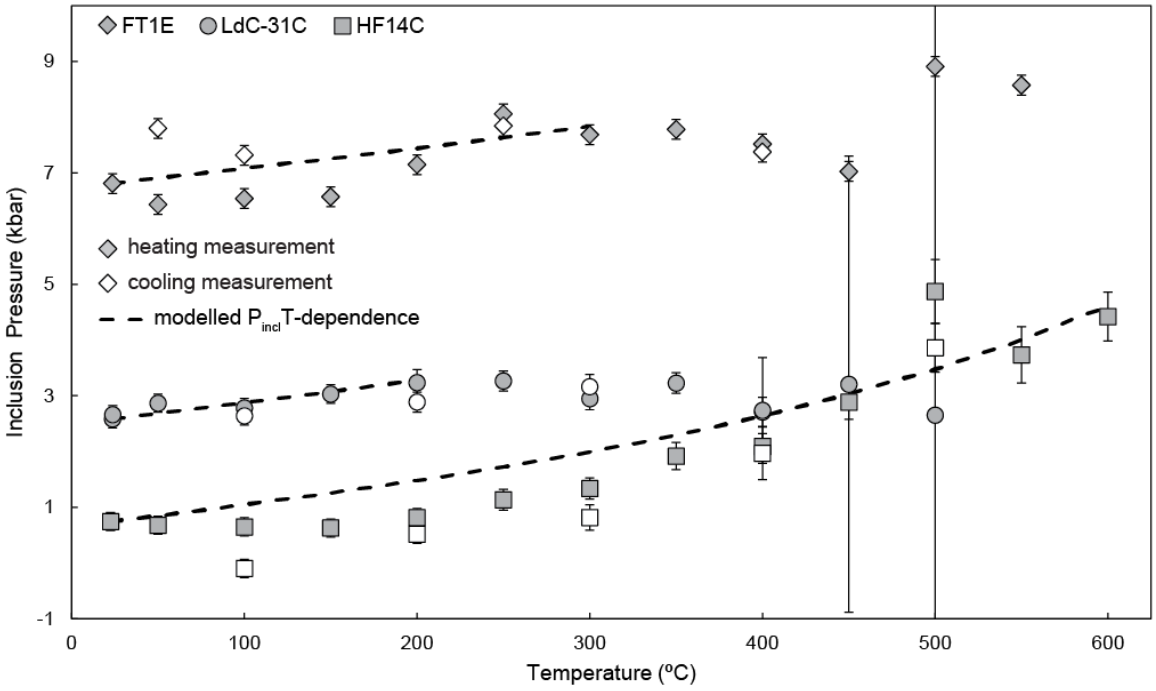

Figure 3.5: Inclusion pressures calculated from heating measurements, compared to the inclusion pressure evolution predicted by elastic modeling with increasing temperature (modeled). The dashed lines represent the modeled inclusion pressure based on the Angel et al. (2017a) quartz constants. Symbols represent the following samples: FT1E (triangle), LdC-31C (circle), HF14C (square).

3.4.2 Evaluation of calculated entrapment pressures at elevated temperatures

To evaluate the reliability of the elastic model and equations of state, we calculate entrapment pressures from inclusion pressures derived at elevated temperatures. Entrapment pressures calculated from inclusion pressures at each heating step are shown in Figure 3.6. Much of the deviation in the calculated entrapment pressures at a given temperature is attributed to errors in fitting of low intensity quartz peaks. For samples FT1E and LdC-31C, we extend entrapment pressures calculated from P_{incl} during heating measurements up to temperatures where P_{incl} values are reliable (Fig. 3.6). Nevertheless,

for moderate-to-high pressure samples FT1E and LdC-31C, entrapment pressures calculated for heated inclusions exhibit only small differences in calculated entrapment pressures relative to those collected from Raman data at 25 °C, suggesting that temperature corrections to modeled entrapment pressures are not needed for the qtz-ep inclusion-host pair (Fig. 3.6). Best fit lines that were fit to entrapment pressures calculated from inclusion pressures determined from Raman shifts at elevated T, exhibit a slope that is similar to that for the evolution of entrapment pressures with increasing temperature (calculated from P_{incl} variation predicted by elastic modeling). Low pressure sample HF14C showed the largest variation in calculated entrapment pressures, and measurements result in lower entrapment pressures relative to theoretical estimates at low temperatures. Large uncertainties are associated with many measurements from samples HF14C due to the overlap of the quartz 464 cm^{-1} peak with shoulder epidote peaks, making peak de-convolution difficult. We do not use HF14C measurements to assess the need for a thermal correction to entrapment pressure calculations when using the qtz-in-ep barometer.

3.4.3 Comparison of calculated entrapment pressures to reference PT constraints

To assess the potential for the quartz-in-epidote barometer to constrain pressures of epidote growth, we compare our results to previously constrained PT conditions for our samples. We do not apply a temperature-dependent correction to the calculated formation pressures. We provide entrapment pressures calculated using the quartz constants from Angel et al. (2017). Relative to the (Holland and Powell 2011) quartz properties, for inclusions that preserve higher pressures, the difference between entrapment pressures from both sets of quartz constants is minimal, whereas calculated entrapment pressures for low pressure quartz inclusions exhibits differences in entrapment pressures of ~ 1 kbar.

3.4.3.1 Upper Schierferhuelle – HF14C

Sample HF14C preserves foliation parallel epidotes that appear to have crystallized pre-or-syn-kinematic to fabric forming deformation (Fig. 3.2A). Therefore, we suggest that PT estimates of this sample should closely agree with PT constraints derived from conventional cation exchange thermobarometry. Epidotes retain quartz inclusions with residual pressures of P_{incl} = 0.74 kbar (based on the quartz 464 cm^{-1} shift). For comparison, measurement of the quartz 206 cm^{-1} band Raman shift leads to a calculated residual inclusion pressure of P_{incl} = 0.75 kbar. The similar inclusion pressures calculated from different quartz Raman band shifts suggest that this quartz retains an isotropic stress and can confidently be used for estimating entrapment pressures (i.e., nominal strain anisotropy within the inclusion; Murri et al. 2018)). Assuming an entrapment temperature of 500 ºC, we estimate an entrapment pressure of 6.14 ± 0.38 (1σ) kbar. Our calculated results slightly underestimate reference formation conditions of P = 7 - 8 kbar at T ≤ 500 ºC in the Upper Schieferhuelle in the Western Tauern derived from garnet-plagioclase-biotite-muscovite barometry, using garnet core compositions, plagioclase and muscovite inclusions in garnet, and matrix biotite (Selverstone and Spear 1985). Epidote formation in this sample may post-date garnet growth, thus recording later, lower pressure conditions associated with epidote crystallization during decompression. Our calculated entrapment pressure is in better agreement with estimated conditions of garnet rim growth (~5 - 6 kbar), obtained from garnet rims and matrix plagioclase-biotite-muscovite (rims) barometry estimates. Several other explanations are also possible. Alternatively, the temperature estimates for garnet core growth are derived from garnet-biotite thermometry that utilizes matrix biotite grains that may post-date garnet growth, suggesting that the temperature estimates for garnet growth may be too low. Increasing the estimated entrapment temperature by ~60 ºC

places the calculated entrapment pressure within the bounds of prior, independent estimates of 7 – 8 kbar. Conversely, use of matrix biotite grains may lead to calculation of high-or-low reference pressure estimates relative to garnet core growth, depending on the timing of biotite crystallization. Ultimately, we suggest that our epidote crystallization conditions are more consistent with garnet rim and matrix grain PT constraints based on similar estimated PT conditions and the microstructural context of epidote. Although we cannot rule out overstepping during formation of garnet rims and the surrounding matrix, we suggest that the agreement of our results with conventional thermobarometry is promising for future work with the qtz-in-ep barometer.

3.4.3.2 Lago di Cignana – LdC-31C

Quartz from sample LdC-31C retains a residual pressure of P_{incl} = 2.59 kbar. Assuming an entrapment temperature of 550 ºC, we calculate an entrapment pressure of 10.05 ± 0.41 (1σ) kbar. Our results suggest much shallower entrapment conditions than the reported peak metamorphic conditions of 600 ºC and 32 - 34 kbar (within the diamond-bearing horizon at Lago di Cignana; (Frezzotti et al. 2011). Our calculated entrapment pressures would suggest epidote growth early during subduction or retrogressive recrystallization during exhumation. Field and petrographic relationships indicate that our epidote grains may be derived from veins encased in the high-P foliation; therefore, epidote precipitation can represent early vein formation that predates HP/LT metamorphism in the Lago Di Cignana region (Fig. 3.2B). Our thin section displays an irregular, undulating contact between the vein and the surrounding foliation. Our PT estimates for sample LdC-31C are also relatively consistent with a range of retrograde metamorphic conditions that have been suggested by (van der Klauw et al. 1997) (T = 550 - 500 ºC, P ≈ 18 kbar; T =

350 – 450 ºC, P ≈ 3.5 – 5.5 kbar); however, our samples show no evidence for extensive retrogression as shown by the preservation of HP assemblages. Partial epidote recrystallization during exhumation could have also reset HP/LT formation pressures at lower PT conditions.

3.4.3.3 Frosnitz Tal – FT1E

Epidotes from sample FT1E are aligned parallel to the primary foliation, suggesting pre-to syn-tectonic crystallization of epidote (Fig. 3.2C). Quartz inclusions retain a residual inclusion pressure of 6.80 kbar. Assuming an entrapment temperature of 625 ºC, our results suggest a formation pressure of 19.45 ± 0.55 (1σ) kbar. Our results are in excellent agreement with previous PT estimates for the Frosnitz Tal eclogite zone in the Tauern Window that are based on multiple studies that constrain PT conditions in the region (T = 625 ºC, P ≈19 - 24 kbar) (Spear and Franz 1986; Selverstone et al. 1992). Our results suggest that epidote crystallization may have occurred near the PT conditions of chemical equilibrium.

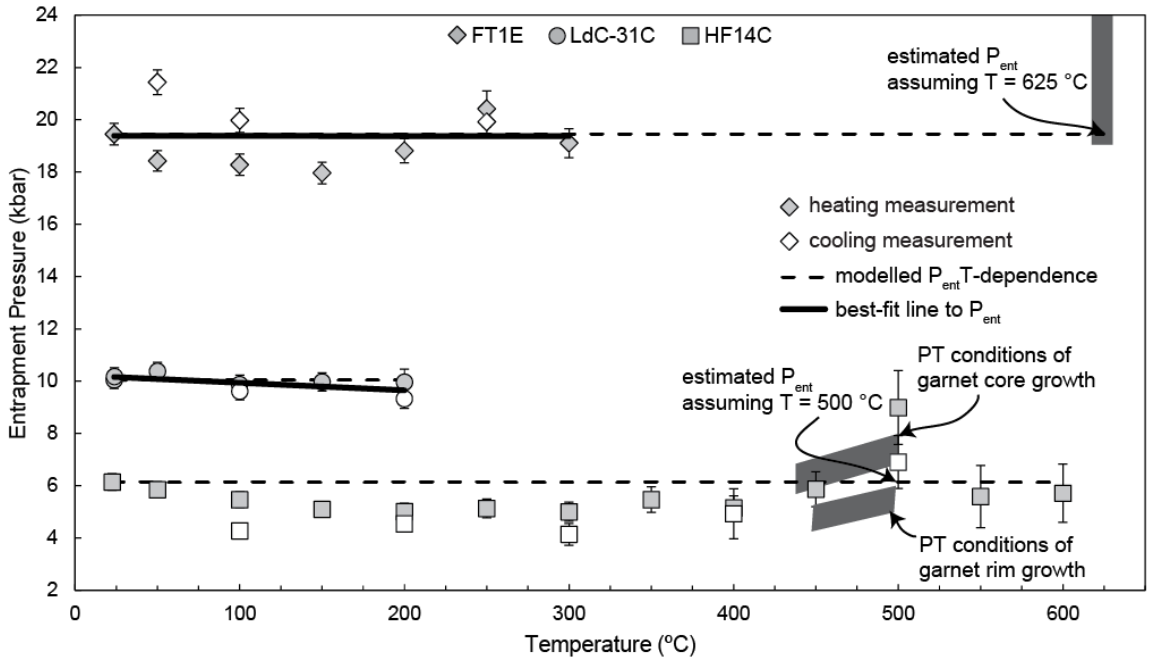

Figure 3.6: Entrapment pressures calculated from P_{incl} determined from Raman shifts during heating, and comparison with model estimates of the temperature-dependence of entrapment pressure (dashed line). Solid lines represent a best-fit line to the entrapment pressures calculated from the evolution of P_{incl} during heating measured in this study. Reference PT conditions for samples FT1E and HF14C and our estimated qtz-in-ep barometry entrapment pressures are shown for comparison. See text for discussion of the reference PT conditions. Symbols represent the following samples: FT1E (triangle), LdC-31C (circle), HF14C (square).

3.4.4 Corrections to thermal component of the elastic model

The agreement between measured and modeled P_{incl} suggests that the elastic model for the quartz-in-epidote barometer does not require thermal corrections. These results are also consistent with a recent study that tests the apatite-in-garnet barometer, and concludes that a thermal correction is not needed for apatite inclusion pressure measurements at ambient temperature that are used to calculate entrapment pressures at higher temperatures (Ashley et al. 2017). In comparison, previous studies have shown that a thermal correction

is required for the QuiG barometer when using the 464 cm^{-1} band for inclusion P determination (Ashley et al. 2016). The ν_{464} band in quartz almost always overestimates inclusion pressure, thus requiring the pressure correction proposed by Ashley et al. (2016a). While the 206 cm^{-1} band gives results most consistent with the computed average stress (an estimate of the hydrostatic component of the stress tensor), estimates based on this broad, low-intensity band typically come at the expense of reduced precision. The difference in results (i.e., no observed offset in measured and theoretical inclusion P with heating) is problematic, given that quartz is the common inclusion phase between the QuiG and qtz-in-ep barometers. P_{incl} given by different quartz inclusion peaks is similar here (hence the theoretical and measured P_{incl} being so similar), but there are significant disparities for quartz in garnet, suggesting significant anisotropy. Perhaps the lower bulk modulus of epidote results in a lower stress anisotropy for the quartz inclusion that isn't detectable. Additionally, because quartz and epidote typically (re)crystallize along a schistosity during fabric development, it may be likely that the orientation of the quartz inclusion relative to the hosting epidote often leads to a bulk stress tensor that optimally characterizes the inclusion P for the system. Regardless, we suggest our results are consistent with the following conclusions: 1) inclusion pressures calculated from the hydrostatic calibration of quartz 464 cm^{-1} Raman band shifts (not valid for anisotropic stress), yield constant entrapment pressures with increasing temperature, 2) allowing for the errors introduced by our modeling for calculating entrapment pressures, our results suggest that the 1D-isotropic model is appropriate for modeling the elastic behavior of these two anisotropic phases, and no further correction is required for P reconstruction (in this case).

3.4.5 Quartz-in-epidote barometry applications

The qtz-in-ep barometer can potentially be applied to epidote-bearing skarn formation, epidote precipitation in ore deposits, epidote-bearing granitoid rocks, hydrothermal alteration of oceanic crust, and growth conditions of epidote in metamorphic rocks from convergent margins. The limitation of the technique lies in the convergence of the 464 cm^{-1} quartz band and shoulder epidote peaks as temperature is increased. For high-T/low-P samples, convergence of the 464 cm^{-1} quartz band may not allow separation of the quartz and epidote bands; perhaps limiting application of qtz-in-ep barometry to epidote crystals that have entrapped quartz under moderate to high pressure conditions. Further analyses on magmatic or skarn epidotes that have well constrained PT conditions might help to refine this model. Nonetheless, the qtz-in-ep inclusion-host pair provides a reliable barometer that can be applied to metamorphic rocks of both continental and oceanic crust origin.

3.5 IMPLICATIONS

A qtz-in-ep barometer is best suited for application with moderate to high-P metamorphic rocks but can likely be applied to understand formation conditions of other geologic environments as well, as long as the quartz 464 cm^{-1} peak can be resolved from shoulder epidote peaks. Qtz-in-ep formation pressures for samples from the Frosnitz Tal eclogite zone and the Upper Schieferhuelle in the Western Tauern are in excellent agreement with previously determined metamorphic PT conditions. Furthermore, our heating measurements suggest that a temperature-dependent entrapment pressure correction is not required, as has been noted for the qtz-in-grt barometer. Therefore, qtz-in-ep entrapment pressures calculated from ambient inclusion pressure measurements can be used to calculate high-temperature entrapment pressures without applying a temperature

correction to the elastic model and molar volume calculations. This result greatly simplifies the application of this method because a high temperature heating stage is not required to obtain the necessary Raman data to implement the model. Our work further highlights how the qtz-in-ep barometer can advantageously be used in the future to constraint PT conditions from distinct structural and textural fabrics.

Chapter 4: Insights into subduction channel exhumation of high-pressure metamorphic rocks by using stable isotopes and solid inclusion barometry

ABSTRACT

We present the first study to utilize solid inclusion barometry to constrain pressure-temperature (PT) conditions of retrograde metamorphic rocks and apply the technique on exhumed subducted material of the Cycladic Blueschist Unit (CBU) exposed on Syros, Greece. Our work utilizes the well-established quartz-in-garnet and the recently tested quartz-in-epidote barometers to constrain pressures of garnet and epidote crystallization. We use oxygen isotope thermometry of quartz and calcite precipitates within boudin necks to calculate temperatures during exhumation and to refine our solid inclusion pressure estimates. Our results reveal three distinct pressure groups that relate to different metamorphic events and textural fabrics: high-pressure garnet-growth at ~ 1.4 - 1.5 GPa and 500 °C, retrograde epidote growth at ~1.3 – 1.4 GPa between 500 - 400 °C, and a second stage of retrograde low-pressure epidote growth at ~1.0 GPa and 400 °C. Our results are consistent with stages of deformation evident in both field and microstructural observations, that record a change of kinematics from N-S prograde stretching lineations, to retrograde stretching lineation fabrics that become re-oriented toward the NE-SW and lastly towards the E-W. Our results indicate that the CBU on Syros underwent incipient cooling during decompression after reaching maximum high-pressure/low-temperature conditions. The determined PT conditions and outcrop observations are consistent with a cold PT evolution that is indicative of exhumation adjacent to a subduction zone boundary, within a subduction channel prior to core-complex capture.

4.1 INTRODUCTION

Constraining the temporal and pressure-temperature (PT) evolution of continental and oceanic crust is fundamental to understanding mechanisms that control the burial and exhumation of rocks. Much of our understanding about the tectonic evolution of the Earth is accomplished by constraining the PT evolution of crustal rocks. Specifically, retrograde metamorphic rocks are a key tool used to understand tectonic processes because they are one of the few rock types that can capture the PT history of rocks throughout exhumation; however, studying these rocks has historically proven challenging for petrologists (e.g., Spear and Pattison, 2017). Often, the conditions under which retrograde rocks form presents several challenges for conventional thermobarometry techniques that require chemical equilibrium, such as sluggish kinetics with decreasing temperatures, partial re-crystallization, and stress effects on metamorphic reactions (e.g., Rubie, 1998; Wheeler, 2014; Jamtveit et al., 2016). Mounting evidence also suggests that partial disequilibrium during metamorphism is likely (e.g., Carlson, 1989, 2002; Pattison et al., 2011).

Solid (mineral) inclusion thermobarometry offers a practical alternative to conventional thermobarometry. The method constrains the PT conditions at which a host crystal entraps an inclusion, and because inclusion-host pair bulk moduli and thermal expansivities commonly differ, upon ascent an inclusion can develop a residual stress that corresponds to entrapment conditions at higher (or lower) pressures and temperatures. The technique has several advantages relative to conventional thermobarometric techniques because the method does not rely upon chemical equilibrium. Furthermore, the determination of mineral growth can advantageously be used to understand the conditions at which individual host minerals precipitate.

This study utilizes the advantages of solid mineral thermobarometry to constrain the PT conditions of mineral growth in high-pressure/low-temperature (HP/LT) metamorphic rocks from Syros, Greece. Syros is an ideal location for applying this technique because although rocks from this locale are commonly utilized for geologic case studies, its exhumation history remains debated, and largely enigmatic. We use the recently studied quartz-in-epidote (qtz-in-ep) barometer, but also the extensively utilized quartz-in-garnet (qtz-in-grt) barometer, and stable isotope thermometry to refine inclusion-host solid mineral pressure estimates and to constrain the PT evolution of a suite of retrograde rocks. Our study elucidates the potential of using solid inclusion barometry to constrain the temporal evolution of PT conditions from distinct textural fabrics and minerals when utilized in combination with structural constraints. Furthermore, this work highlights how future studies can apply similar techniques to constrain the PT conditions of challenging rocks types, from different bulk rocks assemblages.

4.2 GEOLOGIC SETTING

The Cycladic island Syros Greece, located within the Aegean Sea, consists of juxtaposed tectonic slices of oceanic and continental affinity (Fig. 4.1). The rocks dispersed across Syros are associated with Eo-Oligocene subduction (~50 Ma) and Oligo-Miocene to present back-arc extension of the Hellenic arc, and belong to the Cycladic Blueschist Unit (CBU) and a sequence of rocks stratigraphically above the CBU coined the Pelagonian and Vari Units (Keiter et al. 2011; Soukis and Stockli 2013). In this work we focus on rocks within the CBU, which consist of intercalated metavolcanics, metasediments, marbles, metabasites, and serpentinites. Conventional thermobarometry constraints suggest that the entire CBU on Syros reached peak PT conditions of ~1.5 GPa and ~500

°C (Ridley 1984), and developed the spectacular blueschists and eclogites preserved on the island. Trotet et al. (2001) suggested that peak PT conditions of the CBU on Syros were much higher, around ~2.0 GPa and ~550 °C, but more recent work using multi-mineral phase equilibria in marbles and quartz-in-garnet barometry of one metabasic outcrop (Kini beach) supports the more moderate PT estimates of ~1.5 GPa and 500 °C (Schumacher et al. 2008; Behr et al. 2018). Previous work also suggests that a regional metamorphic event occurred around 25-18 Ma and caused retrograde greenschist facies metamorphism (~0.4 - 1.0 GPa, ~450 °C) on all Cycladic islands, but was most pervasive adjacent to large-scale extensional detachment faults (e.g., Bröcker et al., 1993, 2004; Bröcker and Franz, 2006). Despite the documented metamorphic events, the exhumation history of the CBU during the ~25 m.y. period between these two metamorphic events (i.e., between ~50 and ~25 Ma) remains enigmatic; yet, this period spans exhumation of the CBU from subduction pressures of ~1.5 GPa, to the middle crust (~0.3 – 0.7 GPa). The suggested exhumation PT paths for the CBU on Syros are highly variable, ranging from cooling during decompression and complex isothermal decompression (Trotet et al. 2001a; Schumacher et al. 2008). The range of previous PT conditions reflects the lack of comprehensive studies that combine structural geology, petrology, and thermobarometry across the CBU, and the lack of bulk rock assemblages that preserve the entire exhumation history. Because of conflicting PT paths, several models have been proposed to explain the exhumation history of the CBU, such as coaxial vertical thinning (Rosenbaum et al. 2002), extrusion wedge tectonics (Keiter et al. 2011), complex thrusting and extension (Trotet et al. 2001b, 2001a), and subduction channel exhumation (Laurent et al. 2016).

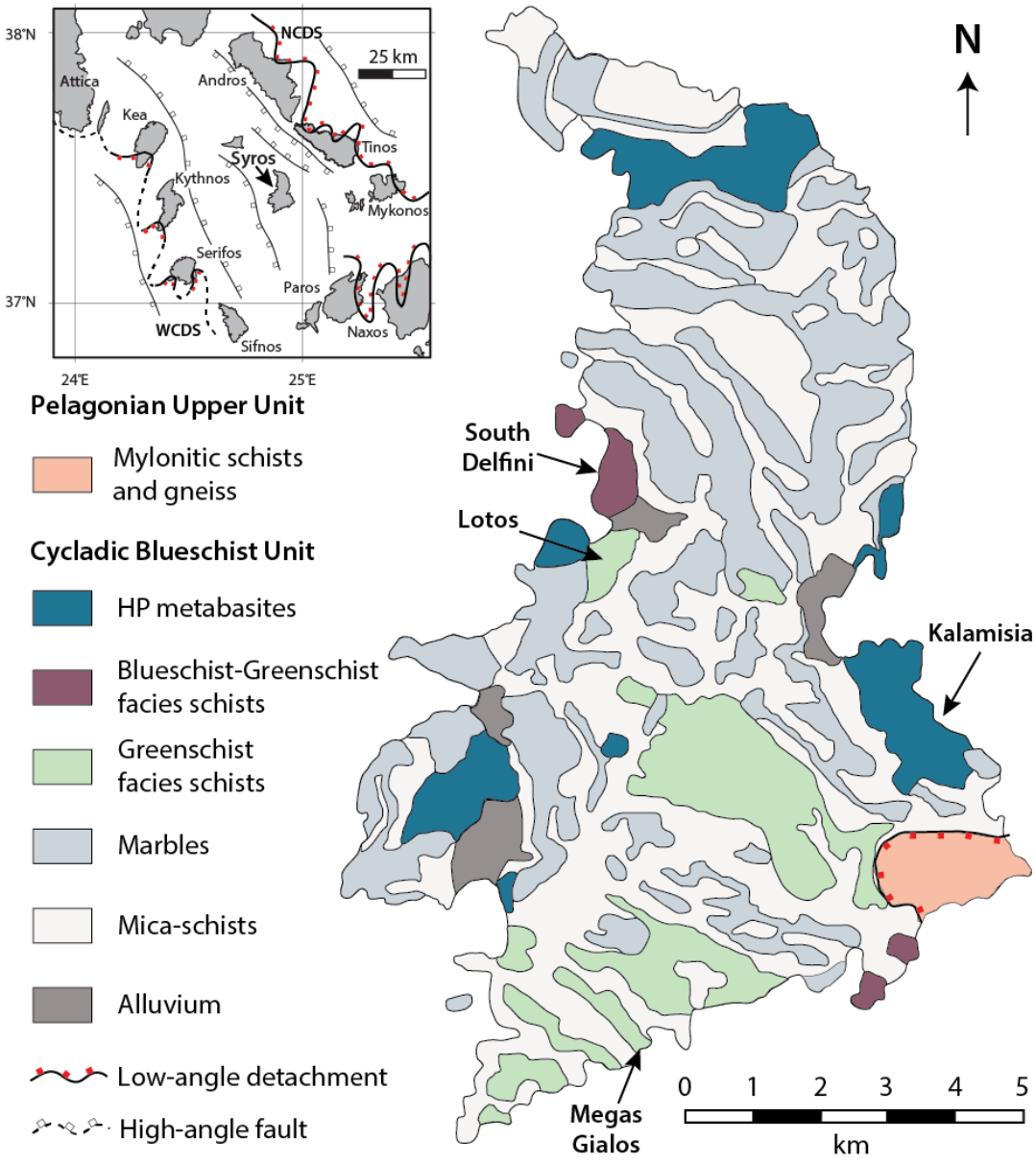

Figure 4.1: Geologic map of Syros, Greece and its location relative to other Cycladic islands [modified from Keiter et al. (2011) and Behr et al. (2018)]. Inset map shows the major North Cycladic Detachment (NCDS) and West Cycladic Detachment (WCDS) Systems. The outcrop locations of our samples are specified by black arrows.

4.3 Field and Microstructural Observations

We present a comprehensive study of four localities on Syros that document several stages of retrograde deformation, recrystallization, and PT conditions (Fig. 4.1). The localities record a transition in deformation that has been documented in previous studies (Keiter et al. 2004; Laurent et al. 2016). Kalamisia, located in eastern Syros, shows retrogression of eclogite facies mineralogy to blueschist facies assemblages in thin section (see Appendix B.1 for sample descriptions), and is defined by a well-developed foliation (S_s, associated with D_s) that is moderately re-oriented by inclined folds that exhibit a steep axial planar cleavage and record fold hinge lines and stretching lineations (L_{t1}, defined by glaucophane, phengite, and epidote) oriented to the NE-SW (D_{t1}, Fig. 4.2A, Fig. B1) (Keiter et al. 2004). Lotos, Delfini, and Megas Gialos outcrops predominantly consist of greenschist facies minerals and exhibit transposed foliation (S_s) with tight, isoclinal folds and shallow axial planes that become further re-orientated by upright folds with fold hinge lines and stretching lineations (L_{t2}, defined by chlorite, epidote, actinolite) oriented to the E-W (D_{t2}, Fig. 4.2B; Fig. B1) (Laurent et al. 2016). Epidote boudinage is common in greenschist facies outcrops and in these outcrops is structurally associated with D_{t2} folding, as indicated by tension gashes and boudinage in epidote that occurs in an E-W orientation, parallel to the orientation of stretching lineations of greenschist facies assemblages. D_{t1} is associated with viscous deformation and alignment of epidote into foliation planes, whereas D_{t2} is associated with semi-brittle deformation and boudinage in elongate epidote. Minerals within boudin necks commonly consist of precipitation of a new generation of coarse-grained epidote, followed by brittle boudinage of epidote and precipitation of quartz, calcite, and an iron-oxide within boudin necks (Fig. B2). Boudin neck precipitates

show minimal evidence of deformation post-precipitation, as indicated by the common lack of striations on mineral surfaces.

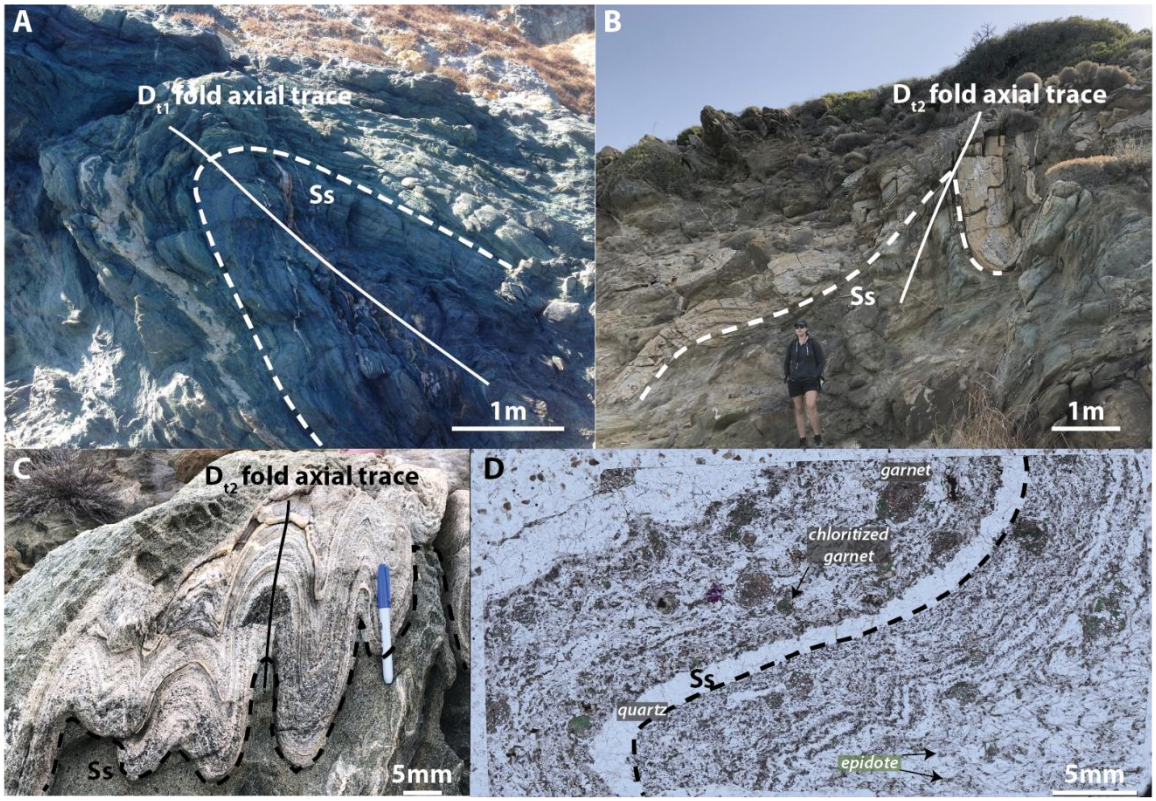

Figure 4.2. Outcrop and photomicrograph photos that elucidate our targeted stages of deformation on Syros. A: Inclined folding (D_{t1}) on Kalamisia related that refolds the S_s foliation. B: Upright folds related to D_{t2} seen at Delfini. C: Outcrop of area of sample KCS34, that samples the core of D_{t2} folds. D: Thin section plane light image of sample KCS34, that is cut perpendicular to a D_{t2} fold axial plane. Epidotes from the core of the upright fold exhibit recrystallization as indicated by a reduction in inclusions and grain size.

Our solid inclusion thermobarometry measurements are taken from ~30 µm and ~80 µm thin and thick sections; respectively, that predominantly consist of sections cut perpendicular to foliation (S_s) and parallel to stretching lineations (L_{t1} and L_{t2}). Foliation

parallel epidotes found within blueschist (Kalamisia) and greenschist facies outcrops (Lotos, Delfini, Megas Gialos) most commonly ranged in size from ~0.5 – 5 mm (b-axis length), are associated with viscous deformation, and are strongly poikiloblastic. One section from Delfini samples the core of an upright fold (D_{t2}), and the section used for analyses is cut perpendicular to a fold axial plane (Fig. 4.2C, D). The sample exhibits significant recrystallization at greenschist facies conditions and is composed of fine-grained epidote whose size along the elongate b-axis ranges from ~50 – 300 μm (Fig. 4.2D). These epidotes are roughly oriented parallel to the folded primary foliation, but often have random orientations within foliation. Epidotes in this section are not poikiloblastic and rarely preserve quartz inclusions, therefore only a few analyses were possible.

4.4 THERMOBAROMETRY CONSTRAINTS

We determined PT conditions by using solid inclusion barometry and oxygen isotope thermometry. Raman spectroscopy was used to determine frequency shifts of quartz inclusions entrapped within epidote or garnet, and a laser fluorination line and a GasBench II coupled to a gas source mass spectrometer were used to measure oxygen isotope ratios of quartz and calcite separates, respectively (see Appendix B2 for analytical methods). We categorize our pressures determined by solid inclusion barometry into three separate groups that sum qtz-in-grt and qtz-in-ep pressure estimates from different localities, samples, and host grains. Individual samples, quartz inclusions, and host grains that were used in analyses are documented in Table B1; some samples record two or more pressures groups. Group 1, deduced from qtz-in-grt barometry, indicates an entrapment pressure (P_{ent}) of ~1.4 - 1.5 GPa (n = 16), at an estimated entrapment temperature (T_{ent}) of

500 °C, in agreement with previous PT constraints of high-P conditions on Syros, Greece (Fig. 4.3, Table B1). The T_{ent} for the qtz-in-grt P_{ent} group was derived from previous estimates of maximum T reached by the CBU on Syros (Ridley 1984; Schumacher et al. 2008). Group 2 and 3 pressures deduced from qtz-in-ep barometry indicate two P_{ent} populations of ~1.3 – 1.4 (n = 31) and ~1.0 GPa (n = 6), at estimated T_{ent} of 450 °C and 400 °C, respectively (Table B1). T_{ent} for the low-P P_{ent} epidote population was deduced from quartz-calcite oxygen isotope thermometry of boudin-neck precipitates by using the calibration of Sharp and Kirschner (1994). The average of oxygen isotope temperature estimates from four quartz-calcite pairs indicates T conditions of ~400 °C (average = 405 °C, 1 σ of average = 22 °C, n = 4) during mineral precipitation (Table B2). T_{ent} for the higher-P epidote population was estimated as being intermediate between garnet and low-P epidote growth. As shown by qtz-in-ep isomekes, the assumed T_{ent} has minimal effect on calculated P_{ent}.

4.5 Results and Discussion

4.5.1 Solid mineral barometry pressure populations

Our thermobarometry results indicate that solid inclusion barometry when used in conjunction with oxygen isotope thermometry, textural, and deformational constraints, can elucidate the PT evolution of individual mineral growth from rocks and outcrops. We suggest that our grouping of pressure estimates is consistent with a systematic PT evolution that reflects subduction and exhumation. Group 1 P_{ent} estimates from the qtz-in-grt barometer are consistent with high-P conditions on Syros and are associated with prograde garnet growth. The Group 2 and 3 P_{ent} estimates from the qtz-in-ep barometer are consistent with epidote growth during retrograde D_{t1} and D_{t2} folding deformation, respectively.

Several supporting results indicate that our qtz-in-grt and qtz-in-ep pressure populations are consistent with these constraints. The group 1 garnet population commonly contains a foliation (S_r) that is defined by inclusions within garnet that is oblique to the S_s fabric, indicating a previous stage of deformation (D_r). Group 2 pressures are recorded by epidotes that predominantly preserve amphibole inclusions with glaucophane (Kalamisia), or glaucophane (rare) and high-pressure green amphibole compositions (Lotos, Delfini, Megas Gialos) (Fig. B2). Amphibole compositions within the matrix of greenschist facies outcrops transition from winchite cores to actinolite rims, suggesting that foliation parallel epidotes primarily crystallized during blueschist-to-greenschist facies metamorphism that preceded greenschist facies metamorphic conditions during actinolite crystallization. The compositional evolution of amphiboles from inclusions in epidote to matrix amphibole rims record a progressive Na decrease, indicative of decreasing PT conditions during exhumation (Fig. B2).

Group 3 pressure populations are primarily derived from a sample that records significant mineral recrystallization during D_{t2} folding (sample KCS34, Delfini), and newly precipitated epidote from a strongly retrogressed zone (SY1402, Lotos). Sample KCS34, which is sampled from the core of an upright fold that fully reprecipitates a predominant portion of the rock matrix to greenschist facies mineral contains epidotes that are small in length, contain minimal quartz inclusions, and only record Group 3 pressures, irrelative of the position of quartz inclusions within epidotes. We suggest that our low-P group (group 3) is associated with epidote growth during D_{t2} folding, that is predominantly recorded in areas that undergo the most significant recrystallization due to enhanced deformation and/or fluid influx during this stage of deformation (e.g., core of fold).

4.5.2 Comparing pressure-temperature conditions with previous studies

We compare the PT conditions determined here with previous work (Fig. 4.3A, 4.3B). Two studies have determined comprehensive PT paths for Syros during exhumation and present different peak and exhumation PT conditions (Fig. 4.3B, Trotet et al., 2001; Schumacher et al., 2008). Schumacher et al. (2008) suggest a "cold" PT path during exhumation, with continuous exhumation of CBU packages shortly after juxtaposition near peak metamorphic conditions; however, their decompression path is based on lawsonite + zoisite stability and has large P and T ranges. Trotet et al. (2001b) suggest that CBU eclogites, blueschists and greenschists of Syros undergo individual cooling histories during exhumation and are juxtaposed late along ductile shear zones. Our results from our 4 locations across Southern Syros show that these outcrops reach similar PT conditions during peak metamorphism and undergo similar cooling histories during retrograde blueschist facies metamorphism as deduced from blueschists and cryptic blueschist-to-greenschist facies assemblages within "greenschist facies" rocks (Fig. 4.3A). Our calculations suggest peak metamorphic conditions of the CBU on Syros of around ~1.5 GPa and 500 °C, as shown by qtz-in-grt P_{ent} estimates, indicating a subduction zone gradient of ~10°C km^{-1} at 50 km (assuming 30 MPa km^{-1}). Group 2 and 3 qtz-in-epidote P_{ent} estimates (Group 2: ~1.3 GPa, ~450 °C; Group 3: ~1.0 GPa, ~400 °C) indicate geothermal gradients of ~10 °C km^{-1} and ~ 12 °C km^{-1} at ~43 and 33 km depths, respectively (Fig. 4.3B). Our results show that CBU rocks from Southern Syros followed a similar PT trajectory during exhumation, suggesting that they were exhumed as coherent packages that were juxtaposed near peak metamorphic conditions, but have experienced different extents of deformation and thus recrystallization during exhumation, inconsistent with results that suggest an individual PT evolution for rocks from each metamorphic facies

(Trotet et al. 2001b, 2001a). Our results are in better agreement with a PT evolution resembling that determined by Schumacher et al. (2008), and a geothermal gradient of ~10 – 12 °C km $^{-1}$ that has also been proposed for CBU rocks from Sifnos, Greece (Schmädicke and Will 2003).

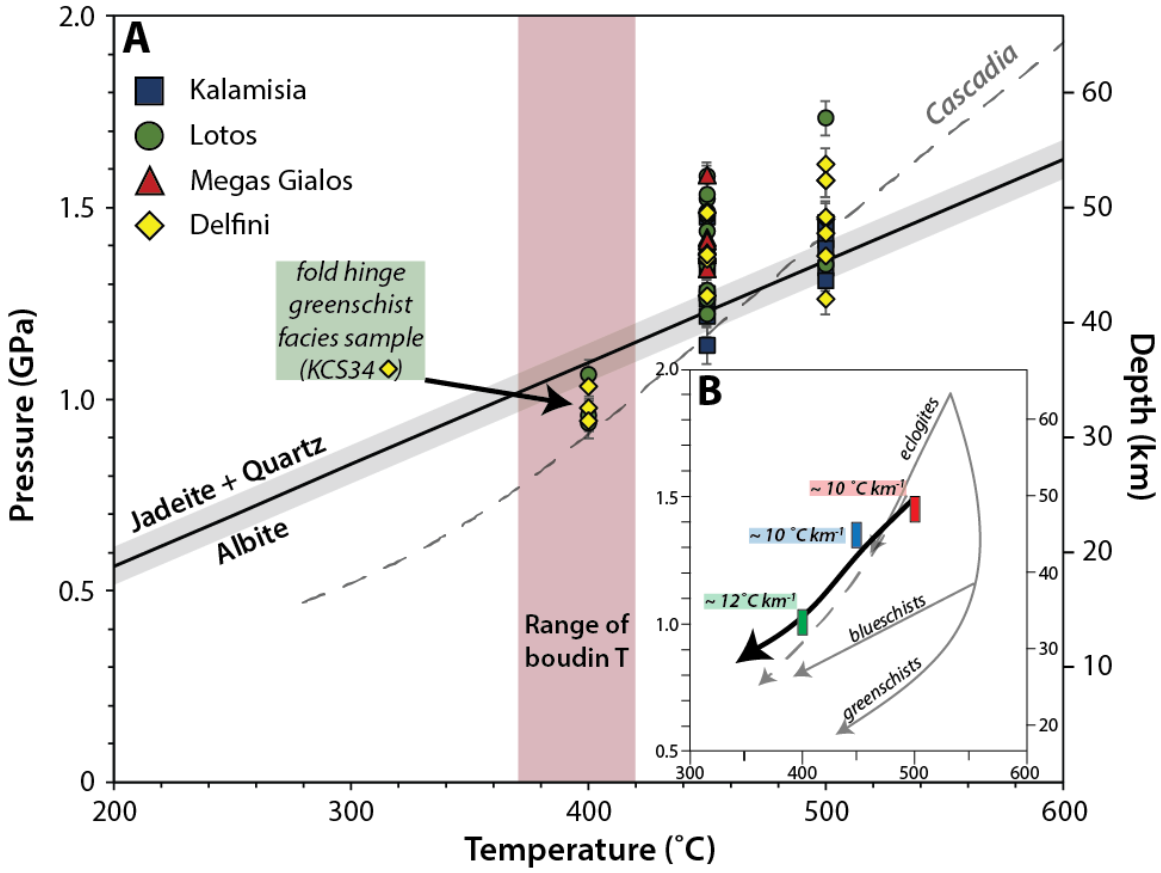

Figure 4.3. A: Pressure-temperature conditions deduced from solid inclusion barometry and stable isotope thermometry. P_{ent} groups 1, 2, and 3, are modelled at 500 °C, 450 °C, and 400 °C. Data is superimposed on the Central Cascadia modeled geothermal gradient from Syracuse et al. (2010). B: Calculated geothermal gradients during exhumation from pressure-temperature conditions determined in this study. Black line reflects a schematic pressure-temperature evolution exhibited by CBU rocks during exhumation. Grey dashed and solid lines represent reference pressure-temperature paths of Schumacher et al. (2008) and Trotet et al. (2001b), respectively.

4.5.3 Exhumation implications from determined PT conditions

Our results indicate that the CBU formed under a warm subduction zone gradient of ~10 °C km^{-1} during peak metamorphic conditions, and its subsequent PT evolution followed contemporaneous cooling during decompression that required a heat sink at depth to cool exhuming rocks. The cooling of exhuming rocks could be achieved under a steady-state subduction zone thermal gradient with modeled thermal conditions of slab-top temperatures similar to those of warm subduction zones, such as Cascadia (Fig. 4.3A) (e.g., Syracuse et al., 2010; Walowski et al., 2015). These constraints would suggest that exhumation of the CBU was achieved parallel to the subducting African plate, in a subduction channel geometry, prior to core-complex capture. During this phase of exhumation rocks exhibit a progressive change in kinematics, from N-S stretching lineations during subduction, to lineations that swing towards NE-SW and finally E-W during exhumation.

4.6 Future Applications and Conclusions

This work suggests that CBU rocks from Syros, Greece, experienced similar peak and exhumation-related PT conditions that indicate incipient cooling during decompression, consistent with exhumation of cohesive units within a subduction channel. In addition, this work further highlights the potential of using solid inclusion thermobarometry in combination with structural (macro and micro) and petrographic constraints, to constrain PT conditions of challenging rock assemblages.

Chapter 5: A comparison of the pressure-temperature and fluid evolution of Syros and Tinos, Greece: implications for exhumation of high-pressure metamorphic rocks

ABSTRACT

This work compares the kinematic, fluid history, and pressure-temperature (PT) evolution of retrograde greenschist facies rocks from the Cycladic Blueschist Unit (CBU) on the islands of Syros and Tinos, Greece, with a focus on constraining the fluid history of Syros during the early exhumation history of the CBU. Both islands preserve relict high-pressure blueschist-to-eclogite facies metamorphic assemblages and greenschist facies retrograde metamorphic rocks that differ in kinematic style, fluid history, and PT conditions. CBU greenschist facies rocks from Syros, Greece, record coaxial strain and E-W stretching lineations. The fluid history as deduced from $\delta^{18}O$, δD, and $\delta^{13}C$ values of boudin neck quartz and calcite mineral separates that form during E-W stretching and record ~ 1.0 GPa and ~400 °C greenschist facies metamorphic conditions, indicate possible interaction with slab-derived fluids derived from dehydration of altered oceanic basalts and/or sediments, and a low $\delta^{13}C$ carbon source that could be derived from mixing of carbon sources such as decarbonation of marbles and oxidation of graphite schists, or internal matrix calcite. Quartz-calcite pairs from boudin necks that record higher temperatures that range from 452 – 544 °C, indicate similar $\delta^{18}O$ values of fluids as those present during greenschist facies metamorphism, implying similar fluid sources. Carbon isotope values of these higher temperature boudins; however, may indicate carbon sourced from a reservoir with higher $\delta^{13}C$ values that could be consistent with decarbonation of marbles or dissolution and reprecipitation of foliation matrix calcite. Previous work on greenschist facies rocks from Tinos, Greece observe enhanced mylonitization and non-

coaxial strain with top-to-the NE stretching lineations. Quartz-in-epidote barometry indicates epidote growth between ~ 0.6 - 0.8 GPa at estimated temperatures between ~ 300 – 450 °C. The fluid history of samples from below the Tinos detachment indicate possible late-stage interaction with meteoric water transferred along the Tinos detachment into the CBU footwall. The results present contrasting kinematics, PT conditions, and fluid history of greenschist facies metamorphism on both islands, and indicate a progression of exhumation mechanisms, that are consistent with initial exhumation of the CBU in a subduction channel geometry, followed by late-stage exhumation of the CBU in the footwall of core-complex detachments. Retrograde metamorphism on Syros that is documented in this work would therefore have occurred under a cold geothermal gradient in a forearc setting, prior to core-complex related extension.

5.1 INTRODUCTION

The mechanisms that lead to exhumation of high-pressure, low-temperature (HP-LT) metamorphic rocks have remained perplexing since the recognition of the petrologic significance of blueschist facies mineral assemblages (Ernst 1971). Relict HP-LT rocks at the surface of the Earth reflect important processes that occur in subduction zones, yet much debate exists as to the driving forces and kinematics behind the exhumation processes. Models that have been proposed to explain the exhumation of blueschists, eclogites, and ultrahigh-pressure (UHP) rocks include, but are not limited to: forced return flow in a subduction channel (i.e., corner flow) (Cloos 1982; Cloos and Shreve 1988a, 1988b), fault-driven capture of high-grade blocks via low-angle detachment faulting (e.g., Avigad and Garfunkel 1991; Hacker et al. 1995), buoyancy driven uplift (e.g., serpentinite diapirism) (e.g., Ernst et al. 1997), and orogenic wedge extrusion mechanics (e.g., Platt

1986; Ring and Reischmann 2002). Though the transport of HP-LT rocks to the surface remains a puzzling process of subduction zones, the forces that act to exhume these rocks greatly influences the evolution of continental margins.

This work focuses on better constraining the exhumation history of the Cycladic Blueschist Unit (CBU) on Syros and Tinos, Greece, with an emphasis on constraining fluid sources during retrograde metamorphism on Syros, Greece. Exhumation has been attributed to two events: an Eo-Oligocene event that was accommodated by syn-orogenic exhumation (Ring et al. 2007), followed by Miocene bivergent extension accommodated by two large-scale detachment fault systems (Jolivet et al. 2010; Grasemann et al. 2012). On the islands of Syros and Tinos, the influence of Miocene detachment faulting is well established; however, the mode of early exhumation remains enigmatic. Syros and Tinos retrograde assemblages potentially record how subduction-related fluid sources vary at shallow depths (< 50 km) during dehydration of subducting continental lithosphere, and during the influence of low-angle normal faults.

5.2 GEOLOGIC HISTORY

5.2.1 Regional Geology

The Cycladic archipelago of Greece preserves a metamorphic complex that consists of a series of progressively juxtaposed terranes. Units of the Attic-Cycladic complex on Syros and Tinos, Greece, consist of, in stratigraphic order from top to bottom: the Vari Unit, the Upper Unit, and the Cycladic Blueschist Unit (CBU) (Keiter et al. 2011; Soukis and Stockli 2013). The CBU is composed of intercalated marble-schist sequences, metavolcanics, metabasalts, and metagabbros with variable amounts of retrogression that is most prominent adjacent to large-scale detachments (Mehl et al. 2005; Brichau et al.

2007; Jolivet et al. 2010). CBU rocks are interpreted as a collection of passive margin deposits of the Adria (Apulian) continental block that were subsequently subducted beneath the Pelagonian continental unit and Eurasian plate, and reached blueschist-to-eclogite PT conditions (Jolivet et al. 2003; Philippon et al. 2011; Fu et al. 2014). The Upper Unit contains allochthonous klippe of Late Cretaceous granitoids, Permo-Mesozoic sediments, ophiolite fragments, and greenschist-facies to medium-pressure/low-temperature metamorphic rocks (Keiter et al. 2011; Soukis and Stockli 2013). The allochthonous Vari Unit is composed of granitoids and quartzofeldspathic gneiss that reached amphibole–epidote facies conditions between 100 – 95 Ma based on Rb-Sr and $^{40}Ar/^{39}Ar$ ages (Tomaschek et al. 2000).

This work focuses on rocks of the CBU from Syros and Tinos, Greece (Fig. 5.1). Three distinct metamorphic events have been proposed to be recorded by the CBU. The first metamorphic event (M1) is an Eocene high-P/T event, where peak metamorphic conditions were reached at ~53 Ma on Syros [Lu-Hf garnet dating (n = 3), U-Pb dating of zircon rims (Tomaschek et al. 2003; Lagos et al. 2007)] and ~44 Ma on Tinos [mica Ar-Ar dating (Bröcker et al. 1993)]. The second metamorphic event (M2) was a regional event that occurred around 25-18 Ma that caused retrograde greenschist facies metamorphism (Wijbrans and McDougall 1986; Wijbrans et al. 1990; Brocker and Franz 2006). The third metamorphic event (M3) is associated with contact metamorphism adjacent to Miocene granitoid intrusions on Sifnos, Tinos, Mykonos, and Naxos (Grasemann et al. 2012).

During the (M1) Eocene event, general agreement suggests that the CBU on Syros and Tinos reached peak P-T conditions of ~15 kbar and ~500 °C (Bröcker et al. 1993; Schumacher et al. 2008), and developed blueschists and eclogites preserved on the islands of Sifnos, Syros, and Tinos. A study from Syros and Sifnos suggests that peak P-T

conditions were much higher, around ~2.0 GPa and 550 °C (Trotet et al., 2001); however, more recent studies based on mineral-equilibria of marbles (Schumacher et al. 2008) and quartz-in-garnet barometry from Kini beach (metabasite; Behr et al. 2018) support the more moderate P-T estimates of ~1.5 GPa and 500 °C.

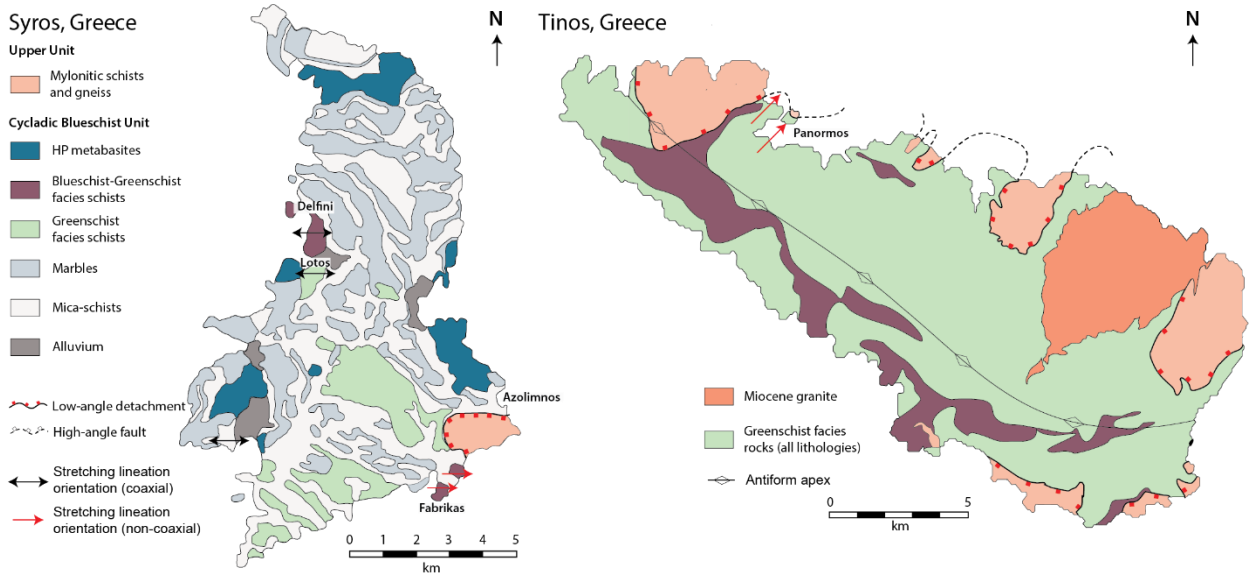

Figure 5.1: Geologic Maps of Syros and Tinos, Greece. The outcrop where samples were collected are shown in bold text. Syros records coaxial strain (black double arrows), except below the Vari detachment (red single arrow). Tinos records non-coaxial strain below the Tinos detachment.

Regional greenschist facies metamorphism marks the beginning of the M2 event. Previous work on Tinos constrains greenschist facies metamorphism to have occurred around ~0.4 – 0.7 GPa and ~440 – 470 °C, based on quartz-magnetite oxygen isotope thermometry and petrologic constraints of blueschist-to-greenschist transitions (Matthews and Schliestedt 1984; Holland 1988; Bröcker et al. 1993). Studies generally agree that greenschist facies metamorphism occurred in the Oligo-Miocene during back-arc

extension in the Hellenic subduction zone (Matthews and Schliestedt 1984; Schliestedt and Matthews 1987). No studies on Syros have carefully documented the sources of the fluids that may have caused greenschist facies metamorphism, leaving uncertainty about the fluids present during this stage of P-T conditions.

5.2.2 Previous Syros and Tinos Kinematic Observations

Previous work on Syros has documented two stages (D1 and D2) of deformation: 1) dynamic, ductile isoclinal folding during prograde metamorphism, and 2) late-stage upright kink folding and crenulation during greenschist facies metamorphism that primarily occurs under static conditions (Keiter et al. 2004). The S2 foliation of Keiter et al. (2004) is the penetrative S2 fabric that defines the dominant foliation across Syros, that is subsequently overgrown by euhedral, static lawsonite pseudomorphs. The presence of well-preserved lawsonite pseudomorphs, has been proposed as evidence of static greenschist facies metamorphism during exhumation-related upright kink folding (Keiter et al. 2004, 2011). Contrary works suggests that the dominant S2 foliation on Syros formed during exhumation and is temporally accompanied by NW-SE trending lineations, symmetric pressure shadows, and island-wide boudinage (Rosenbaum et al. 2002). The presence of symmetric structures is proposed as evidence of deep coaxial, ductile vertical thinning (Rosenbaum et al. 2002). More recent work has suggested that southern Syros records non-coaxial strain and top-to-the-E/NE stretching lineations that occur as deformation progressively localizes at the base of a subduction channel (Laurent et al. 2016).

More agreement exists on the evolution of the structural history of Tinos, Greece. Multi-stage extensional faulting indicates progressive slip accommodation by the ductile-

to-brittle Tinos detachment, the semi-ductile to brittle Livadi detachment, and lastly the Vari detachment (Brichau et al. 2007). The oldest detachment (Tinos detachment) exhibits a temporal continuum of deformation from ductile shear zones that become cataclastic during exhumation and is lastly cross cut by late-stage brittle veining (Mehl et al. 2005). Importantly, all stages of deformation on Tinos that are associated with detachment faulting evolve under non-coaxial conditions and show prominent NE-SW stretching lineations that are related to the direction of slip along detachments (Parra et al. 2002; Famin et al. 2004; Mehl et al. 2005; Brichau et al. 2007).

5.2.3 Previous Studies of the Fluid History on Syros and Tinos

Previous stable isotope work on Syros has primarily focused on characterizing the oxygen isotope composition of metamorphosed altered oceanic crust and gabbros (Putlitz et al. 2000), determining mobile element transfer between mafic-felsic blocks and ultramafic matrix and the source and processes that expel high $\delta^{11}B$ fluids (e.g., Marschall 2006; Miller et al. 2009), and determining the extent of CO_2 release from marble dissolution adjacent to veins (Ague and Nicolescu 2014). Oxygen isotope studies find that metabasalts and metagabbros from Sifnos and Syros preserve $\delta^{18}O$ values that resemble altered oceanic crust, and this has been suggested to be evidence of minimal fluid release from these blocks during subduction and exhumation (Putlitz et al. 2000). High $\delta^{11}B$ boron-rich fluids that precipitate tourmaline selvages are suggested to record interaction with slab material to produce exceptionally high $\delta^{11}B$ values during exhumation-related blackwall formation around 20 – 25 km and 400 – 430 °C (Marschall 2006). Vein-marble reaction zones record complex dissolution of $CaCO_3$ and precipitation of silicate assemblages (e.g., glaucophane, epidote) (Ague and Nicolescu 2014). Transects across marbles show that

adjacent to veins, marbles exhibit complete resetting of $\delta^{18}O$ values by external fluids and show a progressive decrease in $\delta^{13}C$ values approaching veins, suggesting extremely high fluid-rock ratios during vein formation.

Previous work on Tinos, Greece has focused on constraining the relationship between blueschists and greenschists, and the evolution of fluids during detachment faulting. An oxygen isotope study from blueschist and greenschist interlayering on Tinos has shown that fluids responsible for retrograde metamorphism have a $\delta^{18}O$ value higher than magmatic fluids, suggesting that retrograde metamorphism is not due to plutonic intrusions on Tinos. Blueschist-to-greenschist facies transformation has been attributed to selective infiltration of metamorphic fluids and variable degrees of fluid-rock interaction, but with oxygen isotope variation between blueschists and greenschists that is attributed to original isotopic heterogeneity of protoliths (Bröcker et al. 1993; Ganor et al. 1996). On Sifnos, similar blueschist and greenschist facies relationships have been observed, but these studies suggest that the increase in $\delta^{18}O$ values in retrograde greenschists relative to blueschists indicate infiltration of exotic fluids (Matthews and Schliestedt 1984; Schliestedt and Matthews 1987). Further work on Tinos has deduced different conclusions from an oxygen and hydrogen isotope study of metagabbros that record high $\delta^{18}O$ and δD values relative to hydrothermal alteration of oceanic. An increase in $\delta^{18}O$ and δD values has been attributed to dehydration of altered oceanic crust, and interaction with metagabbros. A detailed study of quartz-calcite pairs in veins below the Tinos detachment shows a progressive decrease in temperatures from early veins that become transposed by progressive deformation to late-stage veins (Famin et al. 2004). Quartz and calcite oxygen isotope pairs exhibit a decrease in temperatures during the temporal evolution of veining in proximity to the Tinos detachment, and a decrease in $\delta^{18}O$ values. Results suggest that

advective removal of heat by surficial fluids leads to cooling of the CBU hanging wall and a change in fluid composition in proximity to the Tinos detachment (Famin et al. 2004).

5.3 Sample Localities and Descriptions

5.3.1 Syros, Greece

Chapter 4 highlights some of the structural features that occur during exhumation that are recorded on Syros, Greece. Briefly, samples from Syros exhibit a progressive transition of kinematics as indicated by stretching lineations that become re-oriented to the NE-SW during exhumation, and lastly to the E-W during subsequent greenschist facies metamorphism (Fig. 5.1). We have separated these deformation stages that record progressive deformation during exhumation into D_{t1} and D_{t2}. D_{t1} is primarily recorded by blueschists facies lithologies and corresponds to folds with NE-SW hinge lines that reorient a previous foliation (S_s). D_{t2} represents a continuation of deformation that progresses from blueschist-to-greenschist facies, wherein fold hinge lines become reoriented to the E-W. Common epidote boudinage appears to be associated with extension parallel to E-W stretching. Further evidence from outcrop (Fig. 5.2) indicates that Syros greenschist facies lithologies on Lotos and Delfini record coaxial strain as indicated by common boudinage and the lack of shear sense, with non-coaxial strain only becoming evident in closer proximity to the Vari detachment. This is inconsistent with recent work by Laurent et al. (2016), where they observe top-to-the-east shear sense indicators in greenschist facies lithologies on Delfini and Lotos.

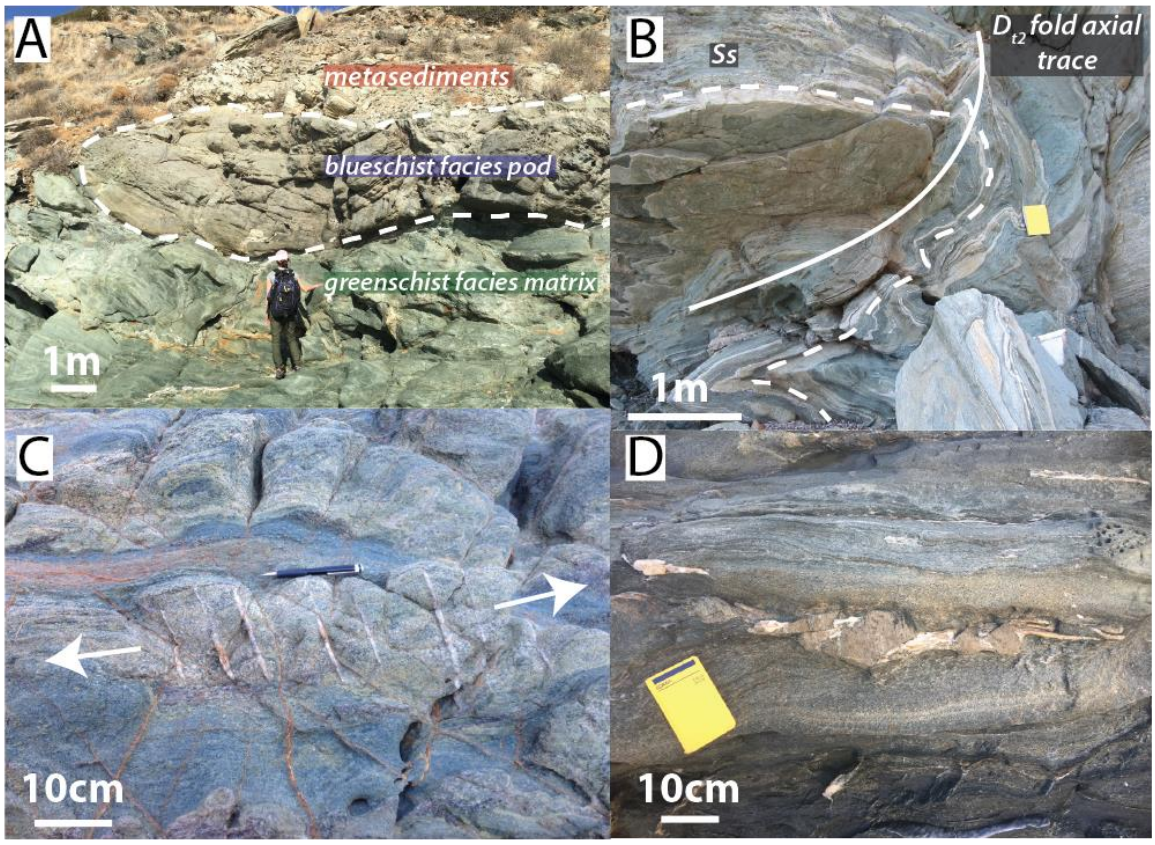

Figure 5.2: Outcrop examples of greenschist facies metamorphism on Syros, Greece. A) Blueschist-greenschist assemblages appear in close proximity, where zones that localize strain become retrogressed under greenschist facies conditions, and blueschist pods are preserved with the retrogressed matrix. B) Outcrop scale deformation associated with greenschist facies metamorphism. D_{t2}-related folds record E-W oriented hinge lines, and C) stretching parallel to this direction of extension. D) Boudinaged epidote infilled with quartz and calcite does not preserve a preferred shear orientation, suggesting coaxial strain during greenschist facies metamorphism on Syros.

5.3.1.1 Boudin Necks – Syros, Greece

Boudin neck samples were collected across Lotos, Delfini, and Fabrika on Syros, Greece (Fig. 5.3). Nine samples are derived from boudin necks minerals that precipitate between boudinaged minerals, and six samples have quartz-calcite pairs that were used for

oxygen isotope thermometry. Four boudin necks samples that were used for thermometry are surrounded by a greenschist facies matrix (Lotos and Delfini), and two samples are surrounded by a blueschist facies matrix (Fabrika).

.

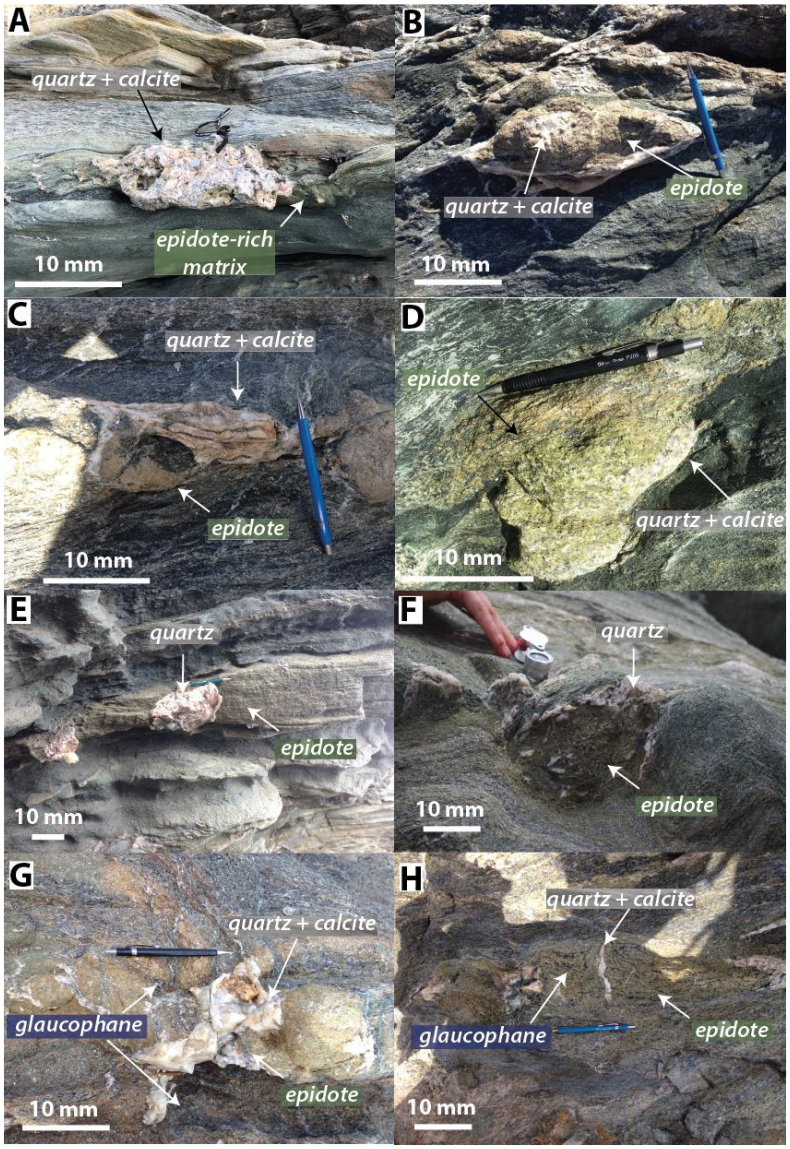

Figure 5.3: Examples of epidote boudins and boudin-neck samples. A) SY1613 (Lotos), B) SY1617 (Delfini), C) SY1618 (Delfini), D) SY1623 (Delfini), E) SY1644 (Delfini), F) SY1411 (Lotos), G) SY1632 (Fabrika), H) SY1635 (Fabrika). Boudin necks in images 3A – 3D had quartz-calcite pairs that could be used to for oxygen isotope thermometry. Boudin necks from images 3A – 3F appear to have formed during greenschist facies conditions, as indicated by the common greenschist facies assemblages that surround epidote boudins. Boudin necks from images 3G and 3H also had quartz-calcite pairs that were used for oxygen isotope thermometry. Temperatures from these samples were higher than those formed within greenschist facies matrix. Higher temperature conditions are supported by the common presence of glaucophane surrounding epidote boudins, and precipitation of intergrown coarse grained glaucophane and epidote.

5.3.1.2 Lotos – Syros, Greece

Rocks from Lotos record mineralogy (chl + ep + act + white mica ± grt) that would be expected from metabasite compositions. Felsic and mafic layering on Lotos, may also indicate the outcrop records some protoliths that are similar in composition to banded tuffs of Azolimnos, or intermingling of sediments with more mafic lithologies. Samples from Lotos that do not include boudin neck samples, are taken from fold-hinges, boudin neck reaction rims, a vein, an older generation, transposed vein, and from matrix within primary foliation (Ss) (Fig. 5.4). Samples that were taken from the foliation matrix for stable isotopes analyses are from rocks that resemble retrogressed metabasites.

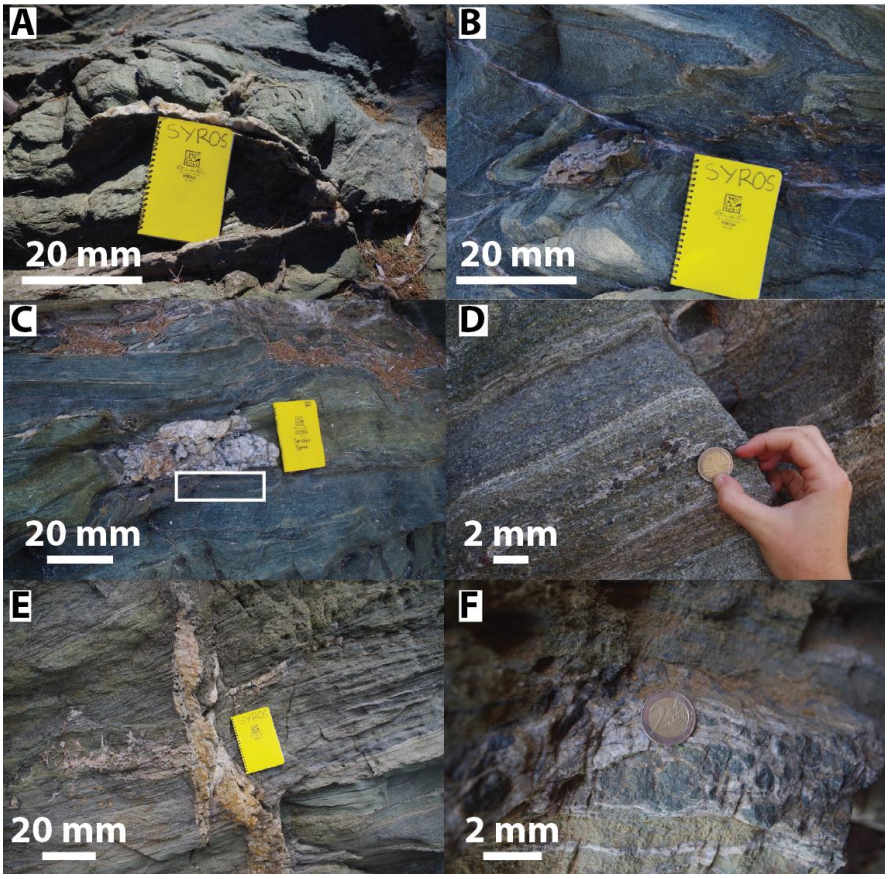

Figure 5.4: Samples collected for stable isotope analyses from Lotos on Syros, Greece. A) SY1401: fold-hinge that may be related to folding that predates D_{t2} deformation. B) SY104: fold-hinge quartz precipitation. C) SY1402: Epidote boudin with quartz-calcite precipitation in boudin neck. A sample of the greenschist facies matrix was taken from the area noted by the white box. D) SY1405: foliation matrix sampled. E) SY1408: Veining oriented N-S, perpendicular to E-W stretching lineations. The vein orientation suggests that it likely formed during D_{t2} deformation. F) SY1410: Early, transposed quartz veins that are now parallel to the primary foliation (Ss).

5.3.1.3 Azolimnos – Syros, Greece

Rocks from Azolimnos have previously been described as banded tuffitic schists (Keiter et al. 2011). Samples from Azolimnos, Greece were collected to determine the

range of $\delta^{18}O$ and δD values of igneous volcanic rocks from the CBU, to determine if they could be potential fluid sources during retrograde metamorphism (Fig. 5.5).

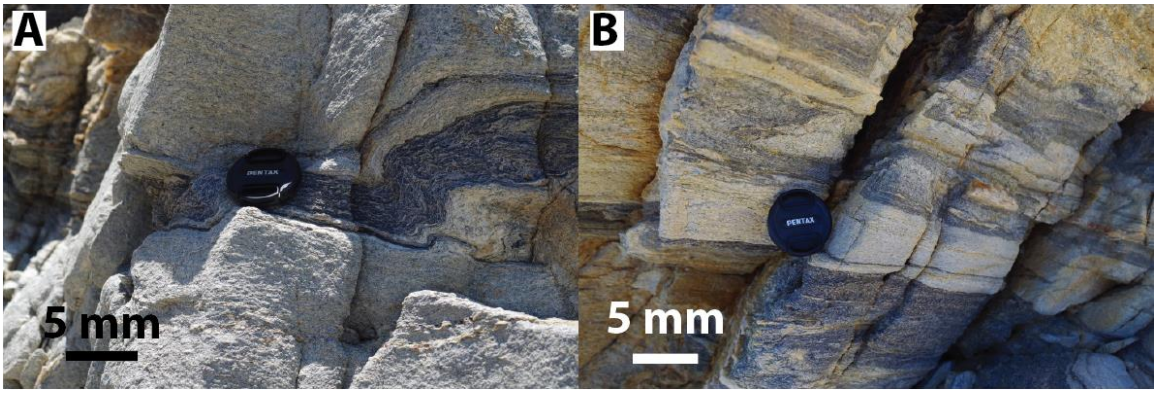

Figure 5.5: Samples collected for stable isotope analyses from Azolimnos on Syros, Greece. These samples are representative of the four samples analyzed for stable isotopes. A) SY1504 and B) SY1507 exhibit felsic and mafic layering associated with formation of banded tuffs.

5.3.1.4 Fabrikas – Syros, Greece

Samples that were collected from Fabrika span a range of lithologies, including a greenschist facies matrix adjacent to a late-stage vein (SY1456), a metasediment (SY1458), and a blueschist (SY1459) (Fig. 5.6). Two boudin neck samples were also collected for quartz-calcite oxygen-isotope thermometry (SY632 and SY1635; Fig. 5.3G, H). These samples differ from boudin necks described above, as glaucophane is commonly intermingled with the matrix of epidote boudins, suggesting that these boudin necks precipitated at higher P-T conditions (Fig. 5.3G, H).

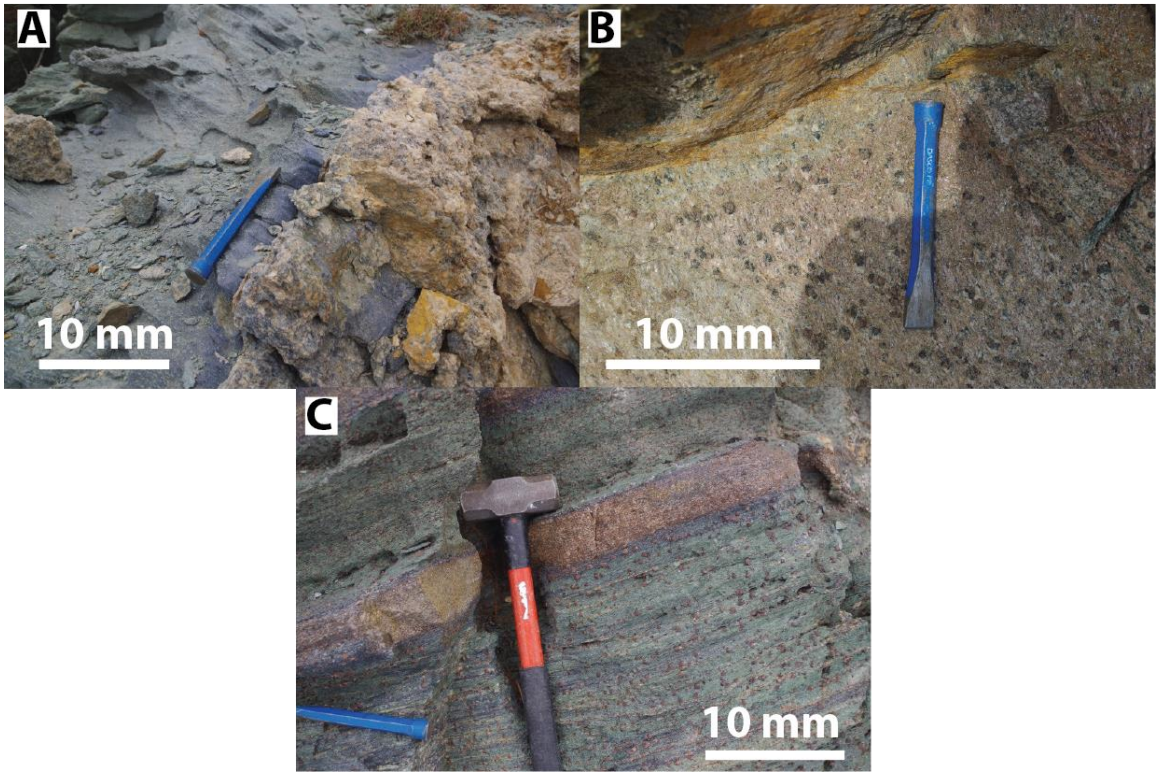

Figure 5.6: Samples collected for stable isotope analyses from Fabrika on Syros, Greece. A) SY1456: greenschist facies matrix adjacent to glaucophane that is preserved by high-CO_2 fluids during normal faulting (Kleine et al. 2014). B) SY1458: metasediment with garnets that exhibit significant chloritization. C) SY1459: blueschist facies rock interlayered with omphacite.

5.3.2 Panormos - Tinos, Greece

Samples from Tinos, Greece that were used for quartz-in-epidote barometry and stable isotope analyses are taken from the CBU footwall, ~ 200 meters away from the Tinos detachment (Fig. 5.7A, B). Samples from Tinos, Greece record increased mylonitization relative to those found on Syros.

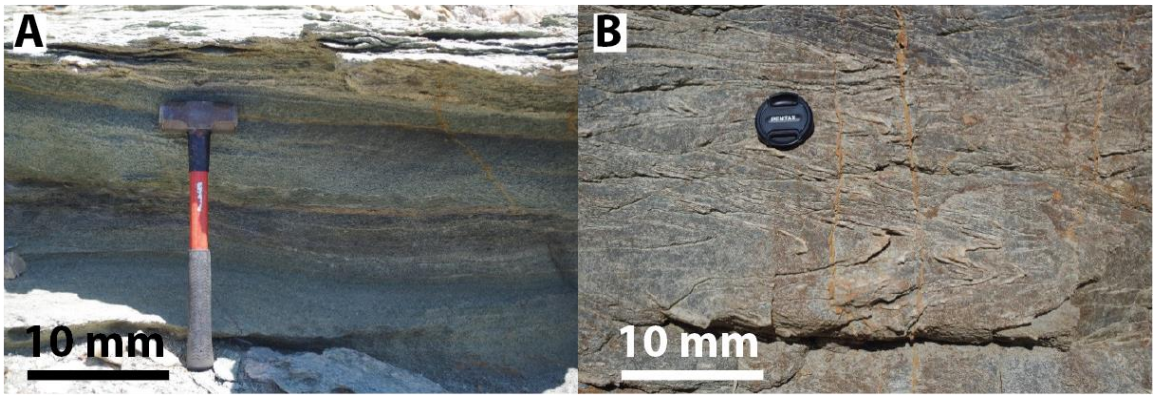

Figure 5.7: Samples collected for stable isotope and solid inclusion barometry analyses from Panormos on Tinos, Greece. A) TN1513: greenschist ~ 200 meters below the Tinos detachment. B) TN514: greenschist with tight isoclinal folds defined by quartz.

5.4 Analytical Methods

5.4.1 Quartz-in-Epidote Barometry

Raman spectroscopy measurements of quartz-in-epidote were completed at Virginia Tech on a JY Horiba LabRam HR800 Raman spectrometer. Measurements were made on foliation parallel epidotes in ~100 µm thick sections of samples KCT7 and KCT8. A 40x objective with a confocal aperture of 400 µm and a 150 µm slit width was used. Raman spectra were centered at 360 cm^{-1}. A linear drift correction dependent on the position of the 520.30 cm^{-1} Ar plasma line was applied to all measurements. The 464 cm^{-1} peak of Herkimer quartz standard was analyzed 5 times prior to analysis for instrument standardization. Quartz Raman measurements were fit by using PeakFit v4.12 from SYSTAT Software Inc. Following the approach of Schmidt and Ziemann (2000), a Gaussian amplitude model was used to fit Ar plasma lines, and the Pearson IV model was used to fit the quartz 464 cm^{-1} band. Measured quartz inclusions were small in diameter relative to the host to avoid geometric corrections, and ranged in diameter from ~ 5 – 15

μm (Mazzucchelli et al. 2018). See Chapter 3 for more information about the peak-fitting approach used for Raman measurements of quartz within epidote.

Quartz inclusion pressures (P_{incl}) were calculated from the quartz 464 cm^{-1} frequency by using the Ashley et al. (2014a) polynomial equation that refit the Schmidt and Ziemann (2000) quartz Raman shift experiments. The 128 cm^{-1} and 206 cm^{-1} quartz Raman bands were not considered in this study because of their low intensities, and common interference with shoulder epidote peaks. Entrapment pressures (P_{ent}) were calculated from residual quartz inclusion pressures by using the Guiraud and Powell (2006) 1D elastic model equation, and following the approach outlined in Chapter 2. Quartz inclusion Raman shifts were measured from multiple epidotes within individual sections. Constant epidote compositions of Xep = 0.5 and X_{cz} = 0.5 were used for all epidote modeling. The propagated errors reported in this study account for errors in peak fit statistics for the Ar plasma line and quartz 464 cm^{-1} peak of standards and unknowns, and instrument uncertainty based on the long-term standard deviation of Herkimer quartz measurements (~ ± 0.1 cm^{-1}).

5.4.2 Stable Isotope Analyses

Oxygen, hydrogen, and carbon isotope measurements were completed at the University of Texas at Austin on a ThermoElectron MAT 253 Mass Spectrometer. Oxygen isotopes of silicates were extracted on a laser fluorination line that reacts silicates samples with BrF_5 (Sharp 1990). Approximately 2 mg of sample was used for each analysis. Standards UWG-2 (garnet; $\delta^{18}O$ = + 5.8 ‰; (Valley et al. 1995) and Laussane-1 (quartz; $\delta^{18}O$ = + 18.1 ‰) were analyzed for standardization. All $\delta^{18}O$ values are reported relative to SMOW. Measurement precision based on the long-term reproducibility of standards is

± 0.1 ‰ (1 σ). CO_2 was extracted from calcite for oxygen and carbon stable isotope measurements on a Thermo Gasbench II coupled to a ThermoElectron 253 mass spectrometer. Each analysis used ~0.25 – 0.5 mg of calcite that was loaded into Exetainer vails that were flushed with ultra-high purity helium and reacted with 103 % phosphoric acid at 50 °C for ~ 2 hours. Headspace CO_2 was then transferred to the mass spectrometer. Samples were calibrated to an in-house standard, NBS-18 and NBS-19. Measurement precision is ± 0.04 ‰ (1 σ) based on the long-term reproducibility of standards. $\delta^{13}C$ values are reported in PDB.

Hydrogen isotopes of hydrous minerals were extracted by using a ThermoElectron MAT TC-EA. Approximately 2 mg of sample was loaded into silver capsules and reacted in a graphite crucible at high-temperatures following the methods of Sharp et al. (2001). A δD calibration curve was created by using IAEA-C3, IAEA-CH7, and NBS-22 standards. All δD values are reported relative to SMOW. Measurement precision based on the long-term reproducibility of standards is ± 2 ‰ (1 σ).

5.5 RESULTS

5.5.1 Quartz-in-Epidote Barometry

Chapter 4 presents an evaluation of PT estimates from four outcrops on Syros, Greece. Samples from Panormos in Tinos, Greece, allow a comparison between pressure estimates of greenschist facies metamorphism on both islands. Both samples from Panormos were collected ~ 200 meters below the Tinos detachment, in the CBU footwall. Temperature estimates for epidote crystallization have not been estimated for Tinos. The temperature range of epidote crystallization thus can only be assumed to fall in between the range of temperature estimates that have been deduced during activity of the Tinos

detachment or estimates of ambient greenschist facies metamorphism (Bröcker et al. 1993; Famin et al. 2004). Famin et al. (2004) estimated temperatures at distances greater than ~100 meters below the Tinos detachment, to vary between ~ 300 – 400 °C, providing a minimum 300 °C temperature estimate during epidote growth. Temperatures closer to the detachment during late-stage veining decrease in proximity to the detachment due to advective removal of heat by fluids. Greenschist facies metamorphic conditions on Tinos that possibly predate detachment faulting have been estimated to range between ~ 440 – 470°C based on quartz-magnetite oxygen thermometry on samples ≥ 200 meters from the Tinos detachment, deeper within the Tinos dome. Therefore, epidote growth entrapment temperatures estimates are approximated to fall between ~ 300 – 450 °C. Quartz pressures measured from inclusions near the surface of polished epidotes (~15 μm below), vary from 207 – 303 MPa (n = 5, mean = 235 MPa; Table 5.1). Entrapment pressures, calculated over the temperature range estimates determined in previous studies, exhibit minimum and maximum mean P_{ent} of ~675 MPa and ~831 MPa, respectively (at 300 and 450 °C). Quartz inclusions that were deeper below the epidote surface (~50 μm deep), retained higher residual inclusion pressures that may reflect punctuated epidote growth within the large crystals and P_{ent} at higher conditions than recorded by quartz inclusions near the surface. Uncertainty of measurements from deep quartz inclusions was higher, due to the lower intensity quartz Raman signal from these deeper inclusions.

Sample	Location	Host	Inclusion #	Host #	v464 (cm-1)	Δv464 (cm-1)	Pincl MPa	Pincl 1 σ Error (MPa)	Pent MPa*	Pent MPa‡	Pent 1 σ Error (MPa)
KCT7†	Panormos	Epidote	1	1	466.71	1.96	216	21	637	795	41
KCT7†	Panormos	Epidote	2	2	467.49	2.74	303	20	808	959	40
KCT7†	Panormos	Epidote	3	3	466.73	1.96	216	20	637	795	39
KCT7†	Panormos	Epidote	4	4	466.70	1.87	207	22	620	779	41
KCT8†	Panormos	Epidote	5	5	467.00	2.12	234	20	672	829	40
KCT7‖	Panormos	Epidote	6	6	468.13	3.31	367	23	938	1085	47
KCT7‖	Panormos	Epidote	7	6	468.81	3.99	443	23	1096	1238	48
KCT7‖	Panormos	Epidote	8	7	468.69	3.96	440	23	1089	1232	48

†Quartz inclusions near polished epidote surface, ~ 15 µm deep

‖Quartz inclusions deep below epidote surface, ~ 50 µm deep

*Assumed entrapment temperature = 300 °C

‡Assumed entrapment temperature = 450 °C

All epidote compositions modeled as X_{Ep} = 0.5, X_{Cz} = 0.5

GPS Coordinates: KCT7 - 37.662500, 25.056667, KCT8 - 37.662249, 25.056635 (Latitude, Longitude)

Table 5.1: Raman data of quartz-in-epidote measurements and calculated entrapment pressures.

5.5.2 Stable Isotopes

5.5.2.1 Greenschist Facies Boudin Necks – Syros, Greece

On Syros, Greece, we show structural and petrographic evidence that constrains the context of minerals we analyzed for oxygen and hydrogen isotope ratios. $\delta^{18}O$ values and temperatures calculated from four separate quartz-calcite boudin neck precipitates from Lotos and Delfini are given in Table 5.2. Temperatures range from 373 – 419 °C. The $\delta^{18}O$ values of fluids in oxygen isotope equilibrium temperatures with quartz and calcite pairs, range from + 12.0 to + 16.1 ‰ and + 12.8 to + 16.6 ‰ (n = 4) by using the quartz-water and calcite-water fractionation calibrations of Sharp and Kirschner (1994) and Hu and Clayton (2003), respectively (Table 5.2, Fig. 5.8A). Three additional boudin neck samples of calcite and quartz (samples that don't have a quartz or calcite pair), also suggest similar $\delta^{18}O$ values. Two calcite and one quartz sample have $\delta^{18}O$ values of + 14.5 to + 16.1 (n = 2) and +17.3 ‰ (n =1), respectively (Table 5.2, Fig. 5.8A). Assuming a temperature of 400 °C, $\delta^{18}O$ values of H_2O in equilibrium with calcite indicate a range of + 11.8 to + 13.4 ‰ (n = 2), and 12.1 ‰ (n = 1) for a fluid in equilibrium with quartz (Table

5.2, Fig. 5.8A). Carbon isotopes of calcite from boudin neck precipitates show minimal variation in $\delta^{13}C$ values and range from -0.77 to + 0.51 ‰. CO_2 in fluids in isotopic equilibrium with calcite vary from $\delta^{13}C \approx$ + 1.9 to + 3.2 ‰ (n = 6, Table 5.2, Fig. 5.9).

5.5.2.2 Lotos – Syros, Greece

Quartz values of samples from Lotos, Syros that sample fold hinges, epidote boudin neck rims, and foliation matrix, show small oxygen isotope variation, and similar $\delta^{18}O$ values to boudin neck quartz-calcite pairs, with $\delta^{18}O$ values that range from + 14.4 to + 17.4 ‰ (n = 6, Table 5.2, Fig. 5.8A). Assuming a quartz-water equilibration temperature of 400 °C, calculated from the average temperature of epidote boudin neck precipitates, $\delta^{18}O$ values of water in equilibrium with quartz range from + 9.2 to + 12.1 ‰ (n = 6, Table 5.2). The high end of these $\delta^{18}O$ water values overlaps with $\delta^{18}O$ water values calculated from boudin neck quartz-calcite pairs, and with boudin neck precipitates from Lotos (SY1613 and SY1411) that indicate fluid $\delta^{18}O$ values of + 12.0 to +12.8 ‰ (n = 3, Table 5.2).

Hydrogen isotope values from Lotos likewise show similar, minimal variation, with δD values of matrix chlorite and epidote that are aligned parallel to the foliation that range from -42 to -51 ‰ (n = 2) and -34 to -51 ‰ (n = 2), respectively (Table 5.2). The larger variation of epidote δD values may reflect the abundance of hydrous inclusions found within epidote (e.g., amphibole, white mica). The $\delta^{18}O$ values of chlorite and epidote range from + 12.9 to + 13.6 ‰ and + 11.7 to +12.4 ‰, respectively. δD values of H_2O in equilibrium with chlorite at 400 °C, indicate a δD range of -10.1 to -18.9 ‰ (Graham et al. 1981; Table 5.2, Fig. 5.8B). $\delta^{18}O$ values of fluids in equilibrium with chlorite at 400 °C calculated by using the Wenner and Taylor (1971) chlorite-water oxygen isotope

fractionation calibration, indicate $\delta^{18}O$ values between + 14.2 to + 14.8 ‰ (n = 2, Table 5.2), in close agreement with $\delta^{18}O$ values of fluids calculated from boudin necks (Fig. 5.8B).

5.5.2.3 Azolimnos – Syros, Greece

Oxygen isotope values of mineral separates of glaucophane, white mica, quartz, garnet, and chlorite from Azolimnos meta-tuffitic blueschists were measured to establish a possible range $\delta^{18}O$ values of metavolcanics rocks. Separates from Azolimnos exhibit a tight range in $\delta^{18}O$ values that vary from + 6.6 to + 10.4 ‰ (n = 13, Table 5.2, Fig. 5.8A). Hydrogen isotope compositional variation of Azolimnos hydrous silicates also exhibit a tight cluster, with δD values ranging from -65 to -45 ‰ (n = 9, Table 5.2, Fig. 5.8B). The range of $\delta^{18}O$ and δD values are in good agreement with those of primary igneous, volcanic rocks (Bindeman 2008; Sharp 2017).

5.5.2.4 Fabrikas – Syros, Greece

Samples from Fabrika were only analyzed for their hydrogen isotope compositions. Their proximity to brittle normal faults makes their relationship with regional greenschist facies metamorphism difficult to evaluate. δD values of chlorite, white mica, epidote, and glaucophane separates from Fabrika range from -44 to – 27 ‰ (Table 5.2, Fig. 5.8B). $\delta^{18}O$ values and temperatures calculated from quartz-calcite boudin neck precipitates from Fabrika range from 452 – 544 °C (Table 5.2). The $\delta^{18}O$ values of fluids in oxygen isotope equilibrium temperatures with quartz and calcite pairs (calculated at T determined from quartz-calcite oxygen isotope thermometry) exhibit a tight range of + 13.3 to + 13.3 ‰ and + 12.5 to + 14.5 ‰ (n = 2) by using the quartz-water and calcite-water fractionation calibrations of Sharp and Kirschner (1994) and Hu and Clayton (2003), respectively (Table

5.2, Fig. 5.8A). Carbon isotope compositions of calcite from boudin neck precipitates show minimal variation and range from + 0.81 to + 1.79 ‰. CO_2 in fluids in isotopic equilibrium with calcite vary from $\delta^{13}C \approx +3.5$ to + 4.6 ‰ (n = 6, Fig. 5.9).

5.5.2.5 Panormos – Tinos, Greece

Chlorite δD values measured from mineral separates of two samples from Panormos on Tinos show minimal δD variation, with values ranging from -82 to -86 ‰ (n = 2, Table 5.2, Fig 5.8B). $\delta^{18}O$ values of quartz, chlorite, and epidote range from + 11.7 to + 17.3 ‰ (n = 4, Table 5.2).

Sample	Location	GPS Coordinates Latitude, Longitude	Microstructural Context	Mineral	$\delta^{18}O$ vs. SMOW (‰)	$\delta^{13}C$ vs. PDB (‰)	δD vs. SMOW (‰)	Temperature °C	Temperature Error °C (1 σ)	Fluid $\delta^{18}O$ vs. SMOW (‰)	Fluid $\delta^{13}C$ vs. PDB (‰)	Fluid δD vs. SMOW (‰)
SY1613	Lotos	37.44480118, 24.89873159	Epidote Boudin Neck	Quartz	17.8							
SY1613 (duplicate)		-	Epidote Boudin Neck	Quartz	17.9							
SY1613	Lotos	-	Epidote Boudin Neck	Calcite	15.8	0.38		373*	29	12.0‡, 12.8•	3.0∫	
SY1617	Delfini	37.45646677, 24.89872299	Epidote Boudin Neck	Quartz	18.5							
SY1617 (duplicate)		-	Epidote Boudin Neck	Quartz	18.6							
SY1617	Delfini	-	Epidote Boudin Neck	Calcite	16.7	0.51		419*	33	13.8‡, 14.3•	3.2∫	
SY1618	Delfini	37.45645416, 24.89873137	Epidote Boudin Neck	Quartz	18.3							
SY1618	Delfini	-	Epidote Boudin Neck	Calcite	16.5	0.14		419*	32	13.6‡, 14.1•	2.8∫	
SY1623	Delfini	37.454283, 24.897447	Epidote Boudin Neck	Quartz	21.1							
SY1623 (duplicate)		-	Epidote Boudin Neck	Quartz	21.1							
SY1623	Delfini	-	Epidote Boudin Neck	Calcite	19.2	0.15		408*	31	16.1‡, 16.6•	2.6∫	
SY1632	Fabrikas	37.3884571, 24.95281502	Epidote Boudin Neck	Quartz	15.9							
SY1632	Fabrikas	-	Epidote Boudin Neck	Calcite	14.6	0.81		544*	44	13.3‡, 12.5•	3.5∫	
SY1635	Fabrikas	37.38677946, 24.95107418	Epidote Boudin Neck	Quartz	17.3							
SY1635	Fabrikas	-	Epidote Boudin Neck	Calcite	15.7	1.79		452*	34	13.3‡, 14.5•	4.6∫	
SY1621	Delfini	37.4542809, 24.89742966	Fe-Calcite Boudin Neck	Calcite	16.1	-0.77	-0.77	400†		13.4•	1.9∫	
SY1644	Delfini	37.44374132, 24.89749714	Epidote Boudin Neck	Calcite	14.5	0.51	1.79	400†		11.8•	3.2∫	
SY1411	Lotos	37.443600, 24.897240	Epidote Boudin Neck	Quartz	17.3			400†		12.1‡		
SY1401	Lotos	37.397660, 24.943500	Fold-hinge	Quartz	17.2			400†		12.0‡		
SY1404	Lotos	37.443840, 24.896960	Fold-hinge	Quartz	16.1			400†		10.9‡		
SY1402	Lotos	37.443320, 24.896870	Epidote Boudin Neck Rim	Quartz	14.4			400†		9.2‡		
SY1402	Lotos	-	Epidote Boudin Neck Rim	Chlorite	13.6		-51	400†		14.8‖		-19‖
SY1402	Lotos	-	Epidote Boudin Neck Rim	Epidote	11.7		-53					
SY1405	Lotos	37.443630, 24.897230	Greenschist Foliation Matrix	Quartz	16.4							
SY1405 (duplicate)		-	Greenschist Foliation Matrix	Quartz	16.4			400†		11.2‡		
SY1405	Lotos	-	Greenschist Foliation Matrix	Chlorite	12.9		-42	400†		14.2‖		-10‖
SY1405	Lotos	-	Greenschist Foliation Matrix	Epidote	12.4		-34	-				
SY1408	Lotos	37.443720, 24.897560	Vein	Quartz	17.4			400†		12.2‡		
SY1410	Lotos	37.443560, 24.897230	Transposed Vein	Quartz	17.3			400†		12.1‡		
SY1456	Fabrika	37.388900, 24.953130	Greenschist Foliation Matrix	Chlorite			-41					
SY1458	Fabrika	37.388950, 24.953260	Metasediment Foliation Matrix	White Mica			-33					
SY1459	Fabrika	37.389130, 24.953630	Blueschist Foliation Matrix	White Mica			-27					
SY1459	Fabrika	-	Blueschist Foliation Matrix	Epidote			-35					
SY1459	Fabrika	-	Blueschist Foliation Matrix	Glaucophane			-44					
SY1501	Azolimnos	37.413278, 24.967250	Blueschist Foliation Matrix	Glaucophane	6.6		-58					
SY1501	Azolimnos	-	Blueschist Foliation Matrix	White Mica	8.1		-46					
SY1501	Azolimnos	-	Blueschist Foliation Matrix	Garnet	6.9							
SY1503	Azolimnos		Blueschist Foliation Matrix	Glaucophane	8.0		-56					
SY1504	Azolimnos	37.413333, 24.967167	Blueschist Foliation Matrix	White Mica	8.0							
SY1504	Azolimnos	37.413222, 24.967111	Blueschist Foliation Matrix	Glaucophane	8.0		-50					
SY1504	Azolimnos	-	Blueschist Foliation Matrix	Quartz	9.3							
SY1505	Azolimnos	37.413083, 24.966778	Blueschist Foliation Matrix	White Mica	8.1		-54					
SY1505	Azolimnos	-	Blueschist Foliation Matrix	Glaucophane	7.9		-56					
SY1506	Azolimnos	37.412583, 24.965778	Blueschist Foliation Matrix	Chlorite	8.2		-65					
SY1507	Azolimnos	37.412583, 24.965778	Blueschist Foliation Matrix	Glaucophane	8.5		-55					
SY1507	Azolimnos	-	Blueschist Foliation Matrix	White Mica	8.6		-45					
SY1507	Azolimnos	-	Blueschist Foliation Matrix	Quartz	10.4							
TN1513	Panormos	37.662778, 25.058056	Greenschist Foliation matrix	Chlorite	13.3		-86					
TN1513	Panormos	-	Greenschist Foliation matrix	Quartz	17.3							
TN1514	Panormos	37.662500, 25.056667	Greenschist Foliation matrix	Chlorite	11.7		-82					
TN1514	Panormos	-	Greenschist Foliation matrix	Epidote	12.6							

* Temperature calculated by using the Sharp and Kirschner (1994) quartz-calcite oxygen isotope fractionation calibration

The average $\delta^{18}O$ value of duplicates was used to calculate temperatures

† Temperature assumed to be 400°C

‡ Fluid $\delta^{18}O$ values calculated by using the Sharp and Kirschner (1994) quartz-water oxygen isotope fractionation calibration

• Fluid $\delta^{18}O$ values calculated by using the Hu and Clayton (2003) calcite-water oxygen isotope fractionation calibration

‼ Fluid $\delta^{18}O$ values calculated by using the Wenner and Taylor (1971) chlorite-water oxygen isotope fractionation calibration

‖ Fluid δD values calculated by using the Graham et al. (1994) chlorite-water hydrogen isotope fractionation calibration

∫ Fluid $\delta^{13}C$ values calculated by using the Ohmoto (1992) CO2-calcite carbon isotope fractionation calibration

Table 5.2: $\delta^{18}O$, $\delta^{13}C$ and δD values of boudin neck precipitates and mineral separates.

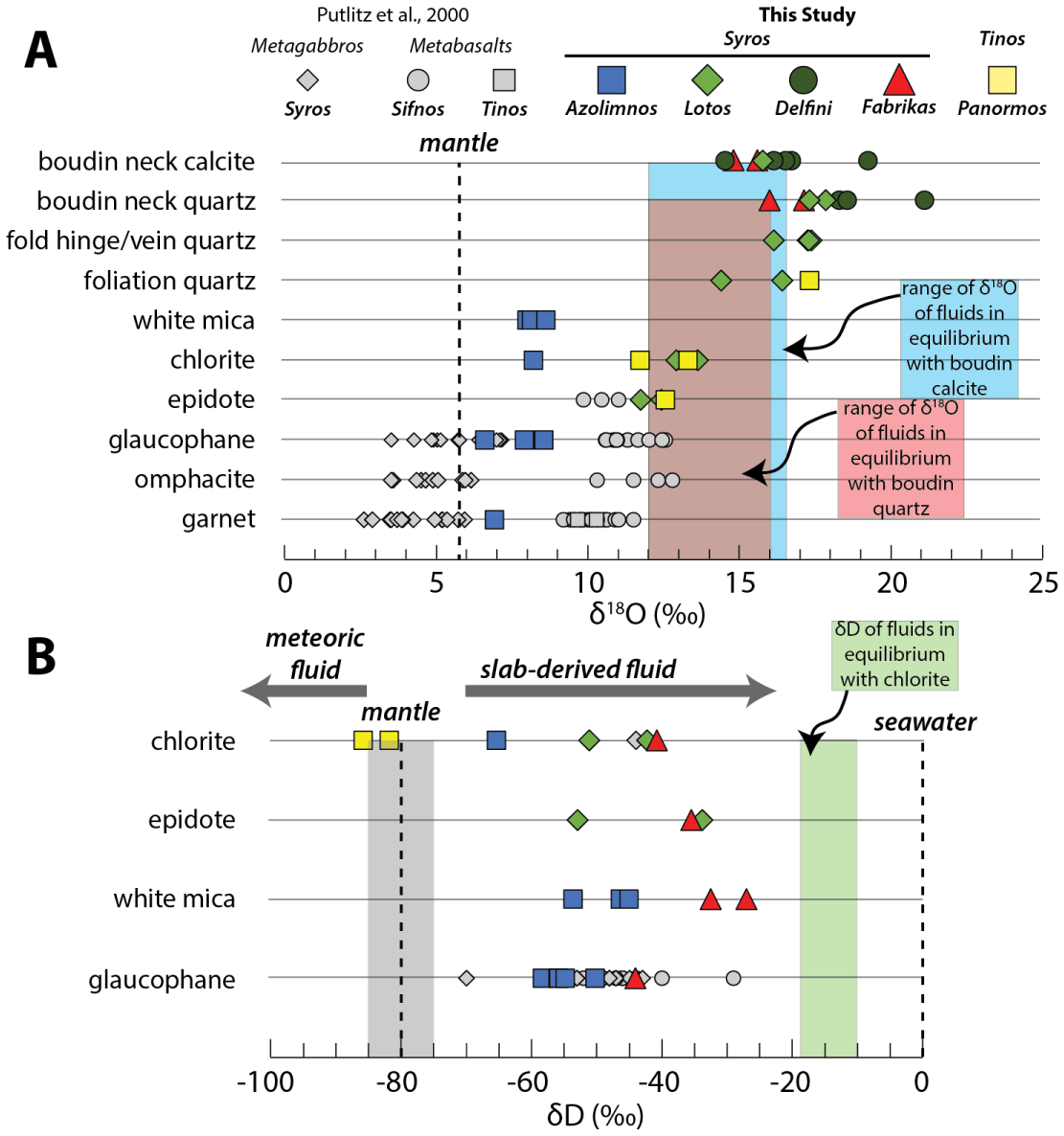

Figure 5.8: Oxygen and hydrogen isotope values of mineral separates from Syros and Tinos, Greece. A) Quartz $\delta^{18}O$ values are compared relative to reference metabasalts and metagabbros from Putlitz et al. (2000). Red and blue boxes indicate the $\delta^{18}O$ value of H_2O fluids in equilibrium with boudin neck quartz and calcite, respectively. B) Hydrogen isotopes are also compared with reference metabasalt and metagabbros. Syros chlorite associated with D_{t2} exhibits high δD fluid values, whereas chlorites from Tinos exhibit low δD fluid values. The results imply different fluid sources for both greenschist facies rocks. See text for discussion.

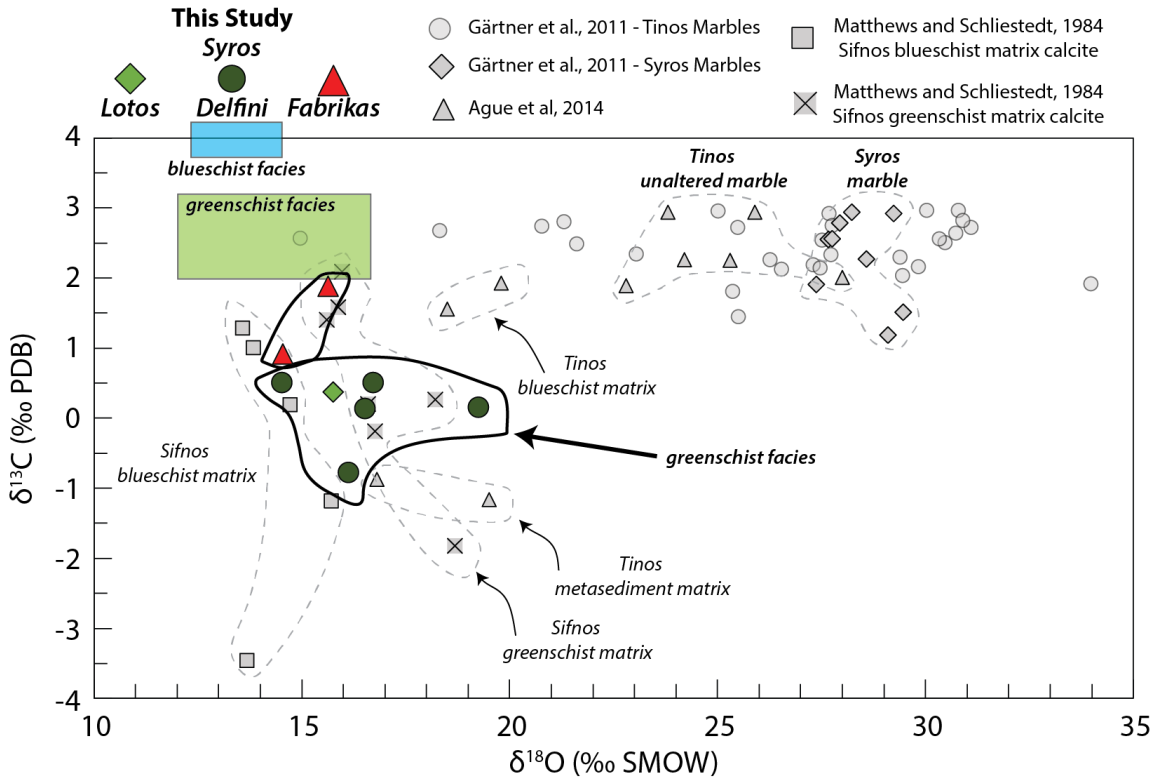

Figure 5.9: $\delta^{18}O$ and $\delta^{13}C$ values of boudin neck calcites from Syros, Greece. Oxygen and carbon isotope ratios are compared relative to reference marbles, and calcite in blueschist to greenschist facies rocks from previous studies on Syros, Tinos, and Sifnos (Matthews and Schliestedt 1984; Gärtner et al. 2011; Ague and Nicolescu 2014). $\delta^{18}O$ and $\delta^{13}C$ values of H_2O and CO_2 in equilibrium with calcite from boudin neck calcites that formed near greenschist facies metamorphic conditions (~ 373 – 419 °C) are illustrated by the green box. $\delta^{18}O$ and $\delta^{13}C$ values of H_2O and CO_2 in equilibrium with calcite from higher temperature boudin neck calcites (~ 452 – 544 °C) are illustrated by the blue box.

5.6 Discussion

5.6.1 Pressures Constraints Near the Tinos Detachment

Pressures determined from quartz-in-epidote barometry of samples from Panormos on Tinos, exhibit lower pressures than epidote growth conditions during greenschist facies metamorphism on Syros, even at temperatures up to 450 °C. The uncertainty of entrapment temperature leads to a large range of P_{ent}, with averages of ~675 MPa to ~831 MPa at 300

and 450 °C, respectively (n = 5, Table 5.1). Calculated geothermal gradients over this range of PT conditions would indicate a gradient of ~14 – 17 °C/km. These calculated geothermal gradients are elevated relative to those of Syros. The elevation of geothermal gradients between Syros and Tinos could represent the early stages of capture of the CBU on Tinos by core-complex detachments that root in ductile crust.

5.6.2 Evidence for Possible Interactions with Slab-Derived Fluids

Stable isotope measurements from Syros and Tinos are summarized in Figures 5.8 and 5.9. The focus of this discussion will be on the fluid chemistry of boudin necks, because they present major fluid conduits during retrograde metamorphism and are less likely to have been chemically buffered by surrounding rocks, or altered by late-stage normal faulting that has been well documented on Syros (Keiter et al. 2004, 2011). Oxygen and hydrogen isotope compositions of high-pressure metabasalts and metagabbros Sifnos, Syros, and Tinos have been well studied (Putlitz et al. 2000, Fig. 5.8A, B). High-pressure blueschist and eclogite mineral separates have $\delta^{18}O$ compositions that mimic hydrothermal alteration of oceanic crust, wherein upper oceanic crust experiences low-temperature seawater alteration, causing an increase in $\delta^{18}O$ values of minerals relative to the mantle, and gabbroic oceanic crust experiences high-temperature seawater alteration and a decrease in $\delta^{18}O$ values relative to mantle (Fig. 5.8A). $\delta^{18}O$ values determined in this study from mineral separates of blueschist facies banded tuffitic schists from Azolimnos exhibit a narrow $\delta^{18}O$ range, and have isotopic compositions that are similar to igneous volcanic rocks, such as andesites (continental and oceanic arcs), and rhyolites (e.g., Yellowstone) (Fig. 5.8A; Bindeman 2008).

Samples analyzed from greenschist facies rocks from Lotos, that include veins, fold hinges, and foliation matrix, and greenschist facies boudin quartz-calcite pairs from Lotos and Delfini, indicate fluid isotopic compositions that are enriched in ^{18}O relative to high-pressure basalts, gabbros, and volcanic igneous rocks (Fig. 5.8A). The oxygen isotope fluid compositions in equilibrium with quartz and calcite from boudin necks, indicate a $\delta^{18}O$ range of + 12.0 to + 16.1 ‰ (n = 5, quartz), and + 11.8 to + 16.6 ‰ (n = 6, calcite) (Fig. 5.8A, Table 5.2). The tight range of $\delta^{18}O$ values of fluids across Lotos and Delfini, suggests that a common metamorphic fluid may have been present across different lithologies during greenschist facies boudin neck formation. This would suggest that fluid isotopic compositions recorded by boudin necks exhibit minimal buffering by regional fluids. The similarity in quartz $\delta^{18}O$ values from boudin necks, hinges, and foliation matrix, may also suggest that quartz from all samples experienced precipitation, recrystallization, or re-equilibration of oxygen isotopes with a common fluid source during exhumation.

The presence of similar boudin neck isotope compositions would require fluids with high H_2O/CO_2 ratios and/or high fluid-rock ratios. Previous studies have noted that fluid inclusion from Syros blueschists and greenschists appear to be almost pure H_2O, with no thermometrically detectable CO_2 (Barr 1990). Fluids with $\delta^{18}O$ values of $\geq \sim +12$ ‰ are generally considered to be derived from dehydration of oceanic crust (basalts) that has undergone low-temperature hydrothermal alteration and/or dehydration of sediments/sedimentary rocks (Sharp 2017). Production of $\delta^{18}O$ values that approach ~ +12 to +16 ‰ from devolatilization of marbles is unlikely, as fractionation between CO_2 and calcite produces a CO_2 phase that is enriched in $\delta^{18}O$ relative to calcite (Scheele and Hoefs 1992; Hu and Clayton 2003; Sharp 2017). Marbles across Syros and Tinos exhibit $\delta^{18}O_{calcite}$ values that range from ~ + 15 to + 34 ‰ (average $\delta^{18}O \approx + 27 \pm 3.7$ ‰, 1σ, Fig. 5.9)

(Gärtner et al. 2011; Ague and Nicolescu 2014). It is possible that many of the low $\delta^{18}O$ values of Tinos marbles may reflect partial devolatilization or alteration of calcite catalyzed by fluid circulating along the Tinos detachment, into the CBU footwall, or alteration adjacent to veins. Unaltered marbles from Tinos that were sampled away from veins or apparent field alteration, exhibit a much tighter range of $\delta^{18}O$ values that range from + 22 ‰ to + 28 ‰ (n = 5, Fig. 5.9) (Ague and Nicolescu 2014). Similarly, marbles from Syros (Kampos and Kini), where detachment faulting is more limited, exhibit a tight range of $\delta^{18}O$ values that range from ~ + 27 to + 29 ‰ (n = 9, Fig. 5.9) (Gärtner et al. 2011).

If Syros and Tinos marbles represent the $\delta^{18}O$ value of carbonate at depth, devolatilization of unaltered marbles would produce CO_2 that is enriched by ~7 to 8 ‰ relative to carbonate between 400 – 600 °C, producing CO_2 $\delta^{18}O$ values ranging from ~ + 29 to + 38 ‰, values that are far removed from those determined from boudin neck samples. Therefore, the dehydration of altered oceanic crust or sediments at depth reflects the most likely source contributing to regional metamorphic H_2O fluids during greenschist facies metamorphism. Paleogeographic constraints suggest that subduction of the CBU was followed by subduction of the Gavrovo-Tripolitza unit (Roche et al. 2016). The unit is composed of pelitic sediments and volcanics, overlain by a platform sequence, followed by flysch deposits (Jolivet and Brun 2010). $\delta^{18}O$ values determined in this work would agree with paleogeographic reconstructions that indicate subduction of sediments of the Gavrovo-Tripolitza unit in the Oligoene, or continued subduction and dehydration of deeper oceanic crust and sediments.

The hydrous silicates from Syros exhibit a wide range of δD values (Fig. 5.8B). Chapter 4 describes the petrographic evolution of greenschist facies metamorphism on Lotos from petrographic observations. Briefly chlorite crystallization presents that last

stage of mineral crystallization, that is temporally most closely associated with boudinage of epidote and precipitation of calcite-quartz pairs. This is evidenced in thin section by late-alteration of the foliation matrix as shown by actinolite pseudomorphs being replaced by chlorite, suggesting that chlorite crystallization may represent the last stages of greenschist facies metamorphism. Hydrogen isotopes are good tracers of fluids, because the low hydrogen content of metamorphic rocks make buffering of the hydrogen isotope composition of fluids by rocks difficult, thus fluids are less susceptible to alteration from source-to-sink. δD values of fluids, calculated from δD values of chlorite from Lotos at an assumed temperature of 400 °C (average greenschist facies boudin neck T), indicate δD values of fluids that range from -10 to -19 ‰ (Table 5.2, Fig. 5.8B). These high values possibly indicate derivation of fluids from an oceanic source, that can be consistent with marine fluids, dehydration of ocean altered basalts, dehydration of serpentinite, or dehydration of sediments that interacted with seawater (Wickham and Taylor 1985; Sharp 2017), in agreement with $\delta^{18}O$ results. δD values of chlorite and white mica from Fabrika metasediments and blueschists indicate interaction with fluids similar to those described for Lotos. The proximity of these samples to late-stage normal faults; however, makes their interpretation difficult, and possible interaction of these hydrous silicates with late-stage Aegean seawater transferred along normal faults, cannot be excluded.

Boudin neck samples collected at Fabrika record higher temperatures. The higher temperatures are consistent with the presence of abundant glaucophane within the matrix of epidote boudins and the predominance of blueschist facies rocks in outcrop (Fig. 5.3G, H). It is possible, therefore, that samples record temperatures that are consistent with conditions during blueschist facies metamorphism, and fluids prevalent during this stage of PT conditions. Fluids in equilibrium with quartz and calcite at determined T conditions

of 452 and 544 °C, indicate fluid $\delta^{18}O$ values that range from + 13.3 to + 13.3 ‰ (n = 2, quartz) and + 12.5 to + 14.5 ‰ (n = 2, calcite) (Table 5.2, Fig. 5.8A). These fluid $\delta^{18}O$ values are similar to those determined to be present during greenschist facies metamorphism and may indicate that the predominant H_2O source during these two stages of exhumation remained constant.

$\delta^{13}C$ values of boudin neck calcite that precipitated during greenschist facies metamorphism display a remarkably tight range of $\delta^{13}C$ values that range from -0.77 to + 0.51 ‰ (n = 6, Table 5.2, Fig. 5.9). The $\delta^{13}C$ composition of CO_2 in fluids that is in isotopic equilibrium with calcite would range from $\delta^{13}C \approx$ + 1.9 to + 3.2 ‰ (n = 6, Table 5.2, Fig. 5.9). $\delta^{13}C$ values of calcite from boudin neck precipitates from higher temperature Fabrika samples, also show minimal variation in $\delta^{13}C$ values and range from + 0.81 to + 1.79 ‰ (n = 2, Table 5.2, Fig. 5.9). The $\delta^{13}C$ composition of CO_2 in fluids that is in isotopic equilibrium with calcite would range from $\delta^{13}C \approx$ + 3.5 to + 4.6 ‰ (n = 2, Table 5.2, Fig. 5.9). These results may suggest that blueschist-to-greenschist facies boudin neck calcites record a CO_2 evolution that indicates CO_2 was sourced from a lower $\delta^{13}C$ source at shallower depths; however, our data is limited (Fig. 5.9).

Potential sources that can produce CO_2-rich fluids during exhumation of the Cycladic islands has rarely been studied. Carbon-rich sources that could potentially contribute to the CO_2 budget in the Cyclades include marine marbles, graphitic schists, mantle devolatilization, and to a lesser extent, dehydration of carbon-poor metasediments and metabasites. Previous models that have been proposed to explain expulsion of CO_2-rich fluids on Naxos have included: 1) devolatilization of mantle, producing a $\delta^{13}C$ composition of -4 to -8 ‰ (Schuiling and Kreulen 1979), and 2) mixing of fluids derived from devolatilization of metasedimentary rocks, fluid/melt partitioning, and decarbonation

of marbles (Buick and Holland 1991). Slightly negative $\delta^{13}C$ values of CO_2-rich fluid inclusions from Naxos have been explained by mixing of fluids from decarbonation of marble, that would produce slightly positive $\delta^{13}C$ values, and CO_2 produced by oxidation of organic matter (e.g., graphitic schists and quartzites) (Kreulen 1980; Siebenaller et al. 2013). $\delta^{13}C$ values of marbles on Syros and Tinos exhibit a small range from $\delta^{13}C \approx + 1.1$ to + 3.0 ‰, and average $\delta^{13}C \approx + 2.4$ ‰ (± 0.4, 1σ) (Gärtner et al. 2011; Ague and Nicolescu 2014). CO_2 produced from decarbonation of marbles would produce CO_2 with $\delta^{13}C$ values that is ~ 2.7 ‰ heavier than carbonates at most temperatures (Ohmoto 1972; Sharp 2017). Therefore, marble decarbonation would produce CO_2 with $\delta^{13}C$ values that range from + 3.8 to + 5.8 ‰, averaging ~ + 5.1 ‰. These values would be too high to explain the $\delta^{13}C$ values of greenschist facies boudin neck calcite and would require a ^{13}C-depleted source to mix with carbonates. Mixing of CO_2 from oxidation of graphitic schists with CO_2 produced from marble decarbonation, could potentially lower the $\delta^{13}C$ value of CO_2, to better agree with calculated CO_2 $\delta^{13}C$ values, in agreement with previous studies (Kreulen 1980; Siebenaller et al. 2013).

The higher $\delta^{13}C$ values of CO_2 compositions calculated from higher temperature boudin neck calcite precipitates from Fabrika, could primarily be sourced from a different carbon reservoir. The $\delta^{13}C$ composition of CO_2 in fluids that is in isotopic equilibrium with calcite would range from $\delta^{13}C \approx + 3.5$ to + 4.6 ‰ (n = 6, Table 5.2, Fig. 5.9). CO_2 primarily produced from the decarbonation of marbles would be in good agreement with the carbon isotope composition of this early boudin generation. Alternatively, calcite $\delta^{13}C$ values of blueschist and greenschist facies rocks have not been well characterized, and dissolution/reprecipitation of calcite by H_2O-rich fluids could produce $\delta^{13}C$ CO_2 values that correspond to those recorded by blueschist and greenschist facies boudins. Data from

previous studies that characterize calcite $\delta^{18}O$ and $\delta^{13}C$ values of blueschists and greenschists, show overlap in carbon isotope compositions with those of boudin necks. It is possible that calcite $\delta^{13}C$ values primarily reflect dissolution and reprecipitation of matrix calcite; however, this conclusion would be difficult to reconcile with the tight range in $\delta^{13}C$ fluid values recorded by boudin necks, and the large range of $\delta^{13}C$ values from matrix calcite. Nonetheless, the possibility cannot be excluded.

5.6.3 Detachment Related Fluids

Hydrogen isotope measurements of chlorite beneath the Tinos detachment, indicate much more negative δD values that range from -82 to -86 ‰. The timing of and thus temperature of chlorite and quartz crystallization is unknown, but previous studies have shown that near the Tinos detachment, a sharp temperature decrease (~ 150 °C adjacent to detachment) is observed along with a decrease in $\delta^{18}O$ values of fluids in equilibrium with quartz and calcite ($\delta^{18}O_{fluid} \approx 0$ ‰). The two Tinos samples are taken ~200 meters away from the Tinos detachment, where the effects of this temperature decrease have been shown to be minimal, and samples record temperatures of ~300°C to 400 °C during all stages of detachment-related deformation (Famin et al. 2004). At temperatures between ~300 °C – 400 °C, measured hydrogen and oxygen isotope ratios of chlorite and quartz would suggest fluid δD and $\delta^{18}O$ fluid values between ~ -47 to -54 ‰ and + 9.1 to + 12.1 ‰, respectively. Similar values of surficial fluids have been noted on Naxos, wherein fluid inclusion formed at ~ 250 °C indicate aqueous fluids of meteoric origin characterized by δD values between – 40 ‰ to -46 ‰. The preservation of high $\delta^{18}O$ values may reflect the greater abundance of oxygen in rocks, relative to hydrogen, making the oxygen isotopic composition of surficial fluids transferred into the footwall rock-buffered, but not hydrogen buffered. Only

in close proximity to the detachment, is the circulation of meteoric waters reflected by the oxygen isotope composition (Famin et al. 2004). The current, near sea-level elevation of Tinos suggests meteoric water values of $\delta^{18}O \approx -5$ ‰ and $\delta D \approx -30$ ‰ (Bowen 2009). Higher paleo-elevations would decrease $\delta^{18}O$ and δD values. Isotopic resetting of chlorite δD values by meteoric water at the surface is also possible and cannot be confidently excluded.

5.6.4 Exhumation Implications

The evident differences between greenschist facies metamorphism on Syros and Tinos is expressed by the differing kinematics, PT conditions, and fluid history recorded on both islands. The CBU on both islands record different stages of their exhumation histories, and the mechanisms that exhumed HP/LT rocks on both islands may have also differed. Exhumation of Syros occurred during early exhumation occurred under a cold geothermal gradient of ~ 9 - 12 °C/km during changing kinematics (see Chapter 4 for discussion), whereas as lithologies from Tinos appear to have experienced near isothermal decompression, as suggested by temperatures estimates of blueschist (~450 – 500 °C) and younger greenschist facies metamorphism between ~21 – 32 Ma (~440 – 470 °C) (Bröcker et al. 1993). Assuming epidote growth during ambient greenschist facies metamorphic conditions that have been determined from samples (quartz-magnetite oxygen isotope thermometry; Bröcker et al. 1993) > ~ 200 meters away from the Tinos detachment, greenschist facies metamorphism occurred under a gradient of ~ 17 °C/km. These PT conditions condition suggest a geothermal gradient during greenschist facies metamorphism on Tinos that is elevated by ~ 5 – 8 °C/km, relative to Syros. The entrapment pressure conditions determined from epidote would also be consistent with

epidote growth when the Tinos detachment was active, whose ductile root has been estimated to reach ~30 km (Brichau et al. 2007). However, the calculated entrapment pressures cannot differentiate between the stage of growth that epidote is associated with.

A schematic model of the exhumation history of the CBU on Syros is shown in Figure 5.10. A comparison between mechanisms that exhumed the CBU on Syros and Tinos from deep depths is discussed below but cannot be quantitatively compared with the data from this study because of the lack of structural context of greenschist facies rocks from Tinos, thus remains only speculative. Subduction of the CBU preserved on Syros prior to the CBU on Tinos is demonstrated by older ages of HP/LT metamorphism (~ 1.5 GPa and 500°C on both islands), around ~ 50 Ma (Tomaschek et al. 2003; Lagos et al. 2007) on Syros, relative to Tinos (~40 - 44 Ma, Bröcker et al. 1993; Bröcker and Franz 1998). Syros CBU then initially underwent exhumation under a cold geothermal gradient, in a subduction channel geometry (Fig. 5.10), whereas based on current PT constraints, the CBU on Tinos underwent exhumation under a warmer gradient. Retrograde metamorphism of the CBU on Syros that is documented in this study would therefore be consistent with having occurred within a cold forearc position, prior to back-arc extension in the Cyclades that exhumed the CBU on Syros rapidly around 8 – 10 Ma based on apatite and zircon (U-Th)/He thermochronometry (Soukis and Stockli 2013).

Several mechanisms may possibly explain such contrasts in gradients on both islands. Although age constraints for D_{t1} and D_{t2} deformation on Syros are not well established, the PT path from Syros indicates near incipient exhumation upon reaching high-pressure conditions, as indicated by the lack of cooling at constant pressure that would be indicative of underplating and refrigeration of hanging wall by subducting lithosphere (Fig. 5.10A). Therefore it is possible that Syros was exhumed to shallow depths prior to

Tinos, as has been suggested by Parra et al. (2002). This may be supported by a range of ages that been determined from Rb-Sr dating of greenschist facies samples from Foinikia and North Oros Syringas, whose Rb-Sr ages range predominantly from ~30 – 34 Ma; however one phengite grain exhibits a Rb-Sr ages of 23 Ma (Cliff et al. 2017), whereas Tinos greenschist facies samples Rb-Sr ages range from ~21 – 32 Ma, with a group of ages that cluster around 21 – 24 Ma (Bröcker and Franz 1998). The exhumation of the CBU on Tinos after Syros may have occurred in a different geometry, wherein a portion of exhumation occurred early within a forearc position (Syros), but trench migration may have moved Tinos to a warmer geothermal gradient, while Syros was already at shallower depths. Conversely, Tinos CBU could have been exhumed under a warmer gradient near the subduction zone, due to slab rollback, and potential influx on warm asthenosphere, or can record a warmer gradient due to the proximity of Tinos greenschists to emplacing plutons.

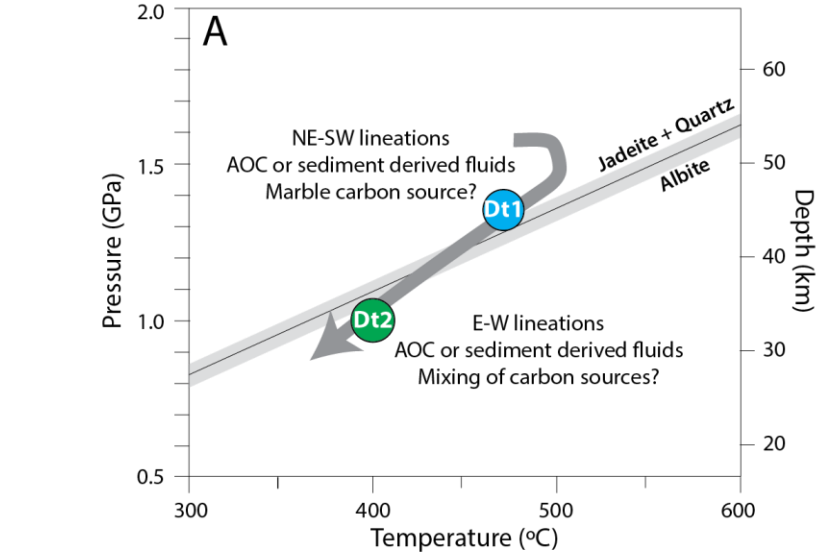
A
2.0
1.5
1.0
0.5
Pressure (GPa)
60
50
40
30
20
Depth (km)
300
400
500
600
Temperature (°C)
NE-SW lineations
AOC or sediment derived fluids
Marble carbon source?
Dt1
Jadeite + Quartz
Albite
Dt2
E-W lineations
AOC or sediment derived fluids
Mixing of carbon sources?

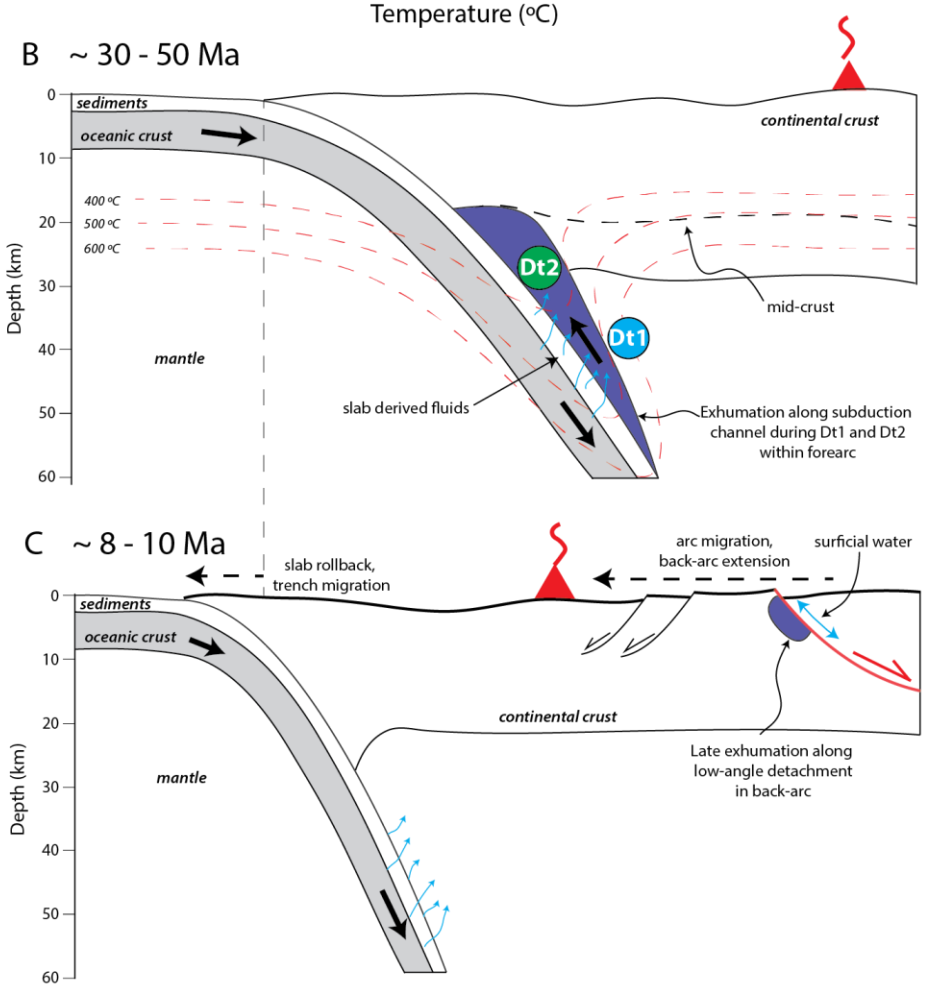
B ~ 30 - 50 Ma
sediments
oceanic crust
continental crust
400 °C
500 °C
600 °C
Depth (km)
mantle
Dt2
Dt1
mid-crust
slab derived fluids
Exhumation along subduction channel during Dt1 and Dt2 within forearc
C ~ 8 - 10 Ma
slab rollback, trench migration
arc migration, back-arc extension
surficial water
sediments
oceanic crust
continental crust
mantle
Depth (km)
Late exhumation along low-angle detachment in back-arc

Figure 5.10: Schematic illustration of exhumation of the CBU on Syros, Greece and related kinematic and PT conditions, and associated fluids. A) The CBU from Syros, Greece underwent cooling during decompression, under a depressed geothermal gradient of ~ 9-12 °C/km. Changing kinematic conditions during exhumation are indicated by swinging lineations from the NE-SW to lastly E-W. Exhuming CBU rocks from Syros show evidence for continuous interaction with altered oceanic crust (basalts) or sediment derived fluids. A possible change in carbon source occurred between D_{t1} and D_{t2} deformation conditions. B) Schematic illustration that shows early exhumation of the CBU in a forearc within a subduction channel, and C) late capture by core-complex detachments (red line) in a back-arc. Blue arrows indicate the direction of fluid movement into the subduction channel and along low-angle detachment, and black arrows indicate the direction of descending and ascending rocks.

5.7 CONCLUSIONS

These results suggest that the CBU on Syros and Tinos, Greece record different stages of retrograde metamorphism, that are best described by blueschist-to-greenschist facies metamorphism on Syros that occurs in a subduction channel geometry within a cold forearc, and greenschist facies metamorphism on Tinos that is partly attributed to core-complex detachment faulting. The following data and observations suggest different exhumation histories during greenschist facies metamorphism on both islands, and perhaps before:

1) Coaxial vs non-coaxial strain recorded by greenschist facies lithologies during formation stretching lineations towards the E-W and NE-SW on Syros and Tinos, respectively.
2) Cooling during decompression under a depressed geothermal gradient of ~9 - 12 °C/km on Syros, and an elevated geothermal gradient on Tinos of ~13 – 17 °C/km during greenschist facies metamorphism.
3) Interaction of exhuming rocks with slab-derived fluids derived from altered oceanic crust or sediments during greenschist-to-blueschist facies metamorphism, as indicated by high $\delta^{18}O$ values, and possibly unique carbon sources during a

transition from blueschist-to-greenschist facies conditions recorded on Syros. Tinos samples record possible interaction with surficial (meteoric) fluids, as indicated by low δD values of chlorite (δD < -80 ‰), a conclusion that has been suggested in previous studies.

4) Carbon isotopes of calcite from boudin necks indicates that CO_2 during exhumation may be derived from decarbonation of marbles, and/or mixing of CO_2 from marbles and a lower $\delta^{13}C$ source such as graphitic schists, or internal dissolution and reprecipitation of matrix calcite.

Chapter 6: Conclusions

This dissertation highlights the many applications of elastic thermobarometry that remain unexplored, the potential of the technique in future studies, and how elastic thermobarometry, stable isotope geochemistry, and structural constraints, can be integrated to elucidate the exhumation history of metamorphic rocks. The results of this dissertation can be summarized as follows:

Chapter 2 shows presents new elastic thermobarometers, a script that can be used to carry-out elastic calculations, and the potential of three inclusion host pairs: apatite-olivine, quartz-in-epidote, and rutile-in-pyrope. Apatite-in-olivine and quartz-in-epidote exhibit good potential, whereas the rutile-in-pyrope fails.

Chapter 3 shows the potential of the quartz-in-epidote barometer, wherein the calculated entrapment pressures from residual quartz inclusion pressures show good agreement with reference and petrographic constraints. The anisotropic inclusion-host pair also shows minimal temperature dependence of calculated entrapment pressures.

Chapter 4 uses structural constraints, quartz-in-epidote barometry, and stable isotope thermometry to provide constraints on the exhumation history of high-pressure rocks from Syros, Greece. Results are consistent with stages of deformation that record a change of kinematics from subduction through exhumation and suggests that Syros underwent incipient cooling during decompression after reaching maximum high-pressure/low-temperature conditions, consistent with a cold PT evolution that is indicative of exhumation adjacent to a subduction zone boundary within a subduction channel prior to core-complex capture.

Chapter 5 uses $\delta^{18}O$, δD, and $\delta^{13}C$ values of epidote boudin neck quartz-calcite pairs and mineral separates that record greenschist facies metamorphic conditions, that

indicate possible interaction with fluids derived from dehydration of altered oceanic crust (basalts) and/or sediments, and a low $\delta^{13}C$ carbon source. The fluid history of greenschist facies samples from below the Tinos detachment indicate possible late-stage interaction with meteoric water. The contrasting fluid histories present differences in the tectonic position of rocks preserved on both islands during exhumation.

Appendices

APPENDIX A: SUPPLEMENT TO CHAPTER 2

A.1 Previous Work

This study follows up some of the preliminary work completed by (Kohn 2014) and Angel et al. (2017b, 2014b). The previous work is significant in that it presents 48 suitable inclusion-host pairs that have been modelled and fit by linear regressions that users can implement. Some of the problems arising from utilizing this approach is that the derived empirical equations have PT limitations where fit is appropriate for the modelled data. Furthermore, the implementation of linear fits to the modelled data provides added uncertainty that is not quantified by the empirical equations. The study by Kohn (2014) provides many suitable barometers and thermometers that can be used for constraining PT conditions of metamorphic rocks, and some plutonic rocks. However, the work primarily presents many inclusion-host pairs that implement metamorphic porphyroblasts and common accessory phases in metamorphic and igneous rocks. We expand on the previous work by expanding the applicability of solid mineral inclusion thermobarometry by providing a larger suite of inclusion-host pairs that can be used, over a wider range of PT conditions that can be modelled.

A.2 Supplementary Data and Code

The inputs from the Matlab and Python GUI's are run through multiple scripts that calculate entrapment pressure and temperature conditions. The script "elastic_model" incorporates the manually input GUI values to solve the Guiraud and Powell (2006) with the Angel et al. (2017b) correction. The elastic model requires calculation of P_{foot} (see text), which is calculated in the script "elastic_model_P_foot". Throughout calculations in both

scripts, solutions for molar volumes from equations of state are calculated in the script "eos". All variables called for in the equations of state are derived from the excel spreadsheet "thermodynamic_properties". To access the files necessary to run the script, please visit the UT-Austin repository to access the zip files containing the accessible code. Files are accessible through the Chapter 2 supplement zip file. To run the Matlab or Python scripts, open the folder for your preferred interface: "solid_inclusion_calculator_matlab" or "solid_inclusion_calculator_python". Open the file "solid_inclusion_calculator_instructions.txt" in the appropriate folder and follow the instructions. Results from inclusion-host pair tests are also give in the supplemental excel file, "supplementary_table_1".

A.3 Mineral Compositions

The elastic properties of some minerals vary appreciably as a function of composition (e.g., feldspars, epidote, garnet). We report previously published compositions for fayalite from the Central Plateau Member Rhyolites of Yellowstone and for garnet from the Verpeneset eclogite in Western Gneiss Region of Norway (Befus and Gardner 2016; Krogh 1982). There are no published compositions for the apatite and rutile inclusions from these locations. We assume pure endmember compositions for rutile and albite. We assume an epidote composition of $X_{ep} = 0.5$ and $X_{cz} = 0.5$. See our text discussion for how we estimated our apatite composition. In the discussion, we demonstrate how we best estimate the composition of apatite and show how compositional uncertainties could affect resulting PT estimates.

APPENDIX B: SUPPLEMENT TO CHAPTER 4

B.1: Sample Descriptions

B.1.1 Kalamisia

Sample Name: KCS70A

Sample Orientation: Perpendicular to foliation, parallel to stretching lineation.

Rock Type: Metabasite – blueschist facies

Primary Mineralogy: omphacite + garnet + glaucophane + epidote + white mica + oxides + minor albite and quartz

Lineation orientation: NE-SW

Petrography: Foliation (S_s) is defined by elongate minerals that include omphacite, glaucophane, epidote, and white mica. Garnets are rotated by the primary foliation and often contain glaucophane pressure shadows and precipitation of glaucophane within brittle garnet fractures. No internal foliation is well developed within garnets. Omphacite displays alteration and breakdown to glaucophane. Glaucophane inclusions within epidote that are oriented parallel to foliation are common, and no epidotes in this sample exhibit brittle fracturing parallel to stretching lineations. No omphacite is observed as inclusion within epidote, further supporting epidote growth during retrograde metamorphism.

Location: 37.420056, 24.956639

B.1.2 Lotos

Sample Name: SY1402 (Fig. B2A)

Sample Orientation: Perpendicular to foliation, parallel to stretching lineation.

Rock Type: Metabasite – greenschist facies

Lineation orientation: E-W

Primary Mineralogy: epidote + white mica + amphibole + chlorite + albite + quartz + calcite + oxides

Petrography: Foliation (S_s) is well-defined by epidote, white mica, amphibole, and chlorite. Epidote is poikiloblastic, with inclusions that include glaucophane within the core (rare) and more winchite composition amphiboles towards the rim (Fig. B2C, D, E). Matrix green amphibole (winchite core) is overgrown by white amphibole rims (actinolite, Fig. B2D). Multiple generations of epidote may be evident, as one has a short b-axis and appears to be inclusion free. Brittle boudinage of epidote parallel to the orientation of stretching lineations is common and is followed by precipitation of quartz and calcite within boudin necks. Boudin neck quartz exhibits constant extinction. Minor chlorite appears within epidote porphyroblasts, but most commonly precipitates within foliation matrix and sometimes pseudomorphs matrix green amphibole. Albite commonly has glaucophane or winchite inclusions, but some albite seems to pseudomorph matrix green amphibole and one albite encapsulates actinolite.

Location: 37.443320, 24.896870

Sample Name: SY1405 – greenschist facies

Sample Orientation: Perpendicular to foliation, parallel to stretching lineation.

Rock Type: Metabasite

Lineation orientation: E-W

Primary Mineralogy: epidote + white mica + garnet + amphibole + chlorite + albite + quartz + calcite + oxides

Petrography: The petrographic of this sample is similar to that described for sample SY1402, but this sample contains garnets with an internal foliation (S_r) that is oblique to the primary foliation (S_s) (Fig. B2B).

Location: 37.443630, 24.897230

Sample Name: KCS2

Sample Orientation: Perpendicular to foliation, parallel to stretching lineation.

Rock Type: Metabasite – greenschist facies

Lineation orientation: E-W

Primary Mineralogy: white mica + epidote + quartz + albite + calcite + oxides + minor actinolite, chlorite and oxides

Petrography: The foliation (S_s) is primarily defined by white mica and epidote. Epidotes are usually large, poikiloblastic porphyroblasts, and are commonly boudinaged with quartz + calcite boudin neck precipitates. Quartz within boudin necks exhibits constant extinction. Actinolite is rare and only occurs within the matrix foliation. The section shows a progressive mineral evolution of greenschist facies minerals with actinolite being pseudomorphed and/or replaced by late calcite + chlorite.

Location: 37.443306, 24.896861

Sample Name: KCS3

Sample Orientation: Perpendicular to foliation, parallel to stretching lineation.

Rock Type: Metasediment – greenschist facies

Lineation orientation: E-W

Primary Mineralogy: quartz + epidote + minor white mica, garnet, and chlorite

Petrography: The foliation (S_s) is predominantly defined by quartz, epidote, and white mica. Some epidotes are large and poikiloblastic and contain abundant quartz inclusions. A second morphology of epidotes contains less inclusions, but often still contains quartz. Both types of epidote are aligned parallel to the foliation. Chlorite is only found within the foliation matrix. The foliation wraps around rotated garnets.

Location: 37.443306, 24.896861

B.1.3 Delfini

Sample Name: KCS34

Sample Orientation: Perpendicular to fold axial plane.

Rock Type: Metasediment – greenschist facies

Lineation orientation: E-W

Primary Mineralogy: quartz + white mica + epidote + garnet + calcite + chlorite

Petrography: This section samples the core of the D_{t2} fold that refolds the primary foliation (S_s) and exhibits significant alteration and recrystallization. Epidote grains in this section exhibit a significant grain size reduction relative to all other sections (~50 – 400 μm in length parallel to long axis). Inclusions (including quartz) within these epidotes are rare. Chlorite appears patchy within matrix, but predominantly alters garnet. Garnets are significantly pseudomorphed by chlorite.

Location: 37.456790, 24.899162

Sample Name: KCS1621

Sample Orientation: Perpendicular to foliation, parallel to stretching lineation.

Rock Type: Metasediment – greenschist facies

Lineation orientation: E-W

Mineralogy: quartz + epidote + garnet + minor white mica and chlorite

Petrography: The foliation (S_s) is predominantly defined by quartz, epidote, and white mica. Most epidotes are large and poikiloblastic and contain abundant quartz inclusions. Large epidote porphyroblasts display a compositional transition in cross-polarized light that is accompanied by a significant decrease in inclusions from core-to-rim. Chlorite is only found within the foliation matrix. The foliation wraps around rotated garnets, and small garnets are sometimes included within epidotes that define the primary foliation. Elongated quartz inclusion within epidote sometimes define the internal foliation of epidote inclusions. Garnets do not preserve an internal foliation.

Location: 37.45646677, 24.89872299

B.1.4 Megas Gialos

Sample Name: KCS50

Sample Orientation: Perpendicular to foliation, parallel to stretching lineation.

Rock Type: Metasediment – greenschist facies

Lineation orientation: E-W

Mineralogy: quartz + epidote + chlorite + minor white mica

Petrography: The foliation is predominantly defined by quartz, epidote, and white mica. Most epidotes are large and poikiloblastic and contain abundant quartz inclusions. Glaucophane inclusions are rare, but do appear within epidote, and are aligned parallel to the primary foliation (S_s). Most amphiboles within epidote are green and are also aligned parallel to foliation. Chlorite only appears within the matrix but defines foliation well.

Location: 37.380139, 24.915111

B.1.5 Boudin Neck Samples

Sample Name: SY1613

Sample Location: Lotos

Outcrop Metamorphic Facies: Greenschist

Location: 37.44480118, 24.89873159

Sample Name: SY1617

Sample Location: Delfini

Outcrop Metamorphic Facies: Greenschist

Location: 37.45646677, 24.89872299

Sample Name: SY1618

Sample Location: Delfini

Outcrop Metamorphic Facies: Greenschist

Location: 37.45645416, 24.89873137

Sample Name: SY1623

Sample Location: Delfini

Outcrop Metamorphic Facies: Greenschist

Location: 37.454283, 24.897447

B.2: Analytical Methods

B.2.1 Thermobarometry Methods

B.2.1.1 Solid Inclusion Barometry

Measurements: Raman spectroscopy measurements of quartz inclusions within garnet and epidote were carried-out at Virginia Tech by using a JY Horiba LabRam HR800 Raman spectrometer with 1800 lines/mm grating. We used a 40x objective with a confocal aperture of 400 µm and a 150 µm slit width. Raman spectra were centered at 360 cm^{-1}. A 514.57 nm wavelength Ar laser with the laser interference filter removed was used for all analyses and allowed us to apply a linear drift correction dependent on the position of the 520.30 cm^{-1} Ar plasma line. Instrument standardization was carried out by measuring the position of the quartz 464 cm^{-1} peak in a Herkimer quartz standard 5 times prior to analysis. The quartz 464 cm^{-1} peak shift reflects the Si-O-Si stretching mode and this Raman peak was used because it exhibits a prominent frequency shift and has a high intensity (Hemley, 1987; Schmidt and Ziemann, 2000). All quartz Raman measurements were fit by using PeakFit v4.12 from SYSTAT Software Inc. A Gaussian amplitude model was used to fit Ar plasma lines, and the Pearson IV model was used to fit the quartz 464 cm^{-1} band, following the approach of Schmidt and Ziemann (2000). Only one peak was needed to fit the 464 cm^{-1} bands of quartz inclusions within garnet, but due to the overlap of the 464 cm^{-1} quartz peak and lower frequency epidote bands at ~ 422 cm^{-1} and 451 cm^{-1}, we applied multiple peak fitting approaches for the qtz-in-ep inclusion-host pair. We used one, two or three peaks to fit the quartz 464 cm^{-1} and shoulder epidote peaks. The number of peaks chosen depended on the quartz 464 cm^{-1} peak intensity and the ease with which it could be resolved from the epidote shoulder peaks. If quartz 464 cm^{-1} intensities were similar to epidote intensities, resolving epidote and quartz Raman bands required two or more peaks

due to broadening of the quartz peak if only one peak was used for fitting. See Chapter 3 and Ashley et al. (2016a) for more information about the peak-fitting approach used for Raman measurements of quartz within epidote and garnet. Measured quartz inclusions were small in diameter relative to the host to avoid geometric corrections (Mazzucchelli et al. 2018).

Inclusion and Entrapment Pressure Calculations: Residual quartz inclusion pressures were calculated from measured 464 cm^{-1} frequency shifts by using the Ashley et al. (2014a) Herkimer quartz polynomial equation that refit the Schmidt and Ziemann (2000) quartz Raman shift experiments. The 128 cm^{-1} and 206 cm^{-1} quartz Raman bands were not considered in this study because of their low intensities, and common interference with shoulder epidote peaks. Entrapment pressures were calculated from residual quartz inclusion pressures by using the Guiraud and Powell (2006) 1D elastic model equation, and following the approach outlined in Chapter 3. Quartz inclusions Raman shifts were measured from multiple epidotes and garnets within individual sections (Table B1). Calculated entrapment pressures from multiple quartz inclusions from one host generally suggest similar entrapment pressures. The largest pressure variation we noted from multiple quartz Raman measurements within one epidote host came from sample KCS50 (Megas Gialos), wherein calculated entrapment pressures range from 1376 – 1583 MPa (1 σ of average = 108 MPa, quartz inclusion #'s 2 – 4, host # 2, Table B1). We assumed constant mineral compositions for all modeling (epidote: $X_{ep} = 0.5$ and $X_{cz} = 0.5$; garnet: $X_{Alm} = 0.7$, $X_{Gr} = 0.2$, and $X_{Py} = 0.1$). The propagated errors reported in this study account for errors in peak fit statistics for the Ar plasma line and quartz 464 cm^{-1} peak, and instrument uncertainty based on the long-term standard deviation of Herkimer quartz measurements (~ ± 0.1 cm^{-1}).

B.2.2.2 Stable Isotope Thermometry

Measurements: Samples were measured by using a ThermoElectron MAT 253 isotope ratio mass spectrometer (IRMS) at the University of Texas at Austin. Quartz $\delta^{18}O$ values were measured by laser fluorination (Sharp 1990). Approximately 2.0 mg of quartz were used in each analysis. Quartz from sample(s) SY1613, SY1617, and SY1623 was duplicated to demonstrate isotopic homogeneity and reproducibility. An internal quartz standard Lausanne-1 ($\delta^{18}O$ = + 18.1‰) was analyzed with all samples to evaluate precision and accuracy. All $\delta^{18}O$ values are reported relative to standard mean ocean water (SMOW), where the $\delta^{18}O$ value of NSB-28 is +9.65‰. Measurement precision based on the long-term reproducibility of standards is ± 0.1 ‰ (1 σ). Precision of Lausanne-1 on day of analysis was ± 0.3 ‰ (1 σ), whereas samples reproduced with a precision of ± 0.1 ‰ (1 σ) or better (Table B2). Calcite $\delta^{18}O$ values were measured on a Thermo Gasbench II coupled to a ThermoElectron 253 mass spectrometer. Each analysis used 0.25 – 0.5 mg of calcite that was loaded into Exetainer vails were flushed with ultra-high purity helium and reacted with 103 % phosphoric acid at 50 °C for ~ 2 hours. Headspace CO_2 was then transferred to the mass spectrometer. Samples were calibrated to an in-house standard, NBS-18 and NBS-19. Measurement precision is ± 0.04 ‰ (1 σ) based on the long-term reproducibility of standards.

Temperature Estimates: Temperatures derived from stable isotope measurements were calculated by using the Sharp and Kirschner (1994) quartz-calcite oxygen isotope fractionation calibration. Isotopic equilibrium was assumed for all samples. Several observations support this assumption: 1) duplicate $\delta^{18}O$ analysis of quartz and calcite grains give the same isotopic value, suggesting grain isotopic homogeneity, 2) the stage of deformation that these mineral-pairs are related to, is not affected by further deformation,

in outcrop and thin section, and 3) all quartz-calcite pairs suggest a similar temperature of isotopic equilibration.

Temperature errors from oxygen isotope measurements were calculated through the square-root of the summed quadratures of all sources of uncertainty. These uncertainties included error of $\delta^{18}O$ values of quartz and calcite of ± 0.1 ‰ (1 σ) and ± 0.04 ‰ (1 σ), respectively. Errors from the sum of propagated analytical errors were propagated through the empirical calibration of quartz-calcite oxygen isotope fraction that was used for temperature calculations:

$$\Delta_{Qtz-Cc} = \frac{A \times 10^6}{T^2}$$

where A = 0.87 (± 0.06, 1 σ). The square-root the summed quadratures is expressed as:

$$\sigma_T = \sqrt{\sigma_A^2(\partial T/\partial A)^2 + \sigma_{\Delta_{Qtz-Cc}}^2(\partial T/\partial \Delta_{Qtz-Cc})^2}$$

$$\sigma_T = \sqrt{\sigma_A^2((0.5 * 10^3)/(\sqrt{A} * \sqrt{\Delta_{Qtz-Cc}}))^2 + \sigma_{\Delta_{Qtz-Cc}}^2(-0.5 * (\sqrt{A} * 10^3)/{\Delta_{Qtz-Cc}}^{1.5})^2}$$

B.2.2 Mineral Chemistry

B.2.2.1 Electron Microprobe Analyses

Measurements: Electron probe microanalysis measurements of amphibole compositions were carried out at the University of Texas at Austin on JEOL 8200 instrument equipped with five wavelength-dispersive spectrometers. Analyses were made on a thin section of sample SY1402 (Lotos). Amphiboles were analyzed for elements Na, Mg, Al, Si, K, Ca, Fe, and Ti, by wavelength-dispersive spectroscopy. Operating conditions employed a 1-μm beam size, 10 nA beam current and 15 keV accelerating voltage. All elements were measured for 30 s on peak and 15 s for both high and low

background measurements. Amphiboles were named according to the Hawthorne and Oberti (2007) classification scheme.

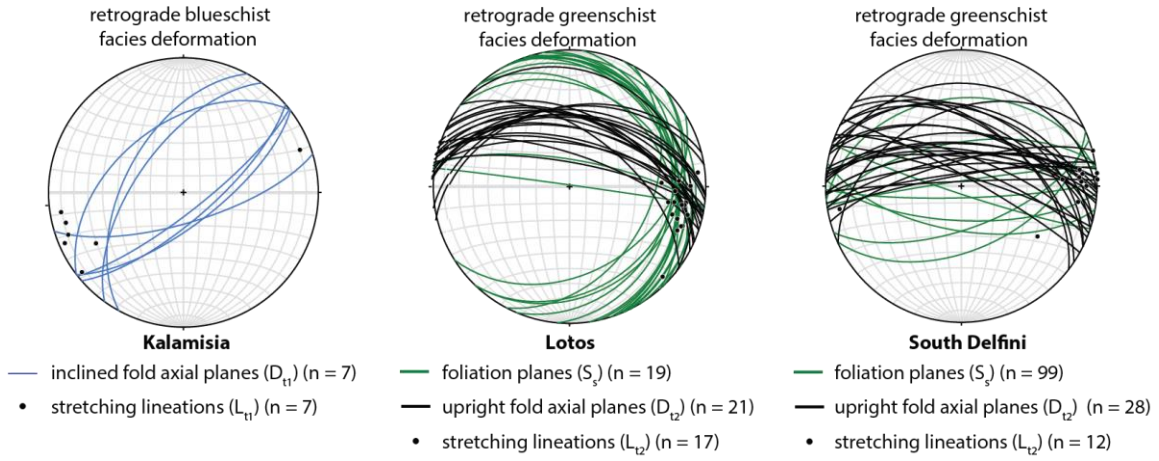

Figure B1: Stereonets from Kalamisia, Lotos, and Delfini, that show a progressive swinging of stretching lineations and changing kinematics from NE-SW and lastly towards the E-W.

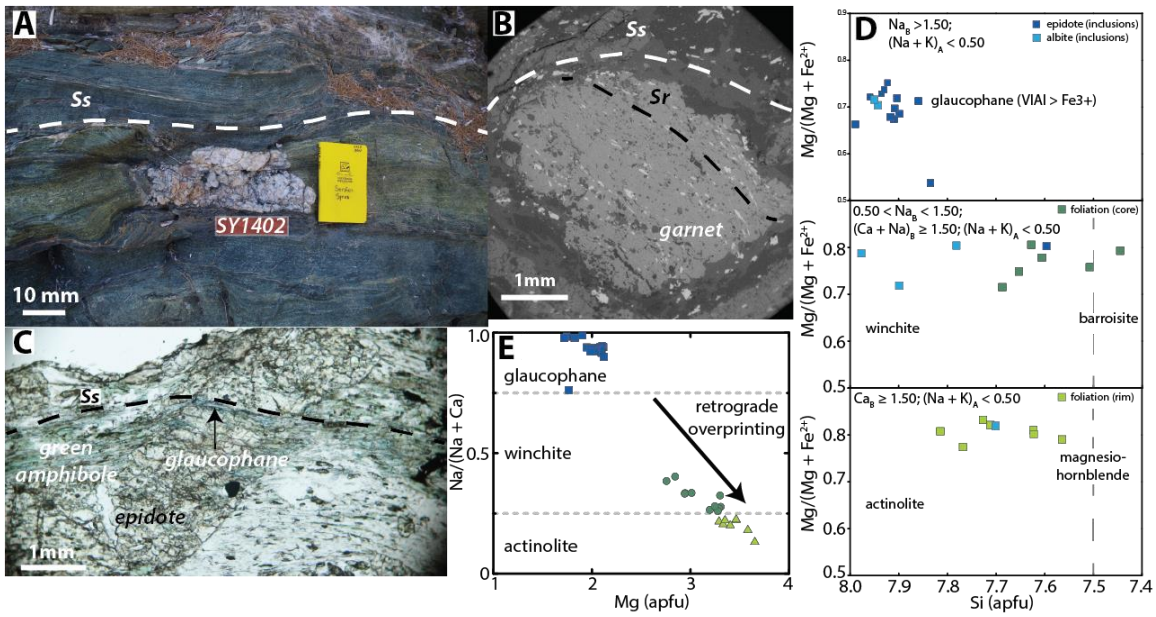

Figure B2: Example of outcrop to photomicrograph scale textural and mineral evolution of blueschist-to-greenschist facies mineralogy from Lotos. A: Example of an epidote boudin and location of sample SY1402 (highlighted by red box). B: Garnet foliation (S_r) oblique to the primary foliation (S_s) of sample SY1405. C: Glaucophane inclusion within amphibole that is aligned parallel to S_s foliation. Amphiboles further from the core and in the matrix transition to green colors in plane polarized light. D: Amphibole compositions (sample SY1402, Lotos) determined from different textural fabrics. Amphibole inclusions within epidote and albite contain both glaucophane (rare) and winchite. Matrix amphibole transitions to winchite cores with actinolite rims. E: Amphibole compositions (sample SY1402, Lotos) show decreasing Na content during retrograde metamorphism, indicative of decreasing PT conditions.

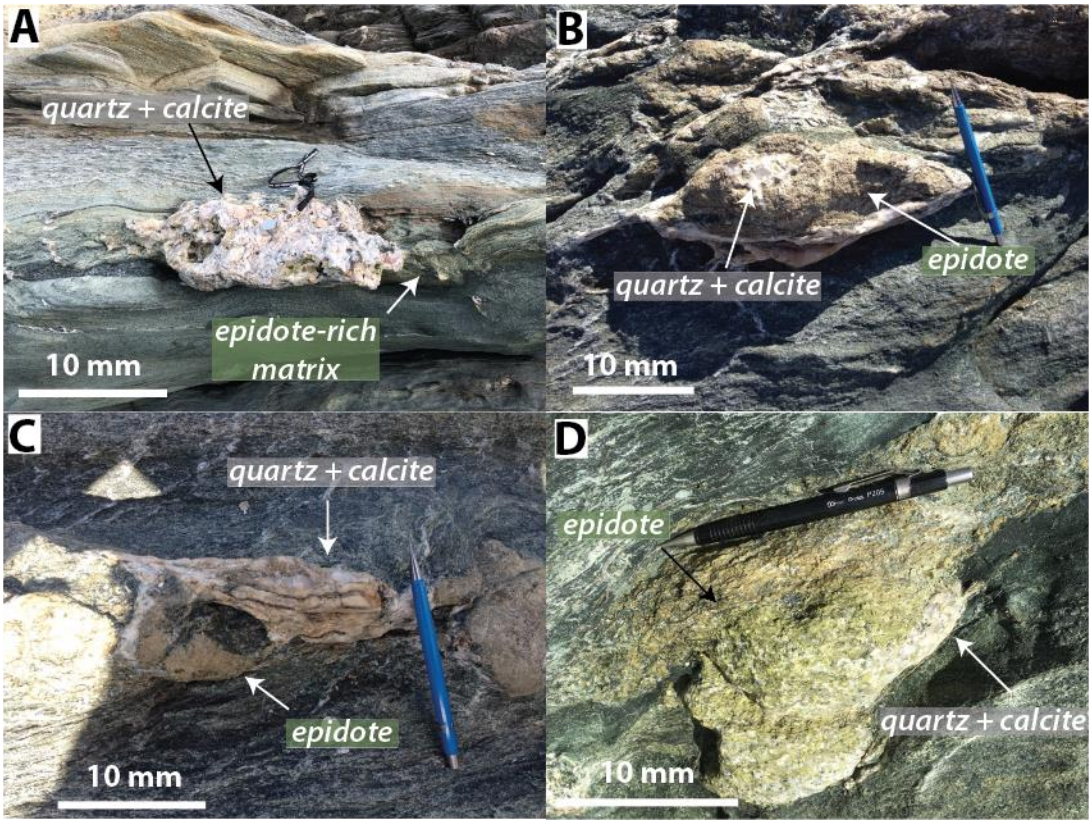

Figure B3: Outcrop photos of epidote boudins sampled for oxygen isotope thermometry. A: SY1613 (Lotos), B: SY1617 (Delfini), C: SY1618 (Delfini), D: SY1623 (Delfini).

Sample	Location	Host	Inclusion #	Host #	v464 (cm^{-1})	Δv464 (cm^{-1})	Pincl MPa	Pincl 1 σ Error (MPa)	Pent MPa	Pent 1 σ Error (MPa)	Population Group #	Group Mean (± 1 σ) MPa
KCS70A	Kalamisia	Garnet*	1	1	470.13	5.56	622	26	1459	45	1	**1396 (62)**
KCS70A	Kalamisia	Garnet*	2	1	470.13	5.57	623	24	1460	42	1	
KCS70A	Kalamisia	Garnet*	3	1	469.56	4.98	556	23	1343	41	1	
KCS70A	Kalamisia	Garnet*	4	2	469.68	4.81	536	30	1309	52	1	
KCS70A	Kalamisia	Garnet*	5	2	470.21	5.34	596	25	1414	43	1	
KCS70A	Kalamisia	Garnet*	6	2	470.10	5.23	584	25	1391	43	1	
KCS70A	Kalamisia	Epidote‡	1	1	469.27	4.14	460	26	1273	54	2	**1284 (115)**
KCS70A	Kalamisia	Epidote‡	2	2	469.70	4.99	556	23	1474	51	2	
KCS70A	Kalamisia	Epidote‡	3	3	468.67	3.89	432	25	1215	52	2	
KCS70A	Kalamisia	Epidote‡	4	4	469.24	4.08	454	24	1260	50	2	
KCS70A	Kalamisia	Epidote‡	5	4	469.59	4.44	494	24	1345	50	2	
KCS70A	Kalamisia	Epidote‡	6	5	468.71	3.55	394	24	1139	48	2	
KCS3	Lotos	Garnet*	1	1	471.21	6.88	773	24	1733	44	1	**1542 (270)**
KCS3	Lotos	Garnet*	2	2	469.50	5.03	561	23	1352	40	1	
KCS2	Lotos	Epidote‡	1	1	468.76	4.46	497	123	1348	265	2	**1411 (109)**
KCS2	Lotos	Epidote‡	2	1	468.38	4.08	454	24	1260	51	2	
KCS3	Lotos	Epidote‡	3	2	468.82	4.62	514	23	1386	49	2	
KCS2	Lotos	Epidote‡	4	3	469.29	4.83	539	23	1438	51	2	
KCS2	Lotos	Epidote‡	5	4	469.00	4.54	505	92	1367	200	2	
KCS2	Lotos	Epidote‡	6	5	469.63	5.17	577	105	1521	235	2	
KCS2	Lotos	Epidote‡	7	6	468.79	4.56	507	24	1371	51	2	
KCS2	Lotos	Epidote‡	8	6	468.08	3.92	435	24	1221	50	2	
KCS2	Lotos	Epidote‡	9	7	469.32	5.04	562	31	1488	70	2	
KCS3	Lotos	Epidote‡	11	9	468.32	4.19	466	24	1284	51	2	
SY1402	Lotos	Epidote‡	12	10	470.20	5.41	605	26	1580	59	2	
KCS3	Lotos	Epidote‡	15	12	470.43	5.22	583	23	1534	50	2	
SY1402	Lotos	Epidote‡	16	13	470.13	5.00	557	24	1478	51	2	
SY1402	Lotos	Epidote‡	17	13	470.15	5.02	560	23	1483	51	2	
KCS3	Lotos	Epidote†	10	8	466.99	2.64	292	24	938	48	3	**986 (64)**
SY1402	Lotos	Epidote†	13	11	467.98	3.22	357	23	1064	47	3	
SY1402	Lotos	Epidote†	14	11	467.58	2.73	302	23	957	46	3	

Table B1: Raman data of quartz-in-epidote-and-garnet measurements and calculated entrapment pressures.

KCS50	Megas Gialos	Epidote‡	1	1	469.23	4.42	492	18	1338	39	2	**1419 (86)**
KCS50	Megas Gialos	Epidote‡	2	2	469.57	4.76	531	114	1420	250	2	
KCS50	Megas Gialos	Epidote‡	3	2	469.37	4.58	510	16	1376	36	2	
KCS50	Megas Gialos	Epidote‡	4	2	470.22	5.42	606	20	1583	45	2	
KCS50	Megas Gialos	Epidote‡	5	3	469.54	4.73	527	16	1413	36	2	
KCS50	Megas Gialos	Epidote‡	5	3	469.42	4.60	512	17	1381	38	2	
KCS34	Delfini	Garnet*	1	1	470.28	5.62	628	23	1470	41	1	**1470 (116)**
KCS34	Delfini	Garnet*	2	1	470.97	6.31	708	23	1613	42	1	
KCS34	Delfini	Garnet*	3	2	470.32	5.64	631	23	1475	41	1	
KCS34	Delfini	Garnet*	4	3	470.41	6.11	684	23	1570	42	1	
KCS34	Delfini	Garnet*	5	3	470.41	6.10	684	25	1569	46	1	
KCS34	Delfini	Garnet*	6	4	469.37	5.13	573	23	1373	40	1	
KCS34	Delfini	Garnet*	7	4	468.99	4.56	508	24	1261	40	1	
KCS34	Delfini	Garnet*	8	4	469.80	5.43	606	24	1432	42	1	
KCS1621	Delfini	Epidote‡	1	1	469.17	4.59	511	23	1379	51	2	**1375 (77)**
KCS1621	Delfini	Epidote‡	2	2	469.15	4.53	504	23	1364	49	2	
KCS1621	Delfini	Epidote‡	3	3	469.61	5.04	562	24	1487	54	2	
KCS1621	Delfini	Epidote‡	4	4	469.04	4.57	509	24	1375	51	2	
KCS1621	Delfini	Epidote‡	8	8	468.56	4.13	459	17	1269	35	2	
KCS34	Delfini	Epidote†	5	5	467.59	3.32	368	27	1032	54	3	**984 (45)**
KCS34	Delfini	Epidote†	6	6	467.16	3.06	339	25	976	50	3	
KCS34	Delfini	Epidote†	7	7	467.22	2.92	323	23	943	47	3	

*Assumed entrapment temperature = 500 °C

‡Assumed entrapment temperature = 450 °C

†Estimated entrapment temperature = 400 °C

All garnet compositions modeled as $X_{Alm} = 0.7$, $X_{Gr} = 0.2$, $X_{Py} = 0.1$

All epidote compositions modeled as $X_{Ep} = 0.5$, $X_{Cz} = 0.5$

$\Delta\nu 464$ cm^{-1} measured relative to Herkimer quartz standardization on day of analysis

Table B1 continued: Raman data of quartz-in-epidote-and-garnet measurements and calculated entrapment pressures.

Sample	Location	Quartz $\delta^{18}O$ (‰)	Calcite $\delta^{18}O$ (‰)	Temperature °C*	Temperature °C (1 σ)
SY1613	Lotos	17.8	15.76	373	29
SY1613 (duplicate)		17.9			
SY1617	Delfini	18.5	16.72	419	33
SY1617 (duplicate)		18.6			
SY1618	Delfini	18.3	16.52	419	32
SY1623	Delfini	21.1	19.24	408	31
SY1623 (duplicate)		21.1			

* Temperature calculated by using the Sharp and Kirschner (1994) quartz-calcite oxygen isotope fractionation calibration

The average $\delta^{18}O$ of duplicates was used to calculate temperatures

Table B2: Quartz-calcite δ18O values of boudin neck precipitates and calculated temperatures.

References

Adams, H.G., Cohen, L.H., and Rosenfeld, J.L. (1975a) Solid inclusion piezothermometry I: comparison dilatometry. American Mineralogist, 60, 574–583.

——— (1975b) Solid inclusion piezothermometry II: geometric basis, calibration for the association quartz-garnet, and application to some pelitic schists. American Mineralogist, 60, 584–598.

Ague, J.J., and Nicolescu, S. (2014) Carbon dioxide released from subduction zones by fluid-mediated reactions. Nature Geoscience, 7, 355–360.

Aliatis, I., Lambruschi, E., Mantovani, L., Bersani, D., Gatta, G.D., Tribaudino, M., and Lottici, P.P. (2017) High-pressure Raman spectroscopy on low albite. Physics and Chemistry of Minerals, 44, 213–220.

Angel, R.J., Alvaro, M., and Gonzalez-Platas, J. (2014a) EosFit7c and a Fortran module (library) for equation of state calculations. Zeitschrift für Kristallographie - Crystalline Materials, 229, 405–419.

Angel, R.J., Mazzucchelli, M.L., Alvaro, M., Nimis, P., and Nestola, F. (2014b) Geobarometry from host-inclusion systems: The role of elastic relaxation. American Mineralogist, 99, 2146–2149.

Angel, R.J., Alvaro, M., Miletich, R., and Nestola, F. (2017a) A simple and generalised P–T–V EoS for continuous phase transitions, implemented in EosFit and applied to quartz. Contributions to Mineralogy and Petrology, 172, 29.

Angel, R.J., Mazzucchelli, M.L., Alvaro, M., and Nestola, F. (2017b) EosFit-Pinc: A simple GUI for host-inclusion elastic thermobarometry. American Mineralogist, 102, 1957–1960.

Asell, J.F., and Nicol, M. (1968) Raman Spectrum of α Quartz at High Pressures. The Journal of Chemical Physics, 49, 5395–5399.

Ashley, K.T., Caddick, M.J., Steele-MacInnis, M.J., Bodnar, R.J., and Dragovic, B. (2014a) Geothermobarometric history of subduction recorded by quartz inclusions in garnet. Geochemistry, Geophysics, Geosystems, 15, 350–360.

Ashley, K.T., Steele-MacInnis, M., and Caddick, M.J. (2014b) QuIB Calc: A MATLAB® script for geobarometry based on Raman spectroscopy and elastic modeling of quartz inclusions in garnet. Computers & Geosciences, 66, 155–157.

Ashley, K.T., Steele-MacInnis, M., Bodnar, R.J., and Darling, R.S. (2016) Quartz-in-garnet inclusion barometry under fire: Reducing uncertainty from model estimates. Geology, 44, 699–702.

Ashley, K.T., Barkoff, D.W., and Steele-MacInnis, M. (2017) Barometric constraints based on apatite inclusions in garnet. American Mineralogist, 102, 743–749.

Auzende, A.-L., Daniel, I., Reynard, B., Lemaire, C., and Guyot, F. (2004) High-pressure behaviour of serpentine minerals: a Raman spectroscopic study. Physics and Chemistry of Minerals, 31, 269–277.

Avigad, D., and Garfunkel, Z. (1991) Uplift and exhumation of high-pressure metamorphic terrains: the example of the cycladic blueschist belt (Aegean Sea). Tectonophysics, 188, 357–372.

Barkoff, D.W., Ashley, K.T., and Steele-MacInnis, M. (2017) Pressures of skarn mineralization at Casting Copper, Nevada, USA, based on apatite inclusions in garnet. Geology, 45, 947–950.

Barr, H. (1990) Preliminary fluid inclusion studies in a high-grade blueschist terrain, Syros, Greece. Mineralogical Magazine, 54, 159–168.

Befus, K.S., and Gardner, J.E. (2016) Magma storage and evolution of the most recent effusive and explosive eruptions from Yellowstone Caldera. Contributions to Mineralogy and Petrology, 171, 30.

Befus, K.S., Lin, J.-F., Cisneros, M., and Fu, S. (2018) Feldspar Raman shift and application as a magmatic thermobarometer. American Mineralogist, 103, 600–609.

Behr, W.M., Kotowski, A.J., and Ashley, K.T. (2018) Dehydration-induced rheological heterogeneity and the deep tremor source in warm subduction zones. Geology, 46, 475–478.

Beyssac, O., Goffé, B., Chopin, C., and Rouzaud, J.N. (2002) Raman spectra of carbonaceous material in metasediments: a new geothermometer. Journal of Metamorphic Geology, 20, 859–871.

Bindeman, I. (2008) Oxygen isotopes in mantle and crustal magmas as revealed by single crystal analysis. Reviews in Mineralogy and Geochemistry, 69, 445–478.

Boppart, H., van Straaten, J., and Silvera, I.F. (1985) Raman spectra of diamond at high pressures. Physical Review B, 32, 1423–1425.

Bowen, G.J. (2009) The online isotopes in precipitation calculator, version 2.2. Avilable from:< http://www. waterisotopes. org.

Brichau, S., Ring, U., Carter, A., Monié, P., Bolhar, R., Stockli, D., and Brunel, M. (2007) Extensional faulting on Tinos Island, Aegean Sea, Greece: How many detachments? Tectonics, 26.

Bröcker, M., and Enders, M. (1999) U–Pb zircon geochronology of unusual eclogite-facies rocks from Syros and Tinos (Cyclades, Greece). Geological Magazine, 136, 111–118.

Bröcker, M., and Franz, L. (1998) Rb–Sr isotope studies on Tinos Island (Cyclades, Greece): additional time constraints for metamorphism, extent of infiltration-controlled overprinting and deformational activity. Geological Magazine, 135, 369–382.

Bröcker, M., and Franz, L. (2006) Dating metamorphism and tectonic juxtaposition on Andros Island (Cyclades, Greece): results of a Rb–Sr study. Geological Magazine, 143, 609–620.

Brocker, M., and Franz, L. (2006) Dating metamorphism and tectonic juxtaposition on Andros Island (Cyclades, Greece): results of a Rb-Sr study. Geological Magazine, 143, 609–620.

Bröcker, M., Kreuzer, H., Matthews, A., and Okrusch, M. (1993) 40Ar/39Ar and oxygen isotope studies of polymetamorphism from Tinos Island, Cycladic blueschist belt, Greece. Journal of Metamorphic Geology, 11, 223–240.

Bröcker, M., Bieling, D., Hacker, B., and Gans, P. (2004) High-Si phengite records the time of greenschist facies overprinting: implications for models suggesting mega-detachments in the Aegean Sea. Journal of Metamorphic Geology, 22, 427–442.

Buick, I.S., and Holland, T.J.B. (1991) The nature and distribution of fluids during amphibolite facies metamorphism, Naxos (Greece). Journal of Metamorphic Geology, 9, 301–314.

Carlson, W.D. (1989) The significance of intergranular diffusion to the mechanisms and kinetics of porphyroblast crystallization. Contributions to Mineralogy and Petrology, 103, 1–24.

——— (2002) Scales of disequilibrium and rates of equilibration during metamorphism. American Mineralogist, 87, 185–204.

——— (2015) Presidential Address. Scales of disequilibrium and rates of equilibration during metamorphism. American Mineralogist, 87, 185–204.

Carswell, D.A., Tucker, R.D., O'Brien, P.J., and Krogh, T.E. (2003) Coesite micro-inclusions and the U/Pb age of zircons from the Hareidland Eclogite in the Western Gneiss Region of Norway. Lithos, 67, 181–190.

Cliff, R.A., Bond, C.E., Butler, R.W.H., and Dixon, J.E. (2017) Geochronological challenges posed by continuously developing tectonometamorphic systems: insights from Rb–Sr mica ages from the Cycladic Blueschist Belt, Syros (Greece). Journal of Metamorphic Geology, 35, 197–211.

Cloos, M. (1982) Flow melanges: Numerical modeling and geologic constraints on their origin in the Franciscan subduction complex, California. Geological Society of America Bulletin, 93, 330–345.

Cloos, M., and Shreve, R.L. (1988a) Subduction-channel model of prism accretion, melange formation, sediment subduction, and subduction erosion at convergent plate margins: 1. Background and description. pure and applied geophysics, 128, 455–500.

——— (1988b) Subduction-channel model of prism accretion, melange formation, sediment subduction, and subduction erosion at convergent plate margins: 2. Implications and discussion. pure and applied geophysics, 128, 501–545.

Cohen, L.H., and Rosenfeld, J.L. (1979) Diamond: Depth of Crystallization Inferred from Compressed Included Garnet. The Journal of Geology, 87, 333–340.

Comodi, P., Liu, Y., and Frezzotti, M.L. (2001) Structural and vibrational behaviour of fluorapatite with pressure. Part II: in situ micro-Raman spectroscopic investigation. Physics and Chemistry of Minerals, 28, 225–231.

Decremps, F., Pellicer-Porres, J., Saitta, A.M., Chervin, J.-C., and Polian, A. (2002) High-pressure Raman spectroscopy study of wurtzite ZnO. Physical Review B, 65, 092101.

Duffy, T.S., Meade, C., Fei, Y., Mao, H.-K., and Hemley, R.J. (2015) High-pressure phase transition in brucite, $Mg(OH)_2$. American Mineralogist, 80, 222–230.

Enami, M., Nishiyama, T., and Mouri, T. (2007) Laser Raman microspectrometry of metamorphic quartz: A simple method for comparison of metamorphic pressures. American Mineralogist, 92, 1303–1315.

Endo, S., Wallis, S.R., Tsuboi, M., Torres De León, R., and Solari, L.A. (2012) Metamorphic evolution of lawsonite eclogites from the southern Motagua fault zone, Guatemala: insights from phase equilibria and Raman spectroscopy. Journal of Metamorphic Geology, 30, 143–164.

Ernst, W.G. (1971) Do mineral parageneses reflect unusually high-pressure conditions of Franciscan metamorphism? American Journal of Science, 270, 81–108.

Ernst, W.G., Maruyama, S., and Wallis, S. (1997) Buoyancy-driven, rapid exhumation of ultrahigh-pressure metamorphosed continental crust. Proceedings of the National Academy of Sciences, 94, 9532–9537.

Famin, V., Philippot, P., Jolivet, L., and Agard, P. (2004) Evolution of hydrothermal regime along a crustal shear zone, Tinos Island, Greece. Tectonics, 23.

Ferry, J.M., and Spear, F.S. (1978) Experimental calibration of the partitioning of Fe and Mg between biotite and garnet. Contributions to Mineralogy and Petrology, 66, 113–117.

Frezzotti, M.L., Selverstone, J., Sharp, Z.D., and Compagnoni, R. (2011) Carbonate dissolution during subduction revealed by diamond-bearing rocks from the Alps. Nature Geoscience, 4, 703–706.

Fu, B., Bröcker, M., Ireland, T., Holden, P., and Kinsley, L.P.J. (2014) Zircon U–Pb, O, and Hf isotopic constraints on Mesozoic magmatism in the Cyclades, Aegean Sea, Greece. International Journal of Earth Sciences, 104, 75–87.

Ganor, J., Matthews, A., Schliestedt, M., and Garfunkel, Z. (1996) Oxygen isotopic heterogeneities of metamorphic rocks: an original tectonostratigraphic signature, or an imprint of exotic fluids? A case study of Sifnos and Tinos islands (Greece). European Journal of Mineralogy, 719–732.

Gärtner, C., Bröcker, M., Strauss, H., and Farber, K. (2011) Strontium-, carbon- and oxygen-isotope compositions of marbles from the Cycladic blueschist belt, Greece. Geological Magazine, 148, 511–528.

Gatta, G.D., Merlini, M., Lee, Y., and Poli, S. (2011) Behavior of epidote at high pressure and high temperature: a powder diffraction study up to 10 GPa and 1,200 K. Physics and Chemistry of Minerals, 38, 419–428.

Gillet, P., Guyot, F., and Malezieux, J.-M. (1989) High-pressure, high-temperature Raman spectroscopy of Ca_2GeO_4 (olivine form): some insights on anharmonicity. Physics of the Earth and Planetary Interiors, 58, 141–154.

Gillet, P., Fiquet, G., Malezieux, J.M., and Geiger, C.A. (1992) High-pressure and high-temperature Raman spectroscopy of end-member garnets; pyrope, grossular and andradite. European Journal of Mineralogy, 4, 651–664.

Graham, C.M., Atkinson, J., and Harmon, R.S. (1981) Hydrogen isotope fractionation in the system chlorite-water. NERC 6th progress report of research, 1984, 1–139.

Grasemann, B., Schneider, D.A., Stöckli, D.F., and Iglseder, C. (2012) Miocene bivergent crustal extension in the Aegean: Evidence from the western Cyclades (Greece). Lithosphere, 4, 23–39.

Gryger, K.J. (2017) Spatial Variability of the Depth to the Magma Reservoir Beneath the Yellowstone Caldera Inferred from Observations of Seiche Loading Induced Strain.

Gualda, G.A.R., Ghiorso, M.S., Lemons, R.V., and Carley, T.L. (2012) Rhyolite-MELTS: a Modified Calibration of MELTS Optimized for Silica-rich, Fluid-bearing Magmatic Systems. Journal of Petrology, 53, 875–890.

Guiraud, M., and Powell, R. (2006) P–V–T relationships and mineral equilibria in inclusions in minerals. Earth and Planetary Science Letters, 244, 683–694.

Hacker, B.R., Ratschbacher, L., Webb, L., and Shuwen, D. (1995) What brought them up? Exhumation of the Dabie Shan ultrahigh-pressure rocks. Geology, 23, 743–746.

Hacker, B.R., Andersen, T.B., Johnston, S., Kylander-Clark, A.R.C., Peterman, E.M., Walsh, E.O., and Young, D. (2010) High-temperature deformation during continental-margin subduction & exhumation: The ultrahigh-pressure Western Gneiss Region of Norway. Tectonophysics, 480, 149–171.

Hanfland, M., Syassen, K., Fahy, S., Louie, S.G., and Cohen, M.L. (1985) Pressure dependence of the first-order Raman mode in diamond. Physical Review B, 31, 6896–6899.

Hanfland, M., Beister, H., and Syassen, K. (1989) Graphite under pressure: Equation of state and first-order Raman modes. Physical Review B, 39, 12598–12603.

Harris, J.W., and Munn, R.W. (1970) Thermal expansion of garnets included in diamond. Journal of Geophysical Research, 75, 5775–5792.

Hawthorne, F.C., and Oberti, R. (2007) Classification of the Amphiboles. Reviews in Mineralogy and Geochemistry, 67, 55–88.

Hemley R. J. (2013) Pressure Dependence of Raman Spectra of SiO_2 Polymorphs: α-Quartz, Coesite, and Stishovite. High-Pressure Research in Mineral Physics: A Volume in Honor of Syun-iti Akimoto.

Hemley, R.J. (1987) Pressure Dependence of Raman Spectra of SiO2 Polymorphs: α-Quartz, Coesite, and Stishovite. In M. H.nghnani and Y. Syono, Eds., High-Pressure Research in Mineral Physics: A Volume in Honor of Syun-iti Akimoto pp. 347–359. American Geophysical Union.

Hemley, R.J., Cohen, R.E., Yeganeh-Haeri, A., Mao, H.K., Weidner, D.J., and Ito, E. (1989) Raman spectroscopy and lattice dynamics of $MgSiO_3$-perovskite at high pressure. Perovskite: A Structure of Great Interest to Geophysics and Materials Science, 35–44.

Holland, T.J.B. (1980) The reaction albite = jadeite+quartz determined experimentally in the range 600-1200 degrees C. American Mineralogist, 65, 129–134.

Holland, T.J.B. (1988) Preliminary phase relations involving glaucophane and applications to high pressure petrology: new heat capacity and thermodynamic data. Contributions to Mineralogy and Petrology, 99, 134–142.

Holland, T.J.B., and Powell, R. (1996a) Thermodynamics of order-disorder in minerals: I. Symmetric formalism applied to minerals of fixed composition. American Mineralogist, 81, 1413–1424.

——— (1996b) Thermodynamics of order-disorder in minerals: II. Symmetric formalism applied to solid solutions. American Mineralogist, 81, 1425–1437.

——— (1998) An internally consistent thermodynamic data set for phases of petrological interest. Journal of Metamorphic Geology, 16, 309–343.

——— (2011) An improved and extended internally consistent thermodynamic dataset for phases of petrological interest, involving a new equation of state for solids. Journal of Metamorphic Geology, 29, 333–383.

Holland, T.J.B., Redfern, S.A.T., and Pawley, A.R. (1996) Volume behavior of hydrous minerals at high pressure and temperature: II. Compressibilities of lawsonite, zoisite, clinozoisite, and epidote. American Mineralogist, 81, 341–348.

Howell, D., Wood, I.G., Dobson, D.P., Jones, A.P., Nasdala, L., and Harris, J.W. (2010) Quantifying strain birefringence halos around inclusions in diamond. Contributions to Mineralogy and Petrology, 160, 705–717.

Hu, G., and Clayton, R.N. (2003) Oxygen isotope salt effects at high pressure and high temperature and the calibration of oxygen isotope geothermometers. Geochimica et Cosmochimica Acta, 67, 3227–3246.

Izraeli, E.S., Harris, J.W., and Navon, O. (1999) Raman barometry of diamond formation. Earth and Planetary Science Letters, 173, 351–360.

Jamtveit, B., Austrheim, H., and Putnis, A. (2016) Disequilibrium metamorphism of stressed lithosphere. Earth-Science Reviews, 154, 1–13.

Javoy, M. (1977) Stable isotopes and geothermometry. Journal of the Geological Society, 133, 609–636.

Jolivet, L., and Brun, J.-P. (2010) Cenozoic geodynamic evolution of the Aegean. International Journal of Earth Sciences, 99, 109–138.

Jolivet, L., Faccenna, C., Goffé, B., Burov, E., and Agard, P. (2003) Subduction tectonics and exhumation of high-pressure metamorphic rocks in the Mediterranean orogens. American Journal of Science, 303, 353–409.

Jolivet, L., Lecomte, E., Huet, B., Denèle, Y., Lacombe, O., Labrousse, L., Le Pourhiet, L., and Mehl, C. (2010) The North Cycladic Detachment System. Earth and Planetary Science Letters, 289, 87–104.

Keiter, M., Piepjohn, K., Ballhaus, C., Lagos, M., and Bode, M. (2004) Structural development of high-pressure metamorphic rocks on Syros island (Cyclades, Greece). Journal of Structural Geology, 26, 1433–1445.

Keiter, M., Ballhaus, C., and Tomaschek, F. (2011) A new geological map of the Island of Syros (Aegean Sea, Greece): implications for lithostratigraphy and structural history of the Cycladic Blueschist Unit Vol. 481. Geological Society of America.

Kelly, E.D., Carlson, W.D., and Ketcham, R.A. (2013) Magnitudes of departures from equilibrium during regional metamorphism of porphyroblastic rocks. Journal of Metamorphic Geology, 31, 981–1002.

Kleine, B.I., Skelton, A.D.L., Huet, B., and Pitcairn, I.K. (2014) Preservation of Blueschist-facies Minerals along a Shear Zone by Coupled Metasomatism and Fast-flowing CO2-bearing Fluids. Journal of Petrology, 55, 1905–1939.

Knittle, E., Phillips, W., and Williams, Q. (2001) An infrared and Raman spectroscopic study of gypsum at high pressures. Physics and Chemistry of Minerals, 28, 630–640.

Kohn, M.J. (2014) “Thermoba-Raman-try”: Calibration of spectroscopic barometers and thermometers for mineral inclusions. Earth and Planetary Science Letters, 388, 187–196.

Kouketsu, Y., Enami, M., Mouri, T., Okamura, M., and Sakurai, T. (2014) Composite metamorphic history recorded in garnet porphyroblasts of Sambagawa metasediments in the Besshi region, central Shikoku, Southwest Japan. Island Arc, 23, 263–280.

Kreulen, R. (1980) CO 2 rich fluids during regional metamorphism on Naxos (Greece); carbon isotopes and fluid inclusions. American Journal of Science, 280, 745–771.

Krogh, E.J. (1982) Metamorphic evolution of Norwegian country-rock eclogites, as deduced from mineral inclusions and compositional zoning in garnets. Lithos, 15, 305–321.

Kylander-Clark, A.R.C., Hacker, B.R., and Mattinson, J.M. (2008) Slow exhumation of UHP terranes: Titanite and rutile ages of the Western Gneiss Region, Norway. Earth and Planetary Science Letters, 272, 531–540.

Lagos, M., Scherer, E.E., Tomaschek, F., Münker, C., Keiter, M., Berndt, J., and Ballhaus, C. (2007) High precision Lu–Hf geochronology of Eocene eclogite-facies rocks from Syros, Cyclades, Greece. Chemical Geology, 243, 16–35.

Laurent, V., Jolivet, L., Roche, V., Augier, R., Scaillet, S., and Cardello, G.L. (2016) Strain localization in a fossilized subduction channel: Insights from the Cycladic Blueschist Unit (Syros, Greece). Tectonophysics, 672–673, 150–169.

Lin, C.-C. (2003) Pressure-induced metastable phase transition in orthoenstatite (MgSiO3) at room temperature: a Raman spectroscopic study. Journal of Solid State Chemistry, 174, 403–411.

Liu, L.-G., and Mernagh, T.P. (1992) Phase transitions and Raman spectra of anatase and rutile at high pressures and room temperature. European Journal of Mineralogy, 45–52.

Mao, Z., Jiang, F., and Duffy, T.S. (2007) Single-crystal elasticity of zoisite Ca2Al3Si3O12 (OH) by Brillouin scattering. American Mineralogist, 92, 570–576.

Marschall, H.R. (2006) Syros Metasomatic Tourmaline: Evidence for Very High- 11B Fluids in Subduction Zones. Journal of Petrology, 47, 1915–1942.

Matthews, A., and Schliestedt, M. (1984) Evolution of the blueschist and greenschist facies rocks of Sifnos, Cyclades, Greece. Contributions to Mineralogy and Petrology, 88, 150–163.

Mazzucchelli, M.L., Burnley, P., Angel, R.J., Morganti, S., Domeneghetti, M.C., Nestola, F., and Alvaro, M. (2018) Elastic geothermobarometry: Corrections for the geometry of the host-inclusion system. Geology, 46, 231–234.

Mehl, C., Jolivet, L., and Lacombe, O. (2005) From ductile to brittle: Evolution and localization of deformation below a crustal detachment (Tinos, Cyclades, Greece). Tectonics, 24.

Mernagh, T.P., and Liu, L. (1991) Raman spectra from the Al_2SiO_5 polymorphs at high pressures and room temperature. Physics and Chemistry of Minerals, 18, 126–130.

Mernagh, T.P., and Liu, L.-G. (1990) Pressure dependence of Raman spectra from the garnet end-members pyrope, grossularite and almandite. Journal of Raman Spectroscopy, 21, 305–309.

Miller, D.P., Marschall, H.R., and Schumacher, J.C. (2009) Metasomatic formation and petrology of blueschist-facies hybrid rocks from Syros (Greece): Implications for reactions at the slab–mantle interface. Lithos, 107, 53–67.

Murri, M., Mazzucchelli, M.L., Campomenosi, N., Korsakov, A.V., Prencipe, M., Mihailova, B.D., Scambelluri, M., Angel, R.J., and Alvaro, M. (2018) Raman elastic geobarometry for anisotropic mineral inclusions. American Mineralogist, 103, 1869–1872.

Myers, M.L., Wallace, P.J., Wilson, C.J.N., Morter, B.K., and Swallow, E.J. (2016) Prolonged ascent and episodic venting of discrete magma batches at the onset of the Huckleberry Ridge supereruption, Yellowstone. Earth and Planetary Science Letters, 451, 285–297.

Nestola, F., Nimis, P., Ziberna, L., Longo, M., Marzoli, A., Harris, J.W., Manghnani, M.H., and Fedortchouk, Y. (2011) First crystal-structure determination of olivine in diamond: Composition and implications for provenance in the Earth's mantle. Earth and Planetary Science Letters, 305, 249–255.

Nestola, F., Prencipe, M., Nimis, P., Sgreva, N., Perritt, S.H., Chinn, I.L., and Zaffiro, G. (2018) Toward a Robust Elastic Geobarometry of Kyanite Inclusions in Eclogitic Diamonds. Journal of Geophysical Research: Solid Earth.

Occelli, F., Loubeyre, P., and LeToullec, R. (2003) Properties of diamond under hydrostatic pressures up to 140 GPa. Nature Materials, 2, 151–154.

Ohmoto, H. (1972) Systematics of Sulfur and Carbon Isotopes in Hydrothermal Ore Deposits. Economic Geology, 67, 551–578.

Parkinson, C.D., and Katayama, I. (1999) Present-day ultrahigh-pressure conditions of coesite inclusions in zircon and garnet: Evidence from laser Raman microspectroscopy. Geology, 27, 979–982.

Parra, T., Vidal, O., and Jolivet, L. (2002) Relation between the intensity of deformation and retrogression in blueschist metapelites of Tinos Island (Greece) evidenced by chlorite–mica local equilibria. Lithos, 63, 41–66.

Pattison, D.R.M., De Capitani, C., and Gaidies, F. (2011) Petrological consequences of variations in metamorphic reaction affinity. Journal of Metamorphic Geology, 29, 953–977.

Pawley, A.R., Redfern, S.A.T., and Holland, T.J.B. (1996) Volume behavior of hydrous minerals at high pressure and temperature: I. Thermal expansion of lawsonite, zoisite, clinozoisite, and diaspore. American Mineralogist, 81, 335–340.

Peng, G., Luhr, J.F., and McGee, J.J. (1997) Factors controlling sulfur concentrations in volcanic apatite. American Mineralogist, 82, 1210–1224.

Philippon, M., Brun, J.-P., and Gueydan, F. (2011) Tectonics of the Syros blueschists (Cyclades, Greece): From subduction to Aegean extension. Tectonics, 30, TC4001.

Platt, J.P. (1986) Dynamics of orogenic wedges and the uplift of high-pressure metamorphic rocks. Geological Society of America Bulletin, 97, 1037–1053.

Putlitz, B., Matthews, A., and Valley, J.W. (2000) Oxygen and hydrogen isotope study of high-pressure metagabbros and metabasalts (Cyclades, Greece): implications for the subduction of oceanic crust. Contributions to Mineralogy and Petrology, 138, 114–126.

Putlitz, B., Cosca, M.A., and Schumacher, J.C. (2005) Prograde mica 40Ar/39Ar growth ages recorded in high pressure rocks (Syros, Cyclades, Greece). Chemical Geology, 214, 79–98.

Qin, F., Wu, X., Wang, Y., Fan, D., Qin, S., Yang, K., Townsend, J.P., and Jacobsen, S.D. (2016) High-pressure behavior of natural single-crystal epidote and clinozoisite up to 40 GPa. Physics and Chemistry of Minerals, 1–11.

Reynard, B., and Wunder, B. (2006) High-pressure behavior of synthetic antigorite in the MgO-SiO_2-H_2O system from Raman spectroscopy. American Mineralogist, 91, 459–462.

Ridley, J. (1984) Evidence of a temperature-dependent ‘blueschist’to ‘eclogite’transformation in high-pressure metamorphism of metabasic rocks. Journal of Petrology, 25, 852–870.

Ring, U., and Reischmann, T. (2002) The weak and superfast Cretan detachment, Greece: exhumation at subduction rates in extruding wedges. Journal of the Geological Society, 159, 225–228.

Ring, U., Will, T., Glodny, J., Kumerics, C., Gessner, K., Thomson, S., Güngör, T., Monié, P., Okrusch, M., and Drüppel, K. (2007) Early exhumation of high-pressure rocks in extrusion wedges: Cycladic blueschist unit in the eastern Aegean, Greece, and Turkey. Tectonics, 26, TC2001.

Roche, V., Laurent, V., Cardello, G.L., Jolivet, L., and Scaillet, S. (2016) Anatomy of the Cycladic Blueschist Unit on Sifnos Island (Cyclades, Greece). Journal of Geodynamics, 97, 62–87.

Rosenbaum, G., Avigad, D., and Sánchez-Gómez, M. (2002) Coaxial flattening at deep levels of orogenic belts: evidence from blueschists and eclogites on Syros and Sifnos (Cyclades, Greece). Journal of Structural Geology, 24, 1451–1462.

Rosenfeld, J.L. (1969) Stress effects around quartz inclusions in almandine and the piezothermometry of coexisting aluminum silicates. American Journal of Science, 267, 317–351.

Rosenfeld, J.L., and Chase, A.B. (1961) Pressure and temperature of crystallization from elastic effects around solid inclusions in minerals? American Journal of Science, 259, 519–541.

Rubie, D.C. (1998) Disequilibrium during metamorphism: the role of nucleation kinetics. Geological Society, London, Special Publications, 138, 199–214.

Ryzhova, T.V., Aleksandrov, K.S., and Korobkova, V.M. (1966) The elastic properties of rock-forming minerals; V, Additional data on silicates. Physics of the Solid Earth, 2, 63–65.

Samara, G.A., and Peercy, P.S. (1973) Pressure and Temperature Dependence of the Static Dielectric Constants and Raman Spectra of TiO_2 (Rutile). Physical Review B, 7, 1131–1148.

Sandler, J., Shaffer, M.S.P., Windle, A.H., Halsall, M.P., Montes-Morán, M.A., Cooper, C.A., and Young, R.J. (2003) Variations in the Raman peak shift as a function of hydrostatic pressure for various carbon nanostructures: A simple geometric effect. Physical Review B, 67, 035417.

Scheele, N., and Hoefs, J. (1992) Carbon isotope fractionation between calcite, graphite and CO2: an experimental study. Contributions to Mineralogy and Petrology, 112, 35–45.

Schliestedt, M., and Matthews, A. (1987) Transformation of blueschist to greenschist facies rocks as a consequence of fluid infiltration, Sifnos (Cyclades), Greece. Contributions to Mineralogy and Petrology, 97, 237–250.

Schmädicke, E., and Will, T.M. (2003) Pressure–temperature evolution of blueschist facies rocks from Sifnos, Greece, and implications for the exhumation of high-pressure rocks in the Central Aegean. Journal of Metamorphic Geology, 21, 799–811.

Schmidt, C., and Ziemann, M.A. (2000) In-situ Raman spectroscopy of quartz: A pressure sensor for hydrothermal diamond-anvil cell experiments at elevated temperatures. American Mineralogist, 85, 1725–1734.

Schmidt, C., Steele-MacInnis, M., Watenphul, A., and Wilke, M. (2013) Calibration of zircon as a Raman spectroscopic pressure sensor to high temperatures and application to water-silicate melt systems. American Mineralogist, 98, 643–650.

Schouwink, P., Miletich, R., Ullrich, A., Glasmacher, U.A., Trautmann, C., Neumann, R., and Kohn, B.P. (2010) Ion tracks in apatite at high pressures: the effect of crystallographic track orientation on the elastic properties of fluorapatite under hydrostatic compression. Physics and Chemistry of Minerals, 37, 371–387.

Schuiling, R.D., and Kreulen, R. (1979) Are thermal domes heated by CO2-rich fluids from the mantle? Earth and Planetary Science Letters, 43, 298–302.

Schumacher, J.C., Brady, J.B., Cheney, J.T., and Tonnsen, R.R. (2008) Glaucophane-bearing Marbles on Syros, Greece. Journal of Petrology, 49, 1667–1686.

Selverstone, J., and Spear, F.S. (1985) Metamorphic P–T Paths from pelitic schists and greenstones from the south-west Tauern Window, Eastern Alps. Journal of Metamorphic Geology, 3, 439–465.

Selverstone, J., Franz, G., Thomas, S., and Getty, S. (1992) Fluid variability in 2 GPa eclogites as an indicator of fluid behavior during subduction. Contributions to Mineralogy and Petrology, 112, 341–357.

Sharp, Z. (2017) Principles of stable isotope geochemistry.

Sharp, Z.D. (1990) A laser-based microanalytical method for the in situ determination of oxygen isotope ratios of silicates and oxides. Geochimica et Cosmochimica Acta, 54, 1353–1357.

Sharp, Z.D., and Kirschner, D.. (1994) Quartz-calcite oxygen isotope thermometry: A calibration based on natural isotopic variations. Geochimica et Cosmochimica Acta, 58, 4491–4501.

Sharp, Z.D., Atudorei, V., and Durakiewicz, T. (2001) A rapid method for determination of hydrogen and oxygen isotope ratios from water and hydrous minerals. Chemical Geology, 178, 197–210.

Siebenaller, L., Boiron, M.-C., Vanderhaeghe, O., Hibsch, C., Jessell, M.W., Andre-Mayer, A.-S., France-Lanord, C., and Photiades, A. (2013) Fluid record of rock exhumation across the brittle–ductile transition during formation of a Metamorphic Core Complex (Naxos Island, Cyclades, Greece). Journal of Metamorphic Geology, 31, 313–338.

Sobolev, N.V., Fursenko, B.A., Goryainov, S.V., Shu, J., Hemley, R.J., Mao, H., and Boyd, F.R. (2000) Fossilized high pressure from the Earth's deep interior: The coesite-in-diamond barometer. Proceedings of the National Academy of Sciences, 97, 11875–11879.

Soukis, K., and Stockli, D.F. (2013) Structural and thermochronometric evidence for multi-stage exhumation of southern Syros, Cycladic islands, Greece. Tectonophysics, 595–596, 148–164.

Spear, F.S. (2014) The duration of near-peak metamorphism from diffusion modelling of garnet zoning. Journal of Metamorphic Geology, 32, 903–914.

Spear, F.S., and Franz, G. (1986) P-T evolution of metasediments from the Eclogite Zone, south-central Tauern Window, Austria. Lithos, 19, 219–234.

Spear, F.S., and Pattison, D.R.M. (2017) The implications of overstepping for metamorphic assemblage diagrams (MADs). Chemical Geology, 457, 38–46.

Spear, F.S., Thomas, J.B., and Hallett, B.W. (2014) Overstepping the garnet isograd: a comparison of QuiG barometry and thermodynamic modeling. Contributions to Mineralogy and Petrology, 168, 1059.

Swamy, V., Kuznetsov, A., Dubrovinsky, L.S., Caruso, R.A., Shchukin, D.G., and Muddle, B.C. (2005) Finite-size and pressure effects on the Raman spectrum of nanocrystalline anatase TiO_2. Physical Review B, 71, 184302.

Syracuse, E.M., van Keken, P.E., and Abers, G.A. (2010) The global range of subduction zone thermal models. Physics of the Earth and Planetary Interiors, 183, 73–90.

Tardieu, A., Cansell, F., and Petitet, J.P. (1990) Pressure and temperature dependence of the first-order Raman mode of diamond. Journal of Applied Physics, 68, 3243–3245.

Thomas, J.B., and Spear, F.S. (2018) Experimental study of quartz inclusions in garnet at pressures up to 3.0 GPa: evaluating validity of the quartz-in-garnet inclusion elastic thermobarometer. Contributions to Mineralogy and Petrology, 173, 42.

Tomaschek, F., Baumann, A., Villa, I.M., Kennedy, A., and Ballhaus, C. (2000) Geochronological constraints on a Cretaceous metamorphic event from the Vari Unit (Syros, Cyclades, Greece). Beihefte zum European Journal of Mineralogy, 12, 214.

Tomaschek, F., Kennedy, A.K., Villa, I.M., Lagos, M., and Ballhaus, C. (2003) Zircons from Syros, Cyclades, Greece—Recrystallization and Mobilization of Zircon During High-Pressure Metamorphism. Journal of Petrology, 44, 1977–2002.

Trotet, F., Vidal, O., and Jolivet, L. (2001a) Exhumation of Syros and Sifnos metamorphic rocks (Cyclades, Greece). New constraints on the P-T paths. European Journal of Mineralogy, 13, 901–902.

Trotet, F., Jolivet, L., and Vidal, O. (2001b) Tectono-metamorphic evolution of Syros and Sifnos islands (Cyclades, Greece). Tectonophysics, 338, 179–206.

Tsujimori, T., Sisson, V.B., Liou, J.G., Harlow, G.E., and Sorensen, S.S. (2006) Very-low-temperature record of the subduction process: A review of worldwide lawsonite eclogites. Lithos, 92, 609–624.

Valley, J.W., Kitchen, N., Kohn, M.J., Niendorf, C.R., and Spicuzza, M.J. (1995) UWG-2, a garnet standard for oxygen isotope ratios: Strategies for high precision and accuracy with laser heating. Geochimica et Cosmochimica Acta, 59, 5223–5231.

van der Klauw, S.N.G.C., Reinecke, T., and Stöckhert, B. (1997) Exhumation of ultrahigh-pressure metamorphic oceanic crust from Lago di Cignana, Piemontese zone, western Alps: the structural record in metabasites. Lithos, 41, 79–102.

Vazquez, J.A., Kyriazis, S.F., Reid, M.R., Sehler, R.C., and Ramos, F.C. (2009) Thermochemical evolution of young rhyolites at Yellowstone: Evidence for a cooling but periodically replenished postcaldera magma reservoir. Journal of Volcanology and Geothermal Research, 188, 186–196.

Wain, A., Waters, D., Jephcoat, A., and Olijynk, H. (2000) The high-pressure to ultrahigh-pressure eclogite transition in the Western Gneiss Region, Norway. European Journal of Mineralogy, 12, 667–687.

Walowski, K.J., Wallace, P.J., Hauri, E.H., Wada, I., and Clynne, M.A. (2015) Slab melting beneath the Cascade Arc driven by dehydration of altered oceanic peridotite. Nature Geoscience, 8, 404–408.

Wang, S.Y., Sharma, S.K., and Cooney, T.F. (1993) Micro-Raman and infrared spectral study of forsterite under high pressure. American Mineralogist, 78, 469–476.

Wang, Z., O'Neill, H.S.C., Lazor, P., and Saxena, S.K. (2002a) High pressure Raman spectroscopic study of spinel $MgCr_2O_4$. Journal of Physics and Chemistry of Solids, 63, 2057–2061.

Wang, Z., Lazor, P., Saxena, S.K., and O'Neill, H.S.C. (2002b) High pressure Raman spectroscopy of ferrite $MgFe_2O_4$. Materials Research Bulletin, 37, 1589–1602.

Wang, Z., Lazor, P., Saxena, S.K., and Artioli, G. (2002c) High-Pressure Raman Spectroscopic Study of Spinel ($ZnCr_2O_4$). Journal of Solid State Chemistry, 165, 165–170.

Wang, Z., Saxena, S.K., and Zha, C.S. (2002d) In situ x-ray diffraction and Raman spectroscopy of pressure-induced phase transformation in spinel Zn_2TiO_4. Physical Review B, 66, 024103.

Wang, Z., Schiferl, D., Zhao, Y., and O'Neill, H.S.C. (2003a) High pressure Raman spectroscopy of spinel-type ferrite $ZnFe_2O_4$. Journal of Physics and Chemistry of Solids, 64, 2517–2523.

Wang, Z., Downs, R.T., Pischedda, V., Shetty, R., Saxena, S.K., Zha, C.S., Zhao, Y.S., Schiferl, D., and Waskowska, A. (2003b) High-pressure x-ray diffraction and Raman spectroscopic studies of the tetragonal spinel $CoFe_2O_4$. Physical Review B, 68, 094101.

Waters, D.J., and Lovegrove, D.P. (2002) Assessing the extent of disequilibrium and overstepping of prograde metamorphic reactions in metapelites from the Bushveld Complex aureole, South Africa. Journal of Metamorphic Geology, 20, 135–149.

Webster, J.D., and Piccoli, P.M. (2015) Magmatic Apatite: A Powerful, Yet Deceptive, Mineral. Elements, 11, 177–182.

Wenner, D.B., and Taylor, H.P. (1971) Temperatures of serpentinization of ultramafic rocks based on O18/O16 fractionation between coexisting serpentine and magnetite. Contributions to Mineralogy and Petrology, 32, 165–185.

Wheeler, J. (2014) Dramatic effects of stress on metamorphic reactions. Geology, 42, 647–650.

Wickham, S.M., and Taylor, H.P. (1985) Stable isotopic evidence for large-scale seawater infiltration in a regional metamorphic terrane; the Trois Seigneurs Massif, Pyrenees, France. Contributions to Mineralogy and Petrology, 91, 122–137.

Wijbrans, J.R., and McDougall, I. (1986) 40Ar/39Ar dating of white micas from an Alpine high-pressure metamorphic belt on Naxos (Greece): the resetting of the argon isotopic system. Contributions to Mineralogy and Petrology, 93, 187–194.

Wijbrans, J.R., Schliestedt, M., and York, D. (1990) Single grain argon laser probe dating of phengites from the blueschist to greenschist transition on Sifnos (Cyclades, Greece). Contributions to Mineralogy and Petrology, 104, 582–593.

Wilbur, D.E., and Ague, J.J. (2006) Chemical disequilibrium during garnet growth: Monte Carlo simulations of natural crystal morphologies. Geology, 34, 689–692.

Williams, Q., Jeanloz, R., and McMillan, P. (1987) Vibrational spectrum of $MgSiO_3$ perovskite: Zero-pressure Raman and mid-infrared spectra to 27 GPa. Journal of Geophysical Research: Solid Earth, 92, 8116–8128.

Wolfe, O.M., and Spear, F.S. (2018) Determining the amount of overstepping required to nucleate garnet during Barrovian regional metamorphism, Connecticut Valley Synclinorium. Journal of Metamorphic Geology, 36, 79–94.

Yang, H., Downs, R.T., Finger, L.W., Hazen, R.M., and Prewitt, C.T. (1997) Compressibility and crystal structure of kyanite, Al_2SiO_5, at high pressure. American Mineralogist, 82, 467–474.